



THESIS  
2  
(1996)

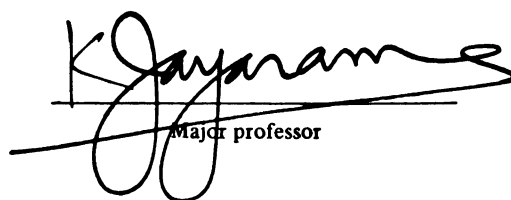


This is to certify that the  
thesis entitled  
Process Modeling for Liquid Composite Molding

presented by  
Jinglei Chen

has been accepted towards fulfillment  
of the requirements for  
M.S. degree in Chemical Engineering

Date 12/1/95

  
Major professor



**PLACE IN RETURN BOX to remove this checkout from your record.  
TO AVOID FINES return on or before date due.**

DATE DUE	DATE DUE	DATE DUE
_____	_____	_____
_____	_____	_____
_____	_____	_____
_____	_____	_____
_____	_____	_____
_____	_____	_____
_____	_____	_____

**MSU is An Affirmative Action/Equal Opportunity Institution**

c:\pic\datedue.pm3-p.1

**PROCESS MODELING FOR LIQUID COMPOSITE MOLDING**

**By**

**Jinglei Chen**

**A THESIS**

**Submitted to  
Michigan State University  
in partial fulfillment of the requirements  
for the degree of**

**MASTER OF SCIENCE**

**Department of Chemical Engineering**

**1995**

## **ABSTRACT**

### **PROCESS MODELING FOR LIQUID COMPOSITE MOLDING**

By

Jinglei Chen

A process model has been developed for mold filling in the liquid composite molding process. This model incorporates mass transfer and dissolution of binder from the fiber preforms into resin, as well as non-isothermal, reactive filling of the preforms, with heated mold walls. The model was first validated by experimental data. Then it was used to investigate resin viscosity variation due to various factors and to develop design guidelines for mold filling with soluble binder.

Transverse flow through real bi-directional fiber preforms can be adequately described by considering flow across orthogonal sets of filaments. This flow problem was solved by both finite element computations and analytically by applying the lubrication approximation for higher fiber volume fraction. The analysis of the lubrication equations was carried out with a decoupling approach developed in this work.

*To my dear wife Min Lu*

## **ACKNOWLEDGEMENT**

The author would like to thank Professor Krishnamurthy Jayaraman for his guidance and encouragement during the span of this Master's research.

The author wants to express his gartitude to Mr. Prasad Kalyanaraman and Mr. Douglas James Backes for providing the experimental data. He also wants to thank all members of the research group for their support and friendship during the past four years.

## TABLE OF CONTENTS

List of Tables.....	viii
List of Figures.....	ix
1. Introduction.....	1
2. Binder Dissolution and Process Model.....	6
2.1 Binder Dissolution and Resin Viscosity.....	6
2.2 Resin Viscosity Model.....	10
2.3 Binder Dissolution Model.....	11
2.4 Process Model.....	14
2.41 Momentum balance.....	14
2.42 Energy balance.....	14
2.43 Mass balance.....	15
2.44 The boundary conditions.....	15
2.45 The numerical scheme.....	16
2.5 Model Validation and Prediction of Binder Dissolution.....	17
3. Process Simulations and Control.....	24
3.1 Resin Viscosity Variations.....	24
3.11 RTM simulations without binder.....	24



3.12 S-RIM simulations without binder.....	28
3.13 RTM simulations with binder.....	31
3.2 Design Guidelines.....	31
4. Transverse Permeability.....	35
4.1 Permeability Prediction.....	35
4.2 Finite Element Analysis.....	40
4.21 Numerical scheme.....	40
4.22 Numerical results.....	44
4.3 Transverse Permeability Model.....	48
4.31 Structural parameters.....	48
4.32 Decoupling of 3-D flow field.....	48
4.33 Model prediction and comparisons with FEA results.....	52
4.4 Experimental Validation.....	60
4.41 Experimental.....	60
4.42 Comparison with experimental data.....	62
5. In-plane Permeability.....	69
5.1 In-plane Permeability Prediction.....	69
5.2 Finite Element Analysis.....	70
5.21 Numerical scheme.....	70
5.22 Numerical results.....	73
5.3 In-plane Permeability Model.....	81
5.31 Flow through a channel.....	81
5.32 Model prediction and comparisons with FEA results.....	84

5.4 Experimental Validation.....	84
6. Conclusions and Recommendations.....	92
6.1 Conclusions.....	92
6.2 Scope of Future Work.....	94
Bibliography.....	96

## **LIST OF TABLES**

Table 4.1: Specifications of bi-directional fiber mats .....	62
Table 4.2: Transverse permeability for asymmetric pitched bi-directional fiber mats.....	66

Fi

Fi

Fi

Fi

Fi

Fi

Fi

Fi

Fi

Fi

Fi

Fi

Fi

Fi

Fi

Fi

Fi

## LIST OF FIGURES

Figure 2.1: Viscosity variation of a vinyl ester resin with % weight binder .....	8
Figure 2.2: Causes of non-uniformity during mold filling .....	9
Figure 2.3: Test of binder contribution in viscosity model .....	12
Figure 2.4: The flow scheme for mold filling .....	18
Figure 2.5: Comparison of predicted and experimental binder washout curves .....	19
Figure 2.6: Resin temperature transients for non-isothermal radial filling .....	21
Figure 2.7: Predicted binder concentration profile for isothermal mold fill .....	22
Figure 2.8: Predicted binder concentration profile for non-isothermal mold fill .....	23
Figure 3.1: Viscosity profile at different initial temperature, RTM without binder .....	26
Figure 3.2: Viscosity profile at different mold wall temperature, RTM without binder ...	27
Figure 3.3: Viscosity profile at different initial temperature, SRIM with out binder .....	29
Figure 3.4: Viscosity profile at different mold wall temperature, SRIM without binder ..	30
Figure 3.5: Viscosity profile at different mold wall temperature, RTM with binder .....	32
Figure 3.6: Variation of viscosity gradient with ratio og fill time to dissolution time .....	34
Figure 4.1: Fiber arrangement in an aligned stack of bidirectional fiber mats .....	39
Figure 4.2: Computational cell for transverse permeation (z-direction) .....	41
Figure 4.3: The 3-D mesh for transverse permeation .....	43

Figure 4.4: 3-D velocity field for transverse permeation .....	45
Figure 4.5: Pressure distribution for transverse permeation .....	46
Figure 4.6: Numerical results of transverse permeability .....	47
Figure 4.7: Three-dimensional repeat unit for transverse flow (z-direction) .....	49
Figure 4.8: Comparison between numerical results and Eq. (4.16), $l_x=l_y$ .....	54
Figure 4.9: Comparison between numerical results and Eq. (4.16), $l_x \neq l_y$ .....	55
Figure 4.10: Comparison between numerical results and Eq. (4.16), $l_x \neq l_y$ .....	56
Figure 4.11: Comparison between numerical results and Eq. (4.19), $l_x=l_y$ .....	57
Figure 4.12: Comparison between numerical results and Eq. (4.19), $l_x \neq l_y$ .....	58
Figure 4.13: Transverse permeability for bi-directional and unidirectional arrays .....	59
Figure 4.14: Predicted transverse permeability verse ratio of pitch distances .....	61
Figure 4.15: Comparison of model prediction and experimental data (cross-plyed) .....	64
Figure 4.16: Comparison of model prediction and experimental data (Cofab) .....	65
Figure 4.17: Comparion between existing models and the experimental data .....	67
Figure 5.1: Computation cell for in-plane permeation .....	71
Figure 5.2: The 3-D mesh for in-plane permeation .....	72
Figure 5.3: 3-D velocity field for in-plane permeation .....	74
Figure 5.4: Pressure distribution for in-plane permeation .....	75
Figure 5.5: Contour of the periodic velocity boundary condition .....	76
Figure 5.6: Numerical results of in-plane permeability .....	77
Figure 5.7: The anisotropy of the symmetric pitch .....	78
Figure 5.8: The anisotropy of an asymmetric pitch .....	79
Figure 5.9: The anisotropy of an asymmetric pitch .....	80

Figure 5.10: Channel cross section shape of in-plane permeation .....	82
Figure 5.11: Comparison of numerical results and model prediction, $l_x=l_y$ .....	85
Figure 5.12: Comparison of numerical results and model prection, $l_x \neq l_y$ .....	86
Figure 5.13: Comparison of model prediction and experimental data (cross-plyed) .....	87
Figure 5.14: Comparison of model prediction and experimental data (Cofab) .....	88
Figure 5.15: Comparion between expermental data and Carman-Kozeny equation .....	90
Figure 5.16: Comparion between expermental data and Carman-Kozeny equation .....	91

## ***Chapter 1 INTRODUCTION***

Liquid composite molding process, including Resin Transfer Molding (RTM) and Structural Reaction Injection Molding (S-RIM), involves injection of reactive resin into a mold cavity with pre-placed fiber preforms. The resin then polymerizes and solidifies within the interstices of the fibers to form the final composite structure. It has attracted much research interest in recent years due to its potential application in automotive industry.

Compared to other manufacturing processes, RTM and S-RIM have a variety of advantages including design flexibility to mold large and complex parts, rapid production cycle time, greater reproductivity, and better potential for automation. All these have made liquid molding process a good candidate for the production of high performance parts. Hence there is a growing need to fully understand the mold filling process of liquid composite molding.

Darcy's law, a macroscale model for flow of incompressible, Newtonian fluids through porous media, is often employed to model the mold filling process. Based on Darcy's law, the superficial velocity is related linearly to the resin pressure gradient by the ratio of preform permeability to the resin viscosity as shown in Eq. (1.1) for one dimensional flow.



$$u = \frac{Q}{A} = - \frac{K}{\mu} \frac{dP}{dx} \quad (1.1)$$

here  $P$  denotes resin pressure,  $x$  denotes the coordinate along the flow direction,  $u$  is the superficial velocity,  $Q$  is the volumetric flow rate,  $A$  is the total area of cross section for flow,  $K$  is the permeability determined by preform architecture, and  $\mu$  is the resin viscosity. The ratio of  $K/\mu$  is called mobility, which governs the flow patterns and filling cycle time.

The resin viscosity may vary during the mold filling process. For the S-RIM process, where a fast reacting resin is used, a viscosity change could be caused by heat transfer and chemical reactions. For the RTM process, where resin reaction is slow, resin viscosity will be mainly affected by heat transfer. When the preforms used in the RTM process have resin soluble polymeric binder on them, the dissolved binder concentration in resin could become another major factor that affects resin viscosity. Although binder dissolution can play a crucial role in the RTM process, it has received little attention from researchers.

Preform permeability is a measure of the ease of penetration of the resin into the preform. It is governed by the architecture of the preform. The preform permeability is typically anisotropic. Mathematically it can be expressed as a second order tensor with nine components.

$$\underline{\underline{K}} = \begin{bmatrix} K_{11} & K_{12} & K_{13} \\ K_{21} & K_{22} & K_{23} \\ K_{31} & K_{32} & K_{33} \end{bmatrix} \quad (1.2)$$

Darcy's law can be generalized to multidimensional flow as follows.

$$\vec{u} = -\frac{\underline{\underline{K}}}{\mu} \cdot \nabla P \quad (1.3)$$

For layered preforms, three components of the permeability dyadic can be readily identified along the principal directions.

$$\underline{\underline{K}} = \begin{bmatrix} K_{11} & 0 & 0 \\ 0 & K_{22} & 0 \\ 0 & 0 & K_{33} \end{bmatrix} \quad (1.4)$$

Usually these permeability components are classified as the in-plane permeability ( $K_{11}$  and  $K_{22}$ ) and the transverse permeability ( $K_{33}$ ). The in-plane permeability governs the permeation within the plane of the layers, while the transverse permeability controls the flow through the thickness of the layers.

Since the mat or fabric and the assembling of preforms for thicker, three dimensional structures are particularly expensive, the injection of resin into these preforms must be closely controlled to avoid enormous waste. Hence it is essential to understand the permeation characteristics of a variety of thick and layered preforms. The permeation in regular arrays of aligned, unidirectional cylinders has been studied extensively with theoretical analysis, numerical simulations, and experimental measurements. However, very little work has been done for more complex preform architectures.

The purpose of this thesis is to develop reliable and robust models to describe the resin viscosity variation during mold filling and to predict the permeability based on the preform architecture. The effects of binder dissolution as well as heat transfer, and chemical reaction on resin viscosity will be considered. The work on permeability modeling will focus on bi-directional preforms, which is a key building block for more complicated preform architecture.

The objectives of this thesis are to:

- (1) Analyze the experimental data obtained from our laboratory on RTM with binder dissolution and develop a mathematical model with the help of this data, for the mass transfer of binder from the preform to the resin.
- (2) Combine the mass transfer model with a viscosity model and other conservation equations to predict the resin viscosity variation in the mold. The model takes into account three factors that affect resin viscosity: binder dissolution, heat transfer, and chemical reaction.
- (3) Perform numerical simulations with this model to provide quick estimates of viscosity variation under various process conditions, as well as design guidelines related to binder dissolution during mold filling.
- (4) Perform numerical simulations of the three dimensional flow in idealized bi-directional fiber arrays with the help of FIDAP, a finite element fluid dynamics analysis package developed by Fluid Dynamics International [1], and obtain numerical results for both in-plane and transverse permeability of bi-directional fiber arrays under various structure arrangements.
- (5) Develop analytical expressions with appropriate simplifications of the 3-D flow

solut

pred

solutions for the in-plane as well as the transverse permeability, and test the model predictions with experimental data.

## 2.1 Bind

A c  
together du  
top of one  
be greatly  
of the spra  
rather ther  
polymer v  
different f  
and to imp

A  
of low mo  
ester resin  
preform. I  
[2]. The

## ***Chapter 2 BINDER DISSOLUTION AND PROCESS MODEL***

### **2.1 Binder Dissolution and Resin Viscosity**

A chemical binder is used to hold the non-woven continuous strand fiber mats together during handling. Non-woven fiber mats do not need to be precisely aligned on top of one another as the directional, woven glass fabric. Hence, the production time can be greatly reduced. The binder is applied by spray coating it onto the fiber mat. Because of the spraying method used, the binder is present in small pockets on the fiber bundles rather than being evenly spread across the fibers. The binder is usually a thermoplastic polymer which allows thermoforming of glass fiber mats into preforms. The binder is different from sizing that is applied on glass fiber to protect the fiber itself from damage and to improve adhesion between the fiber and the resin.

A typical binder used in thermoformable glass mats is a thermoplastic polyester of low molecular weight. Such binders are soluble in unsaturated polyester resin or vinyl ester resin formulations. A binder that dissolves in resin allows faster wet out of the preform. Dissolved binder in the resin also leads to reduced shrinkage -- see Owen et al. [2]. The solubility of the binder in resin is varied for different applications;

therm

polye

with

cause

to un

rate a

indica

import

Backes

fold wh

2.1. Als

so that b

filling.

A

pressure

during m

hinder we

mobility a

instabilitie

causes of n

of Figure 2

mold wall l



thermoformable glass fiber mats contain 4 to 10 weight percent of a thermoplastic polyester binder. Uneven dissolution of binder in resin within the filled mold may occur with the lowest concentration near the inlet and the highest near the other end. This will cause a distribution of properties such as stiffness in the molded part [2]. It may also lead to uneven shrinkage that generates large thermal stresses in the part. Also, the reaction rate and exotherm may be decreased by the presence of the thermoplastic binder as indicated by the work of Lee and coworkers [3] on low profile additives. Hence, it is important to predict the distribution of binder within the resin during the filling process.

Another consequence of binder dissolution is an increase in the resin viscosity. Backes et al. [4] have reported that the viscosity of a vinyl ester resin increases nearly two fold when the binder concentration in the resin reaches about 5 wt%, as shown in Figure 2.1. Also the dissolution time is found to be much less than the gel time of RTM resins, so that binder dissolution will have significant effects on the viscosity profile during mold filling.

As shown in Eq. (1.1) increased resin viscosity will require a higher injection pressure for the same injection rate. This may give rise to preform compaction effects during mold filling -- see Han et al. [5] and Mishra and Jayaraman [6] -- which will hinder wet-out and generate inhomogeneities. Finally, increasing viscosity or decreasing mobility along the injection flow direction favors the development of "fingering" flow instabilities, which give rise to inhomogeneities in the molded part. The interlinked causes of non-uniformities developed during mold filling are displayed in the schematic of Figure 2.2. This figure displays three causes of viscosity variation -- binder dissolution, mold wall heating, and cure exotherm during reactive filling. Hence, it is important to

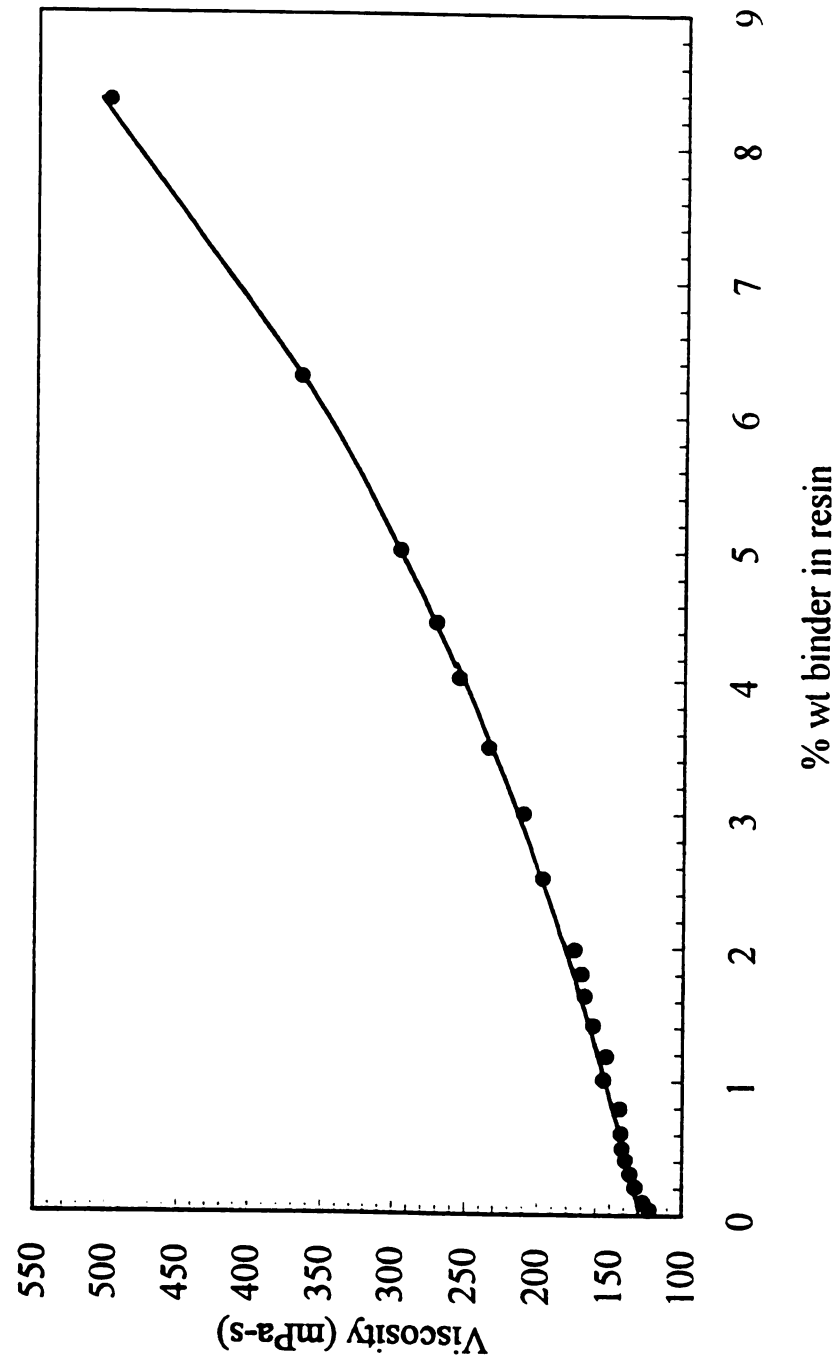


Figure 2.1: Viscosity variation of a vinyl ester resin with % weight binder

NON-UNIFORMITY IN MOLD FILLING

## NON-UNIFORMITY IN MOLD FILLING

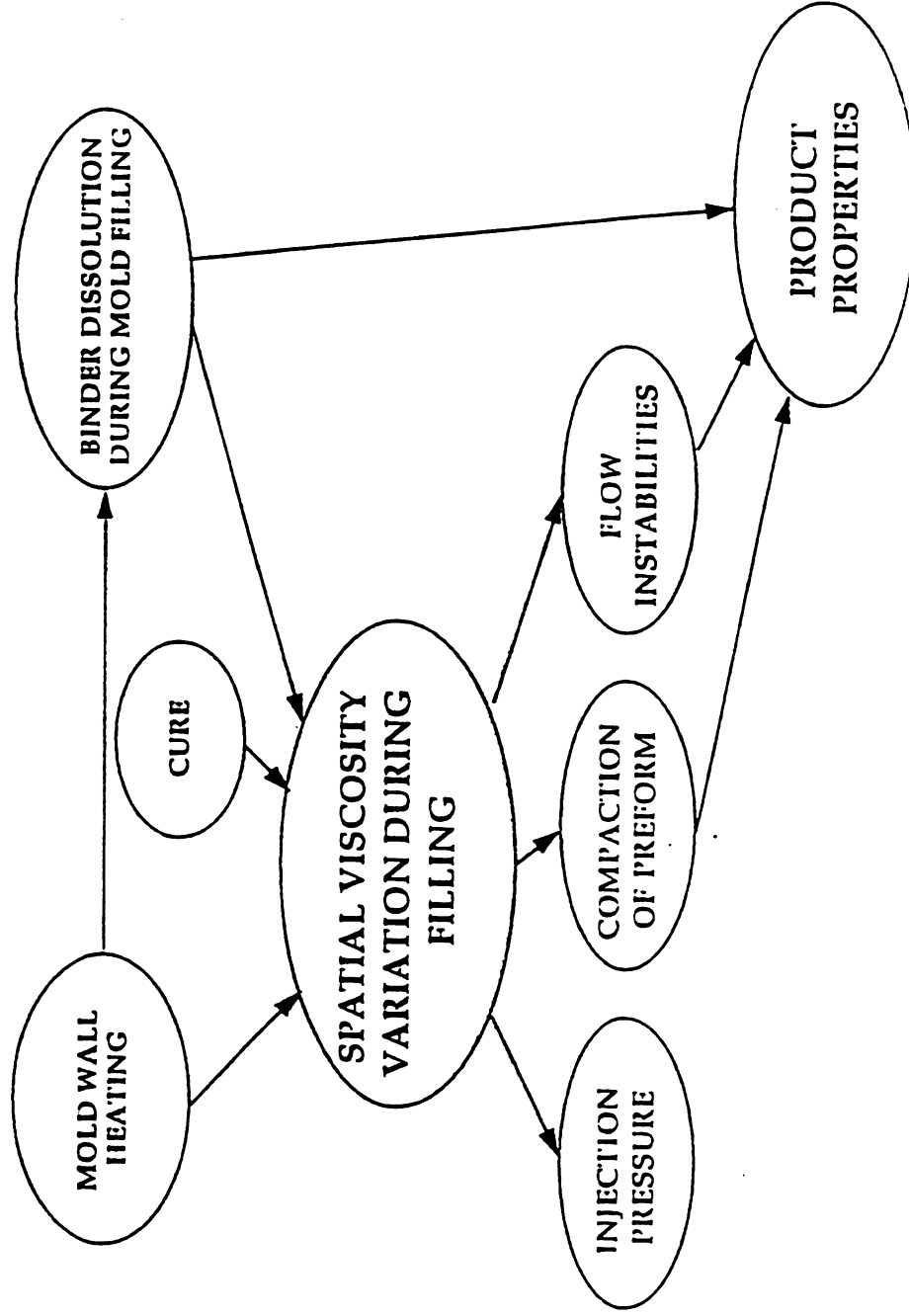


Figure 2.2: Causes of non-uniformity during mold filling

pre

in r

com

heat

anisc

How

vari

dissol

for bi

viscos

**2.2 Re**

first ste

concentr

dissoluti

is found

predict variations in resin viscosity (mobility) during mold filling.

Numerical modeling of mold filling process has been studied by many researchers in recent years [7]. Computer programs have been developed to predict flow through complex shaped fiber preforms [8-10]. Some mold filling simulations incorporate both heat transfer and chemical reaction aspects [11-13]. These address resin flow through anisotropic fiber preforms, heat transfer between resin and fiber, and resin curing. However, not enough attention has been given to resin viscosity as an intermediate variable to control the flow uniformity. No previous model has included the binder dissolution process. The model described in this thesis combines a mass transfer model for binder dissolution and other conservation equations to estimate the variation of resin viscosity due to binder dissolution, mold heating , and resin curing.

## 2.2 Resin Viscosity Model

In order to take into account the three factors that affect the resin viscosity, the first step of modeling is to describe the resin viscosity as a function of binder concentration, temperature, and conversion for mold filling processes coupled with binder dissolution. For the Derakane vinyl ester resin used in our lab, the following expression is found to fit experimental measurements [4],

$$\mu(T, \alpha, c_b) = \mu_0(T) \times f_1(c_b) \times f_2(\alpha) \quad (2.1)$$

where th

here T d

$\alpha_g$ , gel c

viscosity

conversio

## 2.3 Bind

A

the static

here  $K_m$

solubility

concentra

flow thro

transfer co

where the temperature, binder concentration, and conversion effects are

$$\mu_0(T) = \exp(-15.3 + \frac{5981.5}{T}) \text{ (mPa-s)} \quad (2.2)$$

$$f_1(c_b) = 1.0 + 0.1841 c_b + 8.2978 \times 10^{-3} c_b^2 + 1.4278 \times 10^{-3} c_b^3 \quad (2.3)$$

$$f_2(\alpha) = (1 - \frac{\alpha}{\alpha_g})^{(-3.32 \times \frac{\alpha}{\alpha_g} - 0.66)} \quad (2.4)$$

here  $T$  denotes temperature,  $c_b$ , binder concentration in resin in wt%,  $\alpha$ , conversion, and  $\alpha_g$ , gel conversion which is 0.015 for the Derakane vinyl ester resin. The experimental viscosity data and the predicted viscosity from Eq. (2.1) are plotted in Figure 2.3 for zero conversion case.

### 2.3 Binder Dissolution Model

An expression for the rate of binder dissolution,  $R_b$ , has been developed first from the static experiments [4],

$$R_b = K_m a_m (b w_b - \frac{\phi}{1-\phi} c_b) \quad (2.5)$$

here  $K_m$  is the mass transfer coefficient,  $a_m$  is the surface area per unit volume,  $b$  is solubility coefficient,  $w_b$  is binder concentration on fiber ( $\text{g/cm}^3$  fiber volume),  $c_b$  is binder concentration in resin ( $\text{g/cm}^3$  resin volume), and  $\phi$  is porosity. The dissolution data for flow through a rectangular mold [4] is fitted with the following correlation for mass transfer coefficient between fluid and porous media (see Smith [14]),



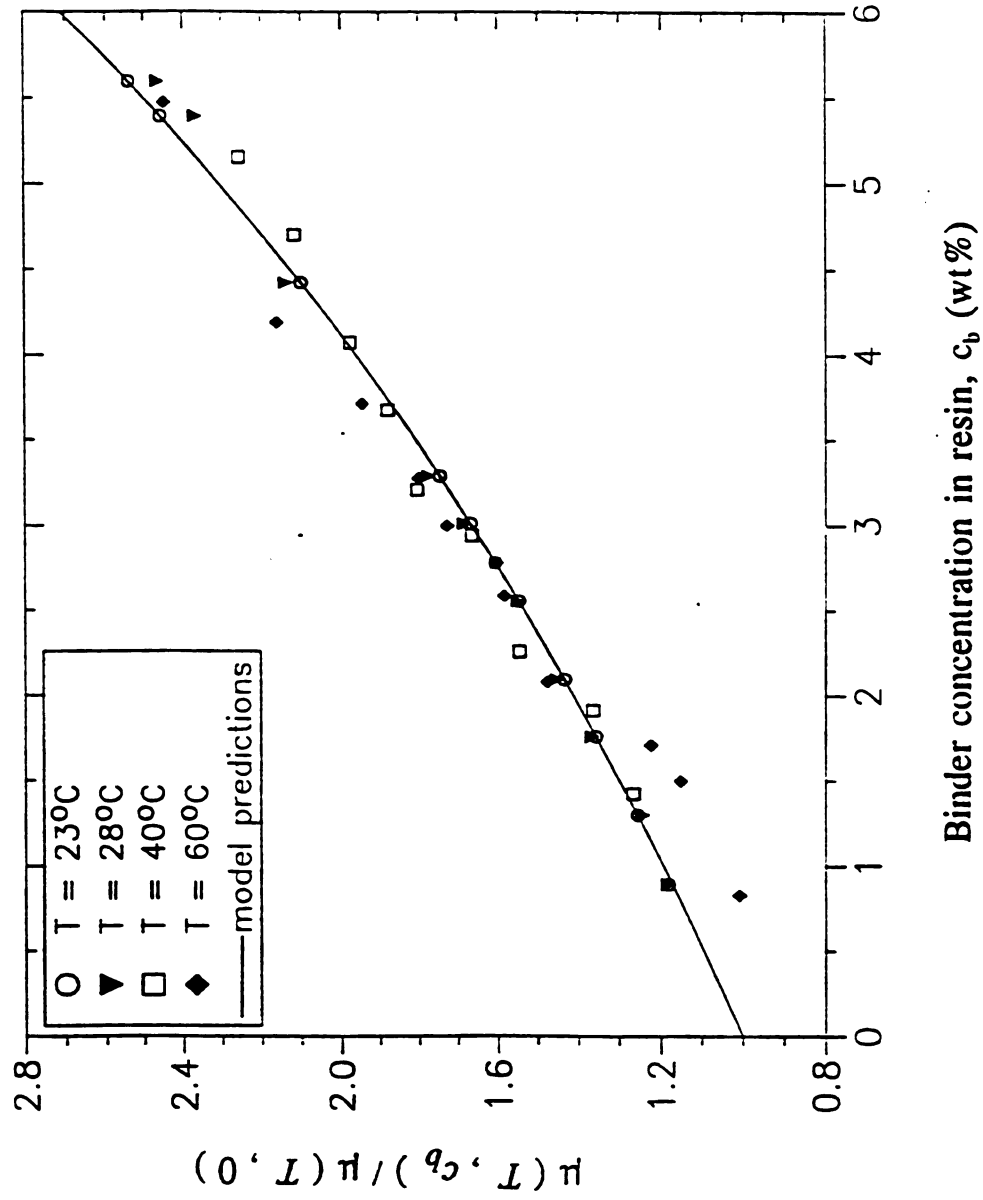


Figure 2.3: Test of binder contribution in viscosity model

here  $u$  is

resin.  $d_p$

data fitting

given by

Here  $\kappa$  is

the mass

where

Eq. (2.8)

binder dis

$$\frac{K_m \phi}{u} = \beta_1 \left( \frac{\mu}{\rho D} \right)^{-2/3} \left( \frac{d_p \rho u}{\mu} \right)^n \quad (2.6)$$

here  $u$  is superficial velocity,  $\rho$  is density,  $D$  is the molecular diffusivity of the binder in resin,  $d_p$  is the fiber bundle diameter,  $\beta_1$  and  $n$  are constants to be determined through data fitting. The change of diffusivity with temperature can be found from the correlation given by Bird et al. [15].

$$D = \frac{\kappa T}{6\pi R_A \mu} \quad (2.7)$$

Here  $\kappa$  is the Boltzman constant, and  $R_A$  is the diffusive radius of binder particles. Finally, the mass transfer rate can be written as

$$R_b = \beta a_m \frac{u}{\phi} \left( \frac{\mu^2}{\rho T} \right)^{-2/3} \left( \frac{d_p \rho u}{\mu} \right)^n \left( b w_b - \frac{\phi}{(1-\phi)} c_b \right) \quad (2.8)$$

where

$$\beta = \beta_1 \left( \frac{\kappa}{6\pi R_A} \right)^{2/3} \quad (2.9)$$

Eq. (2.8) will then be used with the following component balance equations to predict binder dissolution during mold filling process.

$$\phi \frac{\partial c_b}{\partial t} + u \frac{\partial c_b}{\partial x} = \frac{1-\phi}{\phi} R_b \quad (2.10)$$

$$\frac{\partial w_b}{\partial t} = -R_b \quad (2.11)$$

2.4 Pr

2.41 M

Darcy

2.42 E

assumed

Here T

coefficie

rate,  $\Delta H$

here B is

coefficient

obtained t

## 2.4 Process Model

### 2.41 Momentum balance

For resin flow through continuous strand glass mats (isotropic in the flow plane), Darcy's law is used instead of the momentum balance equations (see Eq. (1.1)).

### 2.42 Energy balance

Both heat transfer between resin and fiber and resin and heated mold wall are assumed to be predominantly due to convection.

$$\rho C_p \phi \frac{\partial T}{\partial t} + \rho C_p u \frac{\partial T}{\partial x} = -\phi Q_B + \phi R_c (-\Delta H) + Q_w \quad (2.12)$$

$$(\rho C_p)_B (1-\phi) \frac{\partial T_B}{\partial t} = \phi Q_B \quad (2.13)$$

Here  $T$  is temperature,  $C_p$  is specific heat,  $t$  is time,  $h_v$  is the volumetric heat transfer coefficient between resin and fiber, subscription  $B$  stands for fiber property,  $R_c$  is reaction rate,  $\Delta H$  is heat of reaction, and  $Q_w$  is heat flux from mold to the resin and fiber bed,

$$Q_w = \frac{h_w}{B} (T_w - T) \quad (2.14)$$

here  $B$  is mold thickness,  $T_w$  is mold wall temperature,  $T$  and  $h_w$  is heat transfer coefficient between fluid and mold wall for flow through porous media. Bejan [16] obtained the following expression from boundary layer analysis.

$Q_B$  is th

here  $T_B$

fiber and

**2.43 M**

T

TI

here  $R_c$  is

balance ec

**2.44 The**

It i

Hence one

$$\frac{h_w}{\rho C_p} = 0.564 \left( \frac{k}{\rho C_p} \frac{u}{x} \right)^{1/2} \quad (2.15)$$

$Q_B$  is the volumetric heat flux between resin and fiber,

$$Q_B = h_v (T - T_B) \quad (2.16)$$

here  $T_B$  is the fiber temperature,  $h_v$  is the volumetric heat transfer coefficient between fiber and resin ( Lin et al, [11]),

$$\frac{h_v}{\rho C_p} = 0.0917 + 0.0195u (\times 10^{-2} m/sec) \quad (2.17)$$

#### 2.43 Mass balance

The continuity equation in one dimensional form is

$$\frac{\partial u}{\partial x} = 0 \quad (2.18)$$

The balance equation for conversion is

$$\phi \frac{\partial \alpha}{\partial t} + u \frac{\partial \alpha}{\partial x} = -\phi R_c \quad (2.19)$$

here  $R_c$  is the rate of reaction, which depends on reaction kinetics of the resin. And the balance equations for binder concentration are listed in Section 2.3.

#### 2.44 The boundary conditions

It is assumed in this model that no reaction occurs before resin enters the mold.

Hence one has

where  $T$

at the fl

here  $T_{Bo}$

**2.45 Th**

$T$

Eq. (2.1

While fo

other cha

The abov

$u$  varies  $v$

For radia



$$\begin{aligned}
 x=0, \quad T &= T_i \\
 \alpha &= 0 \\
 c_b &= 0
 \end{aligned}
 \tag{2.20}$$

where  $T_i$  is initial resin temperature, and  $w_{b0}$  is initial binder content on the fiber.. While at the flow front

$$\begin{aligned}
 x=x_f, \quad T_B &= T_{B0} \\
 w_b &= w_{b0} \\
 P &= 0
 \end{aligned}
 \tag{2.21}$$

here  $T_{B0}$  is initial fiber preform temperature, and  $x_f$  is the flow front position,

## 2.45 The numerical scheme

The above set of equations is solved by the method of characteristic technique[17].

Eq. (2.11) and Eq. (2.13) are numerically integrated along the characteristic line of,

$$t = \text{constant} \tag{2.22}$$

While for Eq. (2.10), (2.12), and (2.19), numerical integration is performed along the other characteristic line,

$$x = \frac{u}{\phi} t + \text{constant} \tag{2.23}$$

The above characteristic lines are for one dimensional rectilinear flow with constant  $u$ . If

$u$  varies with time, a stepwise  $u$  profile that is close to the real  $u$  variation could be used.

For radial flow with constant flow rate, the characteristic lines are,

$$\begin{aligned}
 t &= \text{constant} \\
 r &= \int \frac{u}{\phi} dt + \text{constant}
 \end{aligned}
 \tag{2.24}$$

where  $r$  is the radial distance from the center gate and  $u$  is a function of  $r$ .

## 2.5 Model Validation and Prediction of Binder Dissolution

The present model is confined to one-dimensional flow with negligible heat conduction and dispersion, but it takes into account all three factors that will affect resin viscosity. Such a model can be solved by the method of characteristics [17]. Calculations with this model thus provide quick estimates of viscosity variation under various process conditions. The following simulations are done to check the binder dissolution model and the effects of such simplifications. The preform dimensions for the rectangular mold are 15.56 cm x 56.52 cm x 0.3175 cm (see Figure 2.4).

Three sets of experimental binder concentration data from both isothermal and non-isothermal filling experiments with the rectangular mold [4] have been used to determine the mass transfer parameters,  $\beta$  and  $n$  Eq. (2.8). The isothermal filling was done at 23°C. For the non-isothermal filling, the resin inlet temperature is still 23°C, while the mold wall temperature is at 40°C and 60°C, respectively. The variation of the flow rate during the filling experiments has also been considered by using flow velocities varying stepwise with time. The model predicted outlet binder concentration change with time is plotted in Figure 2.5 with the experimental data (from Backes [4]). The empirical constants,  $\beta$  and  $n$  are determined by fitting the non-isothermal experimental data with 40°C mold wall temperature. The best fit yields  $1.374 \times 10^{-10}$  for  $\beta$  and -0.95 for  $n$ . The same constants are used to predict the binder concentration transients for the other two cases. It can be seen from Figure 2.5 that the numerical results match well with the experimental measurements. The deviation from the experimental data for the isothermal

Ga

u

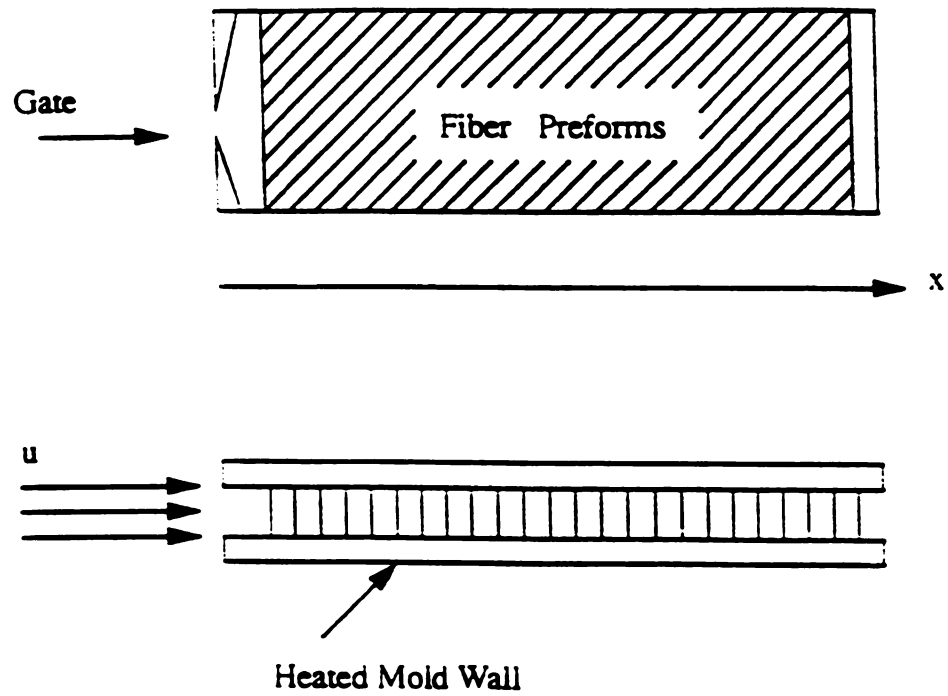


Figure 2.4: The flow scheme for mold filling

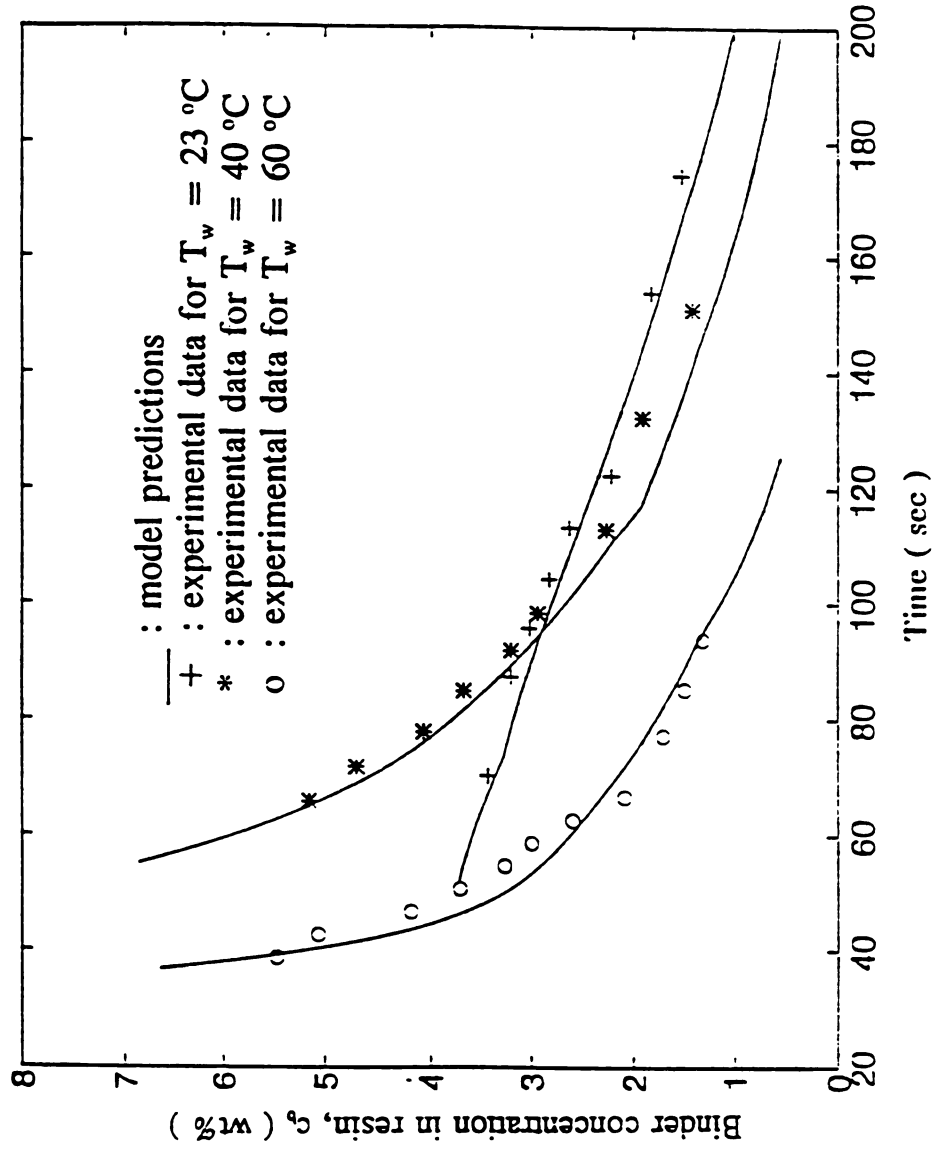


Figure 2.5: Comparison of predicted and experimental binder washout curves

run is less

the mass

In

simulation

gated dis

are the s

given in

numerica

temperatu

with an a

conduction

provides

T

simulation

resin inle

increases

experime

concentra

direction

non-isoth

concentra

temperatu

in resin. 7

run is less than 5% and the deviation for the non-isothermal run is less than 10%. Hence the mass transfer model for binder dissolution in Eqs. (2.5) - (2.8) is valid.

In order to explore the effect of ignoring conduction in the energy balance, another simulation has been carried out for a case studied by Lin et al [11] -- filling of a center-gated disk shaped mold with palatinol oil. The mold dimensions and process conditions are the same as those in [11]. Results of the present simulation are compared with those given in [11]., where a two-dimensional model with heat conduction is used to generate numerical results of temperature distribution. Figure 2.6 shows that the comparison of temperature transients at two different locations in the mold. The same trend is shown with an average difference less than 15%. This shows that despite the omission of heat conduction, the present one-dimension model with mold wall heating as a source term provides good estimates of the temperature profiles.

The binder concentration profile in the mold for a 45 second isothermal filling simulation is shown in Figure 2.7. The simulation was done on the rectangular mold. Both resin inlet and mold wall temperatures are 23 °C. As can be seen, the binder concentration increases along the filling direction. The pattern is qualitatively similar as the experimental results [4]. Since the resin viscosity increases with increased binder concentration, the resin viscosity in this case will increase along the injection flow direction which favors the development of flow instability or "fingers". Another case for non-isothermal filling is shown in Figure 2.8, where resin temperature and binder concentration profiles are plotted together. As can be seen, the increase of resin temperature accelerates the dissolution of binder, which yields higher binder concentration in resin. This is also confirmed by the experiments [4].

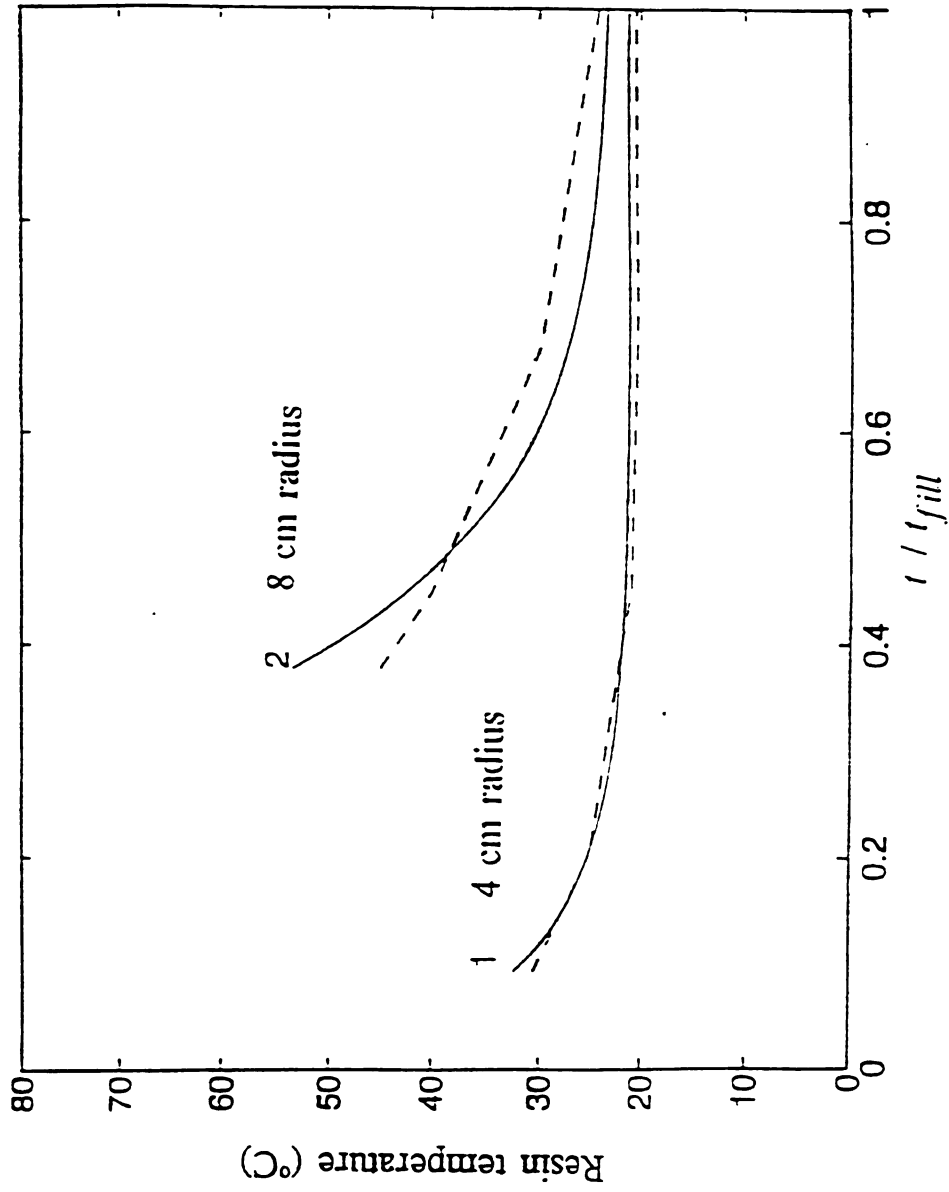


Figure 2.6: Resin temperature transients for non-isothermal radial filling



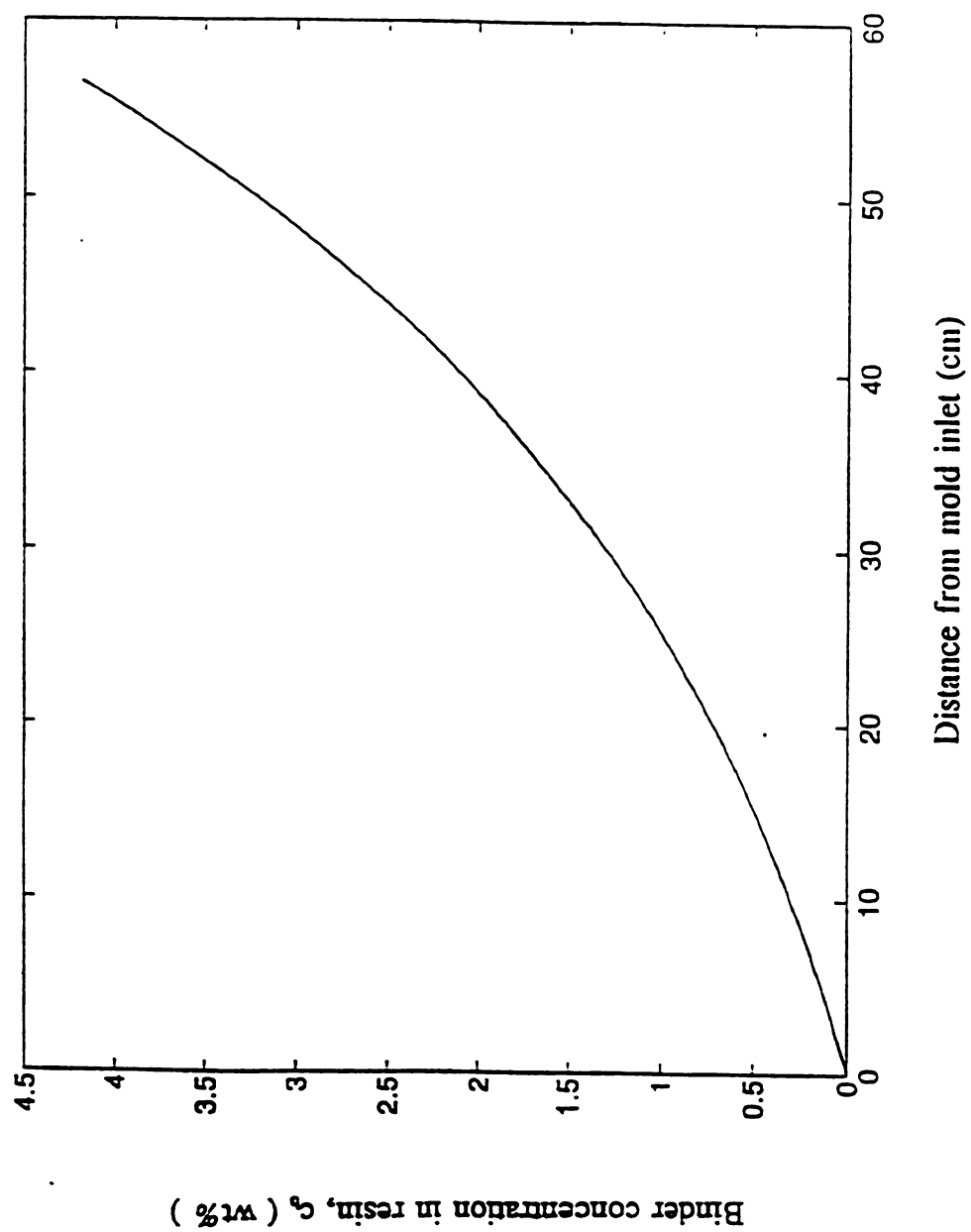


Figure 2.7: Predicted binder concentration profile for isothermal mold fill

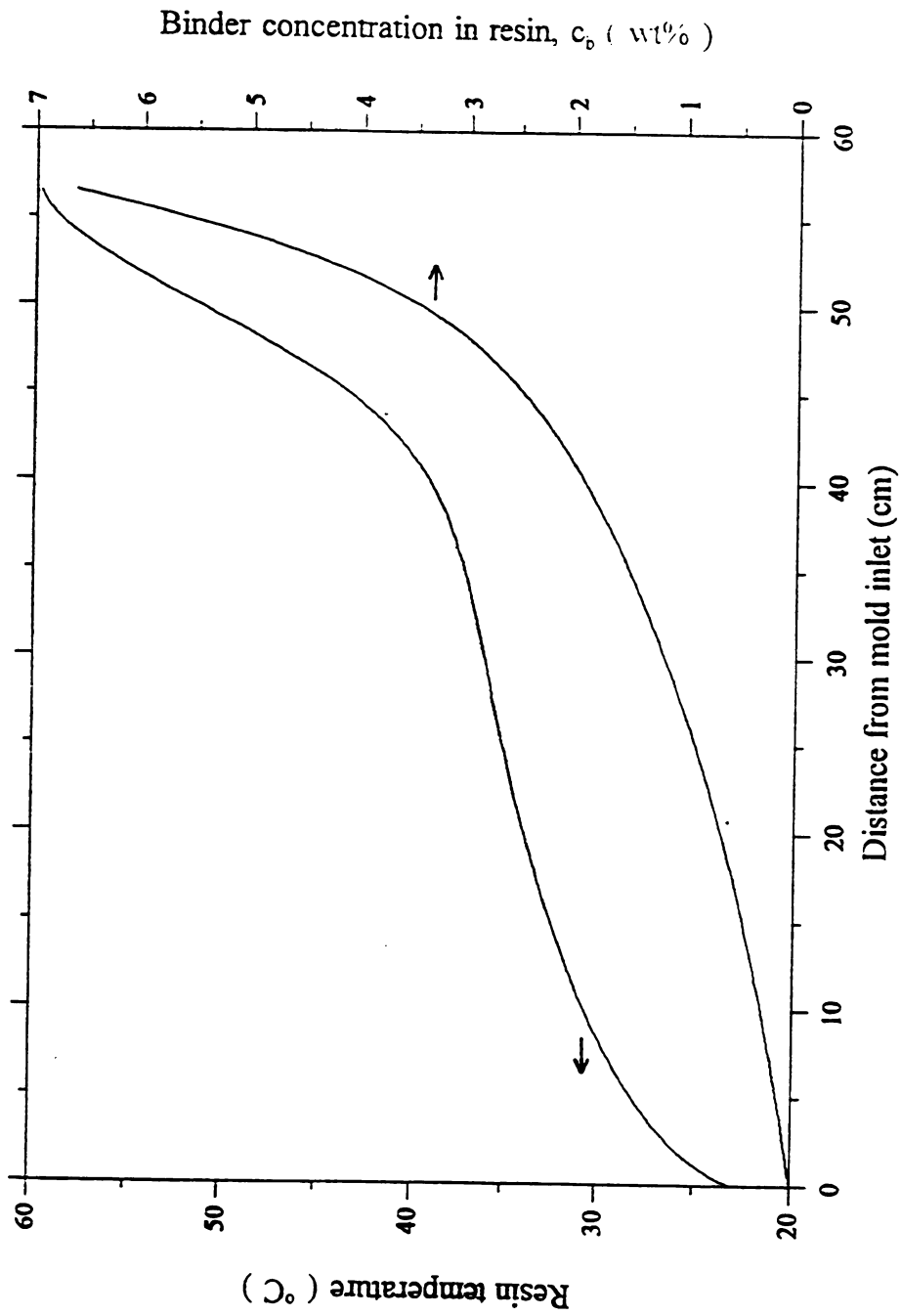


Figure 2.8: Predicted binder concentration profile for non-isothermal mold fill

## ***Chapter 3 PROCESS SIMULATIONS AND CONTROL***

### **3.1 Resin Viscosity Variation**

As pointed out in the previous chapter, the resin viscosity plays an important role during the mold filling process. Resin viscosity, reaction rate, and binder dissolution rate are affected by the resin temperature. Variation in the resin inlet temperature or in the mold wall temperature will have effects on all the three factors that will cause resin viscosity change, which are binder dissolution, heat transfer, and chemical reaction. The process model developed in the previous chapter can be applied to S-RIM as well as RTM processes with or without binder dissolution. Calculations with this model provide quick estimates of viscosity variation under various process conditions. The following set of simulations are done to investigate the effectiveness of using resin inlet temperature or mold wall temperature as a control variable to affect the resin viscosity profile. All these simulations are done on the rectangular mold.

#### **3.11 RTM simulation without binder**

Filling simulations for RTM process are performed on the rectangular mold with a Derakane vinyl ester resin. To isolate the effects of mold wall heating, the simulations are first done for preforms without binder. The base case has the resin inlet temperature

at 25°C and the mold wall temperature at 35°C. Then resin inlet and mold wall temperatures are raised to see its effects on resin viscosity profile. The filling time (45 sec) for all these simulations is much less than resin gel time (about 240 sec at 50°C). The reaction kinetics of the vinyl ester resin has been provided by Larson and Drzal [18].

$$R_c = \frac{k_i(1 - \alpha)}{t_z - t} \quad (3.1)$$

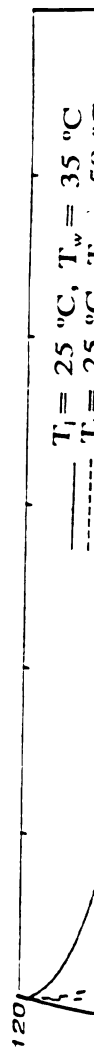
where

$$k_i = 5.69 \times 10^{11} \exp\left(\frac{-10360}{T}\right) \quad (3.2)$$

and

$$t_z = 1.7 \times 10^{-11} \exp\left(\frac{8555}{T}\right) \quad (3.3)$$

Figure 3.1 shows the viscosity profiles for different mold wall temperatures. As can be seen, the increased mold wall temperature results in a larger decrease in viscosity along the mold filling direction. This decreased viscosity or increased mobility profile does not favor the development of flow instability. However, raising the mold wall temperature might also accelerate the reaction. At a mold wall temperature of 60°C there is a small increase in viscosity at the flow front as a result of the reaction. However, for the slow reacting RTM resins, the viscosity increase caused by reaction would be insignificant. When a fast reacting SRIM resin is used, the increase in the reaction rate due to higher mold temperatures could be important (see Figure 3.3). Figure 3.2 shows that raising resin inlet temperature does not affect the viscosity profile to the same extent.



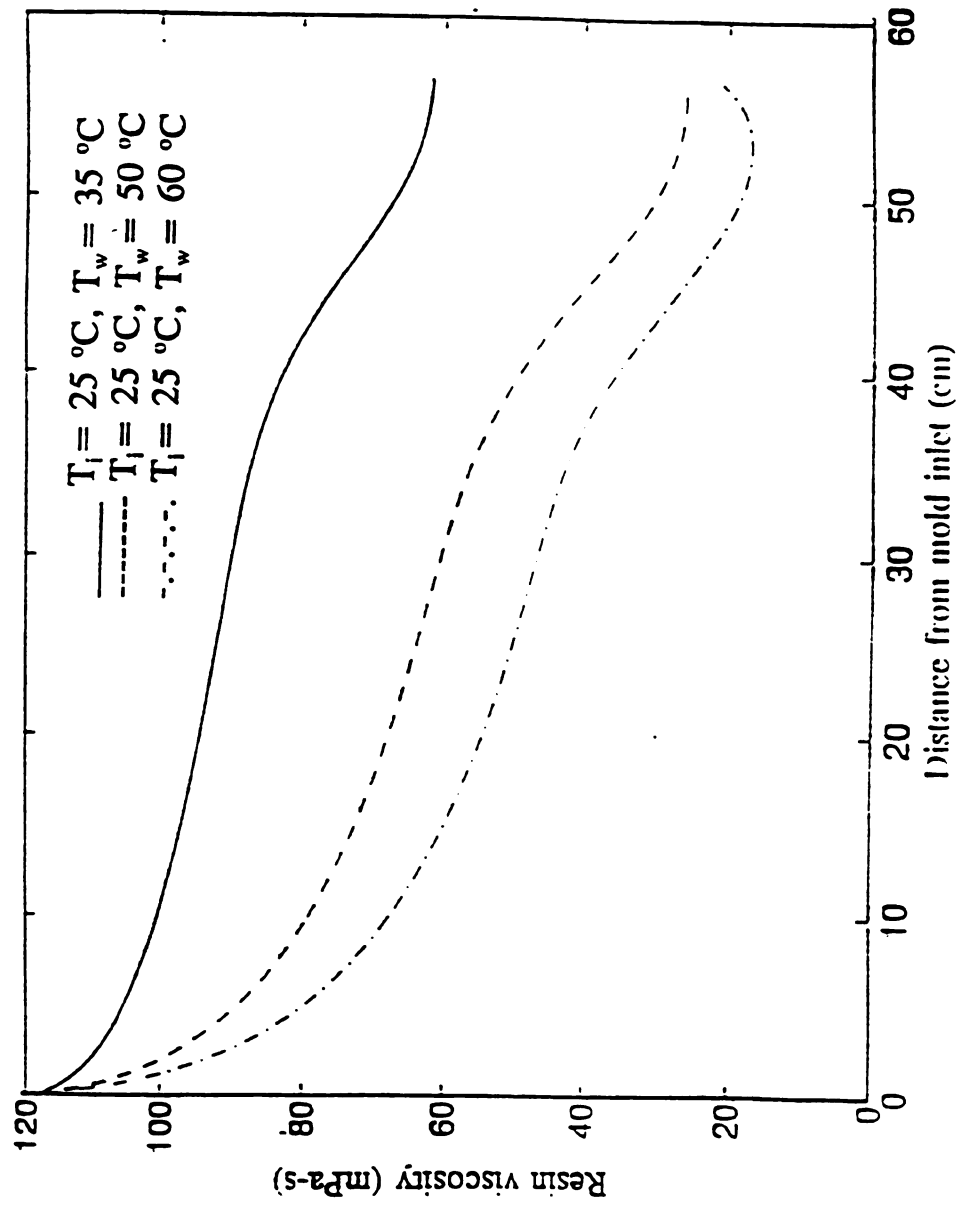


Figure 3.1: Viscosity profile at different mold wall temperature, RTM without binder



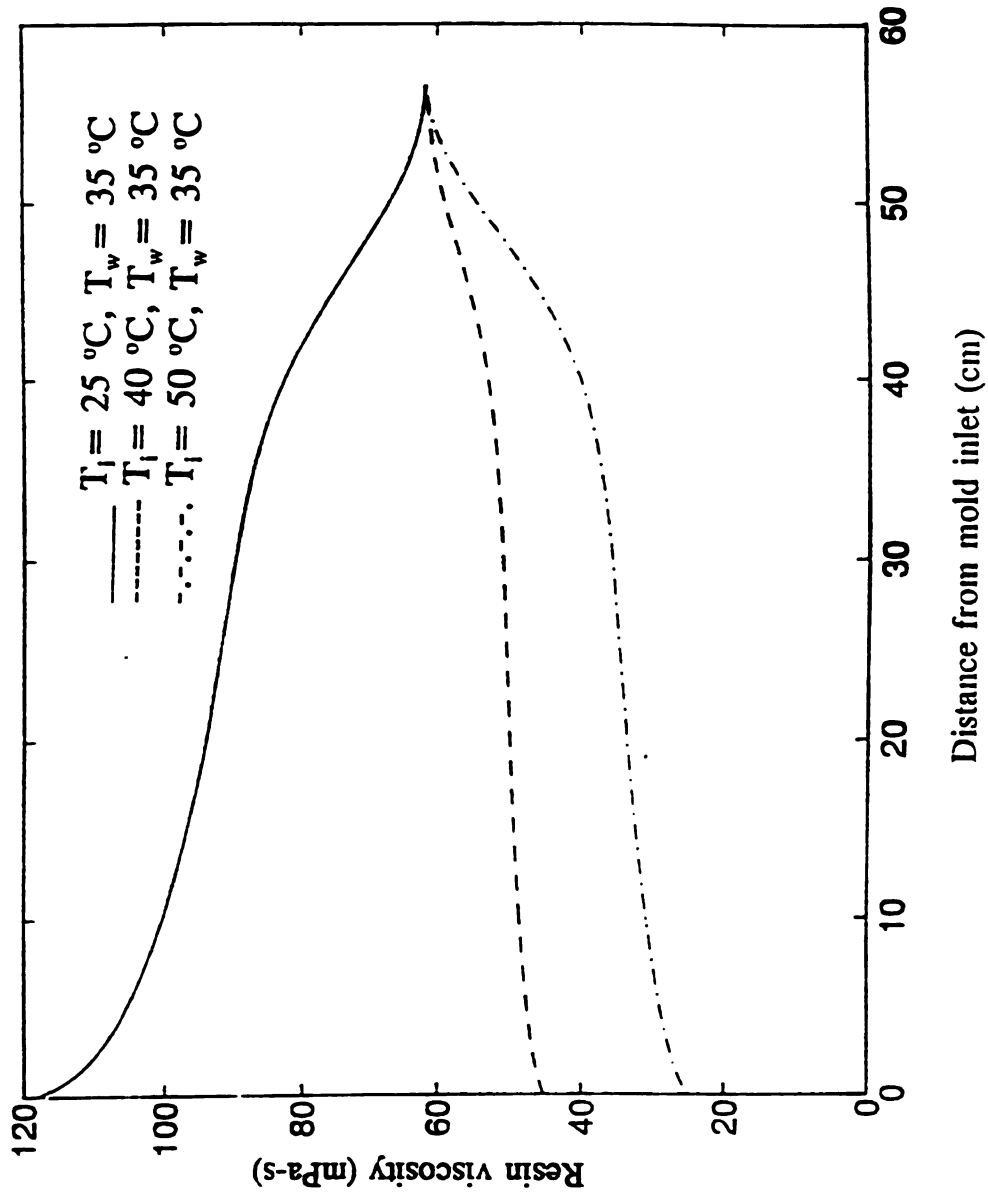


Figure 3.2: Viscosity profile at different initial resin temperature, RTM without binder



### 3.12 S-RIM simulations without binder

Another set of simulations is done for faster reacting polyurethane resins with 25 sec filling time (resin gel time is about 50 sec at 100 °C). The reaction kinetics is given by Lin et al [11],

$$R_c = A_1 e^{-\frac{E_1}{RT}} (\alpha_f - \alpha)^n \quad (3.4)$$

where R is the gas constant,  $A_1$ ,  $E_1$ , and n are constants determined from experiments. Here  $\alpha_f$  can be expressed as

$$\alpha_f = 0.406 e^{2.49 \times 10^3} \quad (3.5)$$

The base case is with a resin inlet temperature of 45 °C and a mold wall temperature of 80 °C. The viscosity profiles along the filling direction under various conditions are plotted in Figures 3.3 and 3.4. It can be seen from Figure 3.3 that for the S-RIM resin a larger viscosity increase caused by reaction occurs when the mold wall temperature is raised from 80 °C to 120 °C. In regions away from the front where conversion is small, higher mold wall temperature still causes resin viscosity to decrease along the flow direction. Hence, care should be taken while choosing the mold wall temperature and the filling time for S-RIM. As shown in Figure 3.4, raising the initial resin temperature yields lower resin viscosity. However, for a 85 °C resin inlet temperature a small viscosity increase can be observed near the end of the mold due to the acceleration of the reaction.

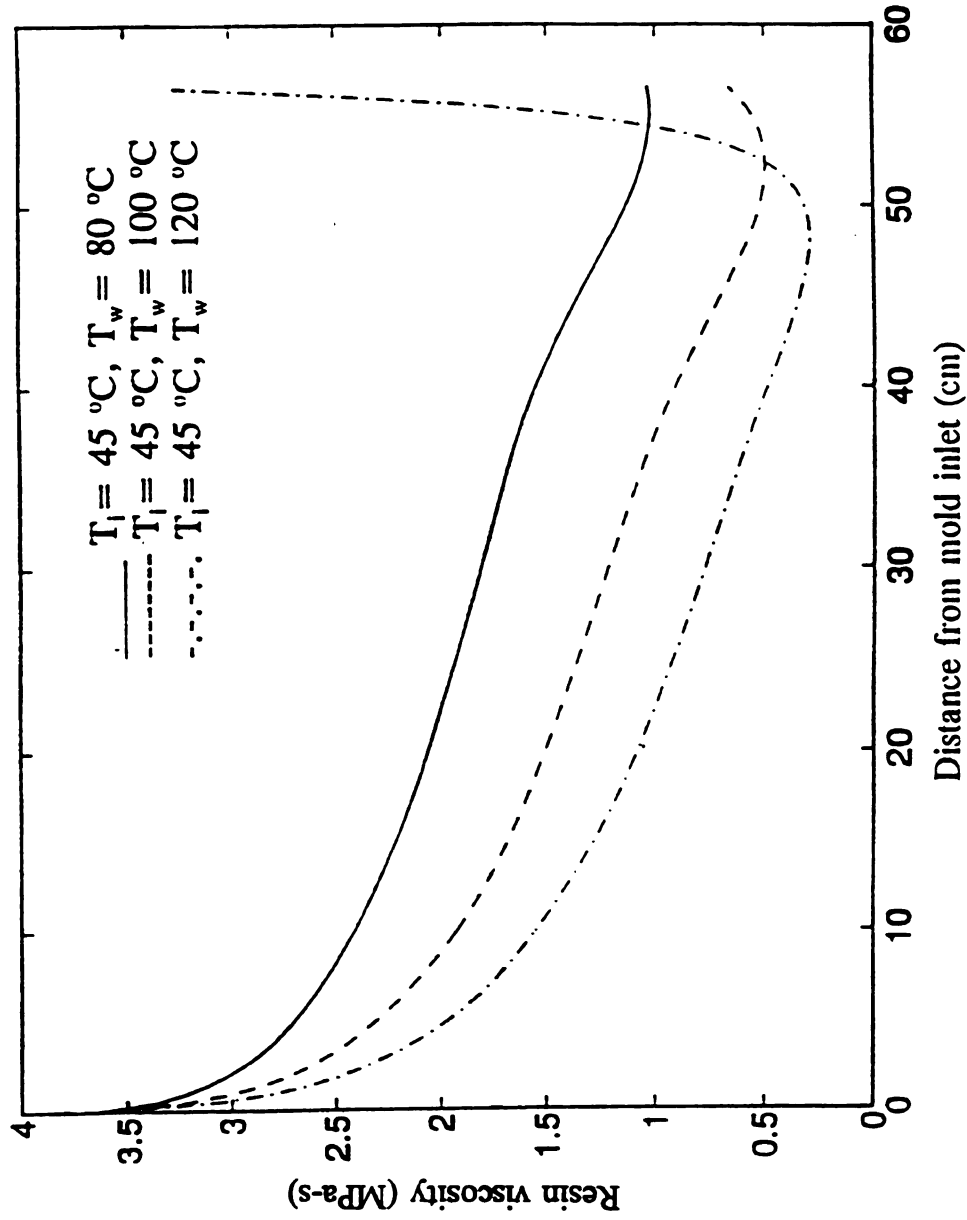


Figure 3.3: Viscosity profile at different mold wall temperature, SRIM without binder

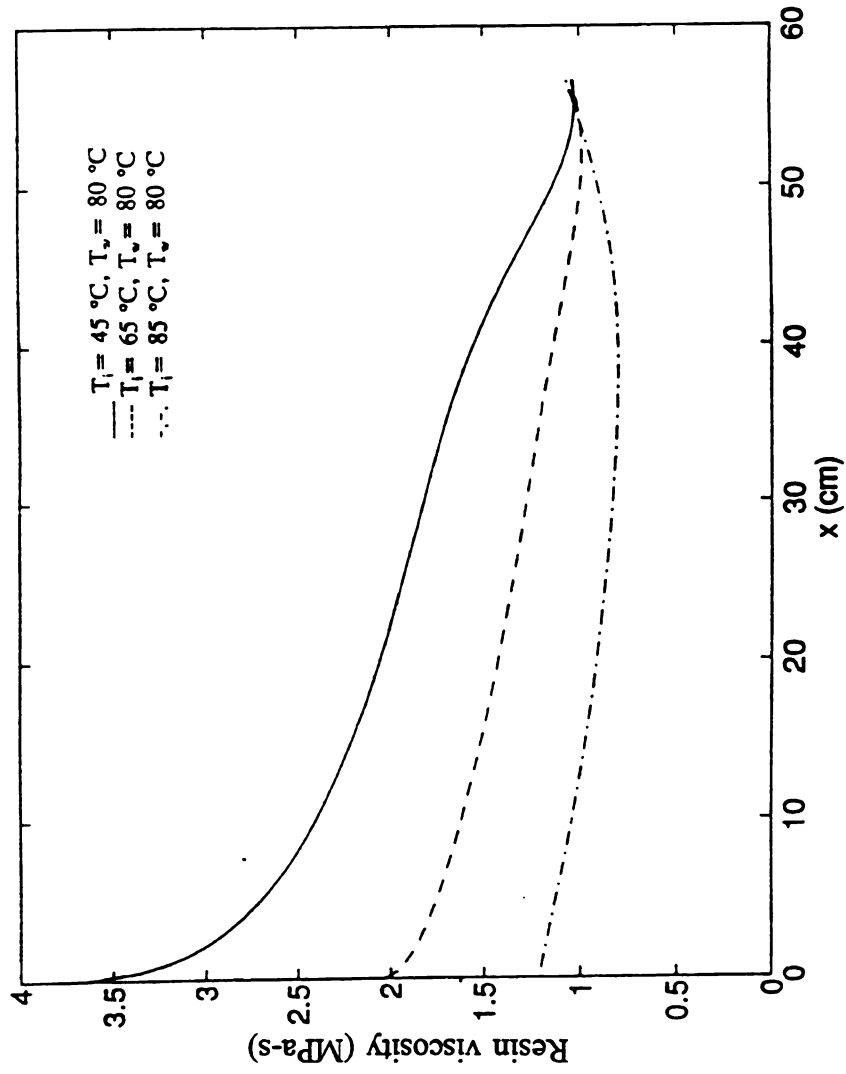


Figure 3.4: Viscosity profile at different initial resin temperature, SRIM with out binder

### 3.13 RTM simulation

Experiment

significant resin vis

of "fingers" and in

mold wall temper

(decrease) along t

be possible to eas

Several simulation

show this point.

with a stepwise w

temperature (35°

dissolved binder.

(see 40°C and 50

local region of v

mold wall temp

### 3.2 Design Gui

If uneve

detrimental to th

either in binder

a window of op

viscosity gradien

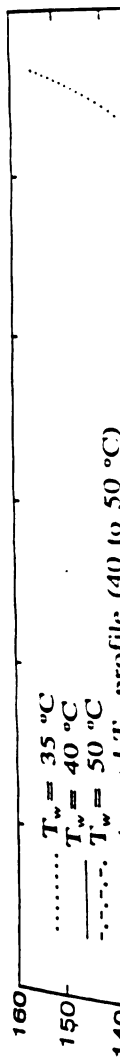
design parameter

### 3.13 RTM simulations with binder

Experimental work [4] has shown that binder dissolution in resin will cause a significant resin viscosity increase along the filling direction, which will lead to formation of "fingers" and inhomogeneity. It has also been shown through above calculations that mold wall temperature can be controlled to produce a negative viscosity gradient (decrease) along the mold. Therefore by controlling the mold wall temperature, it might be possible to ease the increase in viscosity caused by binder concentration in the resin. Several simulations for mold filling with preforms with resin soluble binder are done to show this point. The viscosity profiles with three constant wall temperature levels and with a stepwise wall temperature are shown in Figure 3.5. It shows that for low mold wall temperature (35°C) profile, the resin viscosity will increase along the mold due to dissolved binder. Raising the mold wall temperature will lower the increase in viscosity (see 40°C and 50°C cases). Figure 3.5 also shows that raising the wall temperature in the local region of viscosity increase (stepwise  $T_w$ ) could be more effective than raising the mold wall temperature uniformly in terms of reducing viscosity gradient.

### 3.2 Design Guidelines

If uneven binder dissolution and increasing viscosity in the direction of flow are detrimental to the properties of the molded part, a threshold of gradient may be identified either in binder concentration or correspondingly in the viscosity. Then one may define a window of operating conditions for which the binder concentration gradient or the viscosity gradient will be below the agreed upon threshold. As an example, an important design parameter is the ratio of fill time,  $t_{fill}$  to a characteristic dissolution time  $t_{diss}$ . This



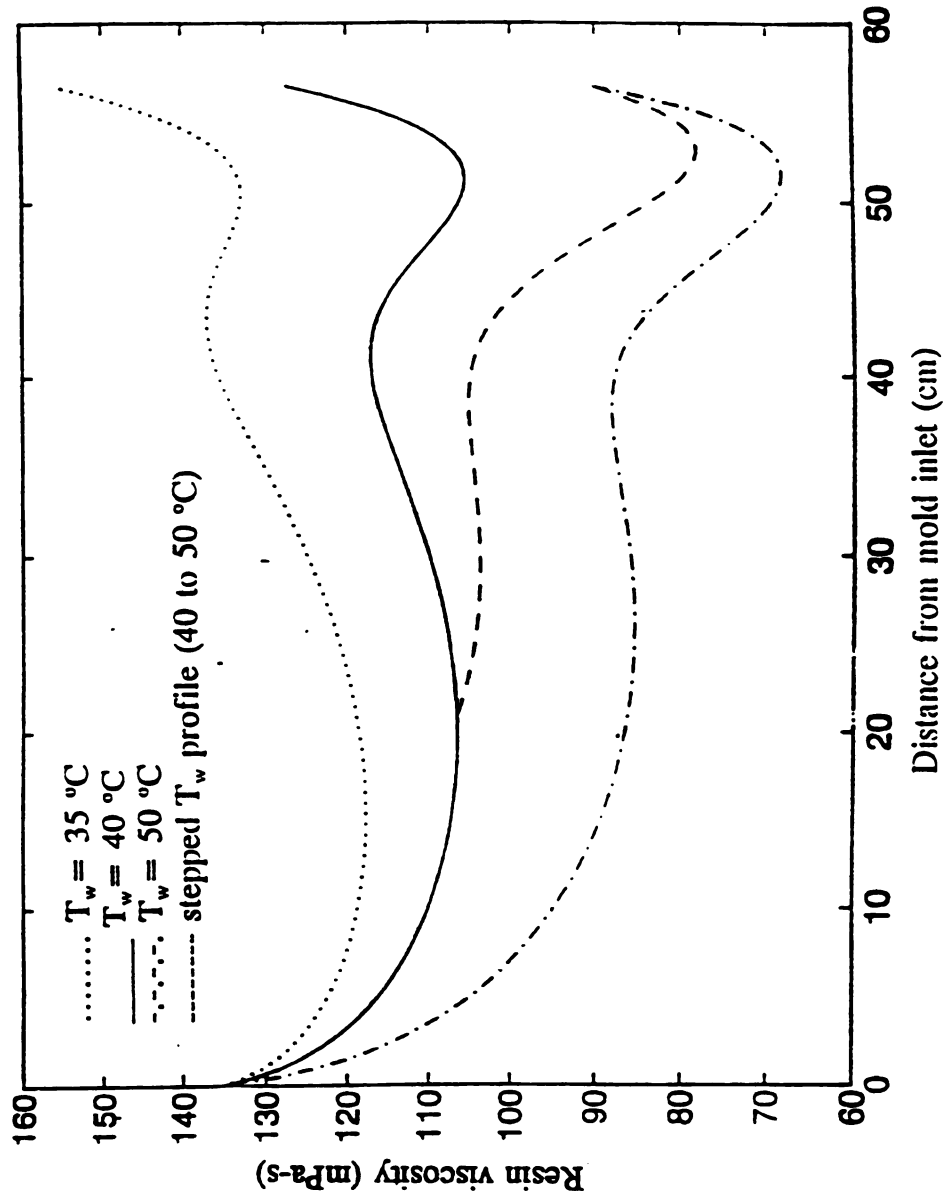


Figure 3.5: Viscosity profile at different mold wall temperature, RTM with binder

ratio may be comp

where the front lo

A small ratio of  
enough time for  
dissolved in resi

The loga  
the fill time to t  
wall temperatur  
ratio of fill time  
at low ratios the  
wall temperatur  
heat has been tra  
time to dissolutio  
becomes larger  
temperature since  
a viscosity gradie  
percent of the dis.



ratio may be computed by the following relation,

$$\frac{t_{fill}}{t_{diss.}} = \int_0^L \frac{K_m a_m}{u} dx \quad (3.6)$$

where the front location is denoted by  $L$  and mold fill time is given by

$$t_{fill} = \int_0^L \frac{dx}{u} \quad (3.7)$$

A small ratio of filling time to the characteristic dissolution time means that there is not enough time for the binder to be dissolved. If the ratio is large, the binder concentration dissolved in resin will be high.

The logarithmic viscosity gradient at the flow front is plotted against the ratio of the fill time to the dissolution time in Figure 3.6 for two simulations with different mold wall temperatures. Figure 3.6 shows that the viscosity gradient increases with increasing ratio of fill time to the characteristic dissolution time. The gradient increases more rapidly at low ratios then levels off as the resin nears its solubility limit. Increases in the mold wall temperature will result in a smaller viscosity gradient at low fill times because more heat has been transferred resulting in a higher resin temperature. Then as the ratio of fill time to dissolution time increases (front moving forward), the viscosity gradient eventually becomes larger for the higher mold wall temperature than for lower mold wall temperature since the higher temperature resin will dissolve more binder. If for example, a viscosity gradient of zero is used as a threshold, the fill time should be less than 5 percent of the dissolution time scale at a mold wall temperature of 35 °C.



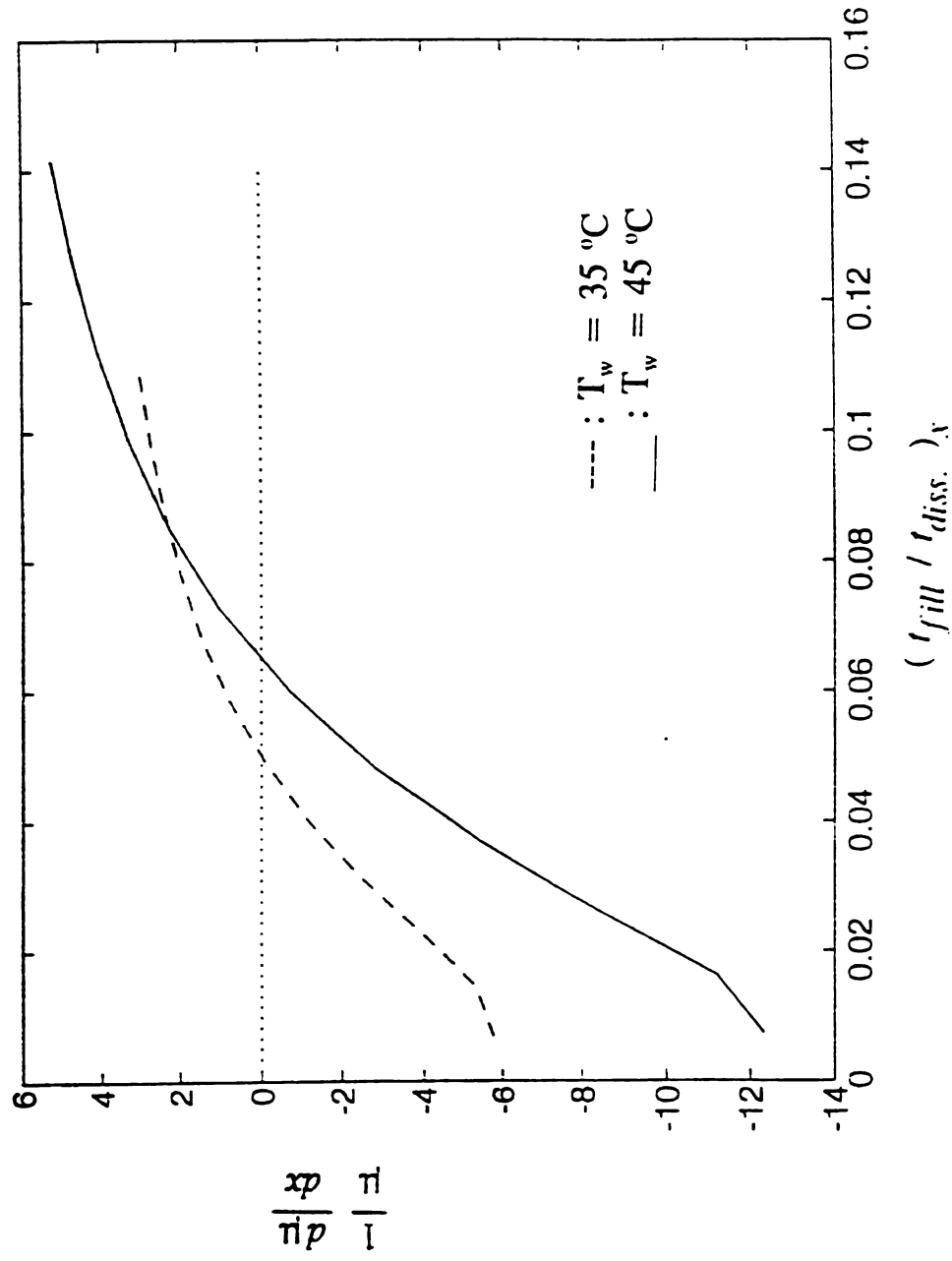


Figure 3.6: Variation of viscosity gradient with ratio of fill time to dissolution time

## ***Chapter 4 TRANSVERSE PERMEABILITY***

### **4.1 Permeability Prediction**

Permeability is one of the most important parameters in Darcy's law, a commonly used macroscale model for the mold filling process of liquid composite molding. Accurate permeability value is a critical requirement for the success of mold simulations based on Darcy's law. Permeability can be obtained through experimental measurements of the pressure drop versus the flow rate. However, these experiments are very time consuming due to the wide range of fiber volume fraction and the variety of fiber mats available. A model for permeability prediction provides a time efficient and cost effective means for permeability estimation, which is essential for any simulation models based on Darcy's law. It can greatly reduce the number of the experiments required to characterize the permeability of the preforms and further lead to a deeper understanding of the relationship between permeability and the preform architecture.

The permeation in regular arrays of aligned, unidirectional cylinders has been studied extensively with theoretical calculations, numerical analyses, and experimental measurements. For these regular arrays the principal directions of the permeability dyadic can be readily identified. Theoretical values of the transverse permeability have been tabulated for both square and hexagonal arrays by Sangani and

Acrivos [19]. Sangani and Yao [20] have later extended this calculation to the randomly packed arrays. Finite element analysis on both regular and random arrays has been performed by Berdichevsky and Cai [21-23]. Phelan [24] obtained the permeability for arrays of porous cylinder also using the finite element method. Results of FEA simulations on arrays of elliptic cylinders, both solid and porous, have been reported by Rangnathan and Advani [25]. Flow of generalized Newtonian fluid across periodic, unidirectional arrays of cylinders has been analyzed by Brushke and Advani [26].

Analytical expressions for the drag force on a cylinder in flow transverse to regular arrays of cylinders (square packed) at low porosity has been obtained first by Keller [27] using the lubrication approximation.

$$F = \frac{9\pi\mu U}{2\sqrt{2}} \left(1 - \frac{a}{l}\right)^{-\frac{5}{2}} \quad (4.1)$$

Here  $l$  is the pitch distance, and  $a$  is the radius of the cylinder (see Figure 4.1). Eq. (4.1) can be transformed in terms of permeability through [28]

$$F = \frac{\mu U \pi a^2}{K(1 - \phi)} \quad (4.2)$$

where  $\phi$  is the porosity and

$$\phi = 1 - V_f = 1 - \frac{\pi a^2}{4l^2} \quad (4.3)$$

here  $V_f$  is the fiber (cylinder) volume fraction. Hence the transverse permeability,  $K_z$  can be expressed in term of  $V_f$

where  $V_m$

$\pi/4$ . The

Chmielew

further d

measurem

correspon

For

developed

Be

expression

final form

here  $V_a$  is

the packing

In c

$$\frac{K_z}{a^2} = \frac{8\sqrt{2}}{9\pi} \left(1 - \frac{a}{l}\right)^{\frac{5}{2}} \left(\frac{a}{l}\right)^{-2} = \frac{8\sqrt{2}}{9\pi} \left(1 - \sqrt{\frac{V_f}{V_{fmax}}}\right)^{\frac{5}{2}} \left(\frac{V_f}{V_{fmax}}\right)^{-1} \quad (4.4)$$

where  $V_{fmax}$  is the maximum attainable  $V_f$  for square packed arrays, which equals 0.79 or  $\pi/4$ . The validity of these analytical results has been established by the experiments of Chmielewski et al [29] and Skartsis et al [30] on idealized cylinder arrays. Gebart [31] further discovered that the predicted permeability matches with the experimental measurements on unidirectional stitched fiber mats if an effective fiber radius corresponding to a small cluster of filaments is used.

For arrays of cylinders at higher porosity, a cell model with free surfaces has been developed by Happel [32]. The transverse permeability is predicted by the relation

$$\frac{K_z}{a^2} = \frac{1}{8V_f} \left[ \ln \frac{1}{V_f} - \frac{1 - V_f^2}{1 + V_f^2} \right] \quad (4.5)$$

Berdichevsky and Cai [22] have further improved this method to obtain analytical expressions for transverse permeability over the entire range of fiber volume fraction. The final formula derived from an improved self-consistent method is

$$K_z = 0.229 \left( \frac{1.814}{V_a} - 1 \right) \left[ \frac{(1 - \sqrt{V_f/V_a})}{(V_f/V_a)} \right]^{5/2} \quad (4.6)$$

here  $V_a$  is the maximum packing or available fiber volume fraction, which depends on the packing patterns of the unidirectional arrays.

In order to gain further insight into more complex structures, it is useful to

consider bi-  
of permeabi  
structures. V  
dimensional  
principal ax  
(components  
the unidirect

Ther  
[33 -35] and  
permeability  
A1118b). Th  
fraction rang  
obtained by

Kim et al [3  
They also p

Here A and  
variable in t  
types of bi-



consider bi-directional fiber mats, which serve as a key building block for the prediction of permeability of more complicated, three dimensional, woven, knitted or braided structures. Well aligned bi-directional fiber mats may be represented by periodic three dimensional arrays with two orthogonal sets of cylinders as shown in Figure 4.1. The principal axes of the permeability dyadic are along the axes of the two sets of cylinders (components  $K_x$  and  $K_y$ ) and along the thickness direction of the stack,  $K_z$ . Unlike for the unidirectional arrays, no analytical model has been reported for this kind of geometry.

There are however some limited experimental data reported by Lee and co-workers [33 -35] and Morse et al [36]. Lee and co-workers have done extensive measurements of permeability on various fiber mats including bi-directional stitched fiber mats (Cofab-A1118b). They reported both in-plane and transverse permeability data for fiber volume fraction ranging from 0.3 to 0.55. Empirical relations for permeability prediction were obtained by fitting the experimental data [34].

$$K_z = \frac{272(1 - V_f)^3}{V_f^2} \quad (4.7)$$

Kim et al [37] investigated the in-plane and the transverse permeation through 0/90 cloth. They also proposed an empirical relation from experimental measurements.

$$K = A(BV_{fmax} - V_f) \quad (4.8)$$

Here A and B are the fitting constants. Since the fiber volume fraction was the only variable in these relations, they cannot be used to estimate the permeability of different types of bi-directional fiber mats. As shown in the paper of Morse et al [35], the

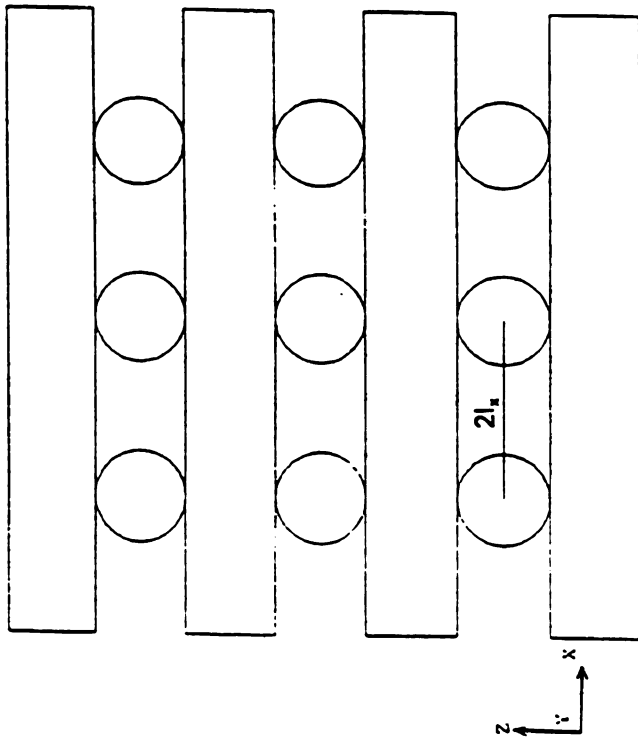


Figure 4.1: Fiber arrangement in an aligned stack of bi-directional fiber mats

difference between the transverse permeability of two different types of bi-directional fiber mats can be as large as 100% even at the same fiber volume fraction. Hence other structural parameters that affect the permeation should also be considered.

The effects of preform microstructure on the permeation through bi-directional stitched fiber mats have been studied by Kalyanaraman [38]. The main microstructural characteristics of preforms were identified as (i) the number of filaments per tow, (ii) the diameter of a single filament, (iii) the number of tows per inch in 0/90 directions, and (iv) the stitch or weave pattern. All these and the fiber volume fraction can affect the preform permeability, and should be taken into account in the models for permeability prediction. This chapter will focus on the prediction of the transverse permeability of bi-directional fiber mats. First 3-D flow simulations in idealized bi-directional fiber arrays are performed by using the finite element method (FIDAP). Then an analytical model for permeability prediction is developed with appropriate simplifications on the 3-D flow solutions. Finally, this model is tested by comparing with the experimental data obtained in our own lab [38].

## **4.2 Finite Element Analysis**

### **4.2.1 Numerical scheme**

For the idealized structure of bi-directional fiber mats shown in Figure 4.1, periodic repeat patterns or computational cells can be identified with appropriate boundary conditions. The computational cells for permeation transverse to the stack are depicted in Figure 4.2. As can be seen, the cell consists of an inlet surface,  $\Gamma_{in}$ , the cylinder surfaces,  $\Gamma_{cyl}$ , the symmetric surfaces,  $\Gamma_{sym}$ , and an outlet surface,  $\Gamma_{out}$ . Finite element simulations

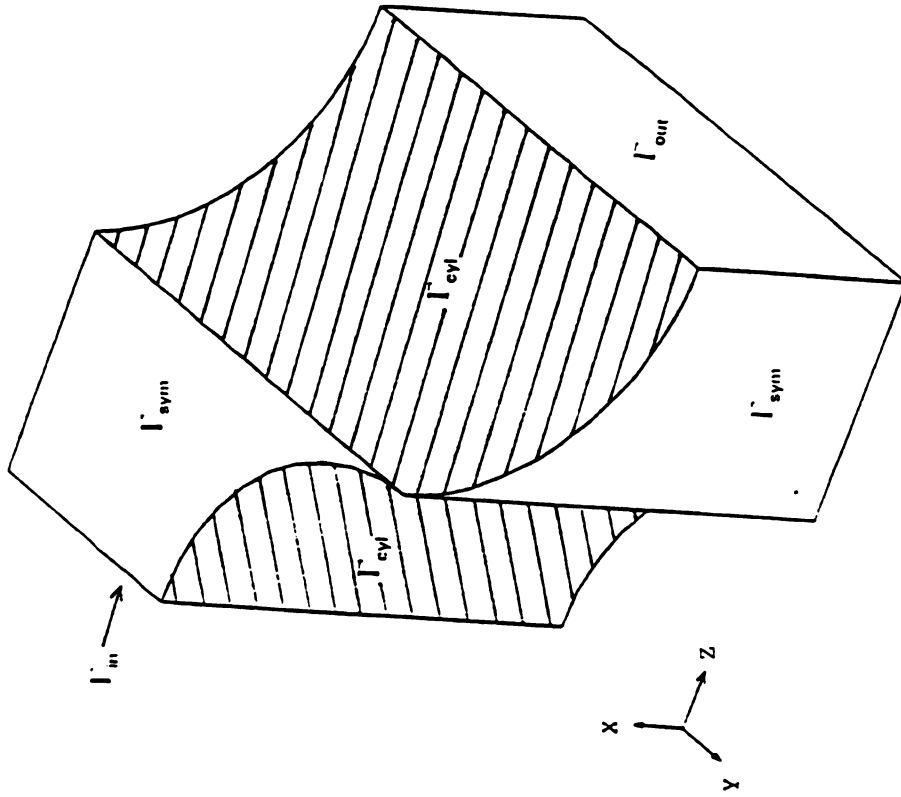


Figure 4.2: Computational cell for transverse permeation (z-direction)

of the flow of a Newtonian fluid through the repeat cell are performed with the help of FIDAP [1]. The Stokes solution of the interstitial velocity field are obtained by solving the following equations:

$$\nabla \cdot \vec{u} = 0 \quad (4.9)$$

$$\mu \nabla^2 \vec{u} = \nabla P \quad (4.10)$$

Here  $\vec{u}$  is the interstitial velocity. The corresponding boundary conditions are :

$$\begin{aligned} \vec{u} &= 0, & \text{on } \Gamma_{cyl} \\ u_n &= 0, & \text{on } \Gamma_{sym} \\ P(\Gamma_{in}) - P(\Gamma_{out}) &= -\Delta P \end{aligned} \quad (4.11)$$

where  $u_n$  is the velocity component in the normal direction of the symmetric surface. A constant pressure drop,  $(-\Delta P)$  is specified between the inlet and outlet surfaces.

A mesh of 4000 brick elements and 4851 nodes is used for the simulations as shown in Figure 4.3. In each brick element, the velocity is interpolated with trilinear shape functions,  $\phi_k$  of the form,

$$\phi_k = \frac{1}{8} (1 \pm r)(1 \pm s)(1 \pm t), \quad k = 1 \dots 8 \quad (4.12)$$

where  $r$ ,  $s$ , and  $t$  are normalized coordinates for the element, which vary from -1 to 1. The pressure is discretized piecewise in the element, where the interpolation function  $\psi_k$  is of the form,

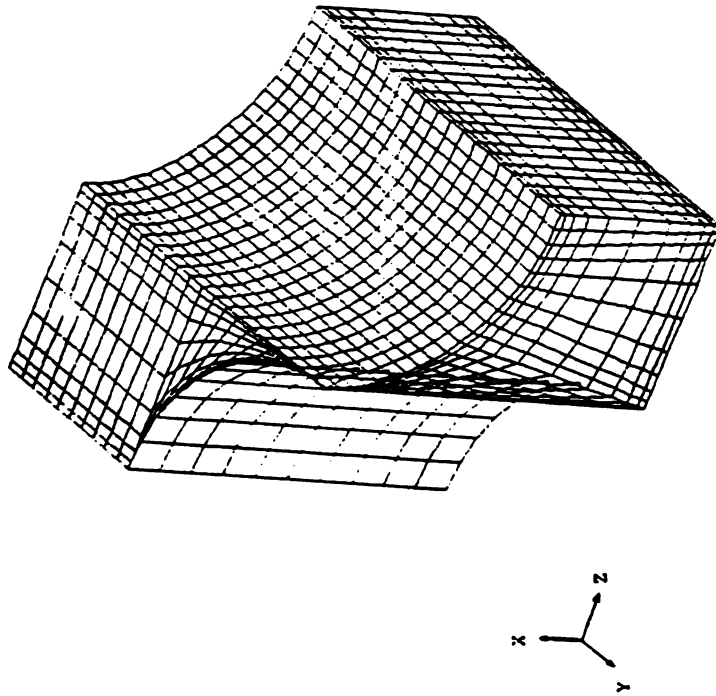


Figure 4.3: The 3-D mesh for transverse permeation

$$\begin{aligned}\psi_k &= 1 && \text{for } r, s, t \text{ within the element} \\ \psi_k &= 0 && \text{elsewhere}\end{aligned}\tag{4.13}$$

The running time of a typical case is around 5 hours on a SUN 690 MP at Case Center of Michigan State University.

#### 4.22 Numerical results

Numerical simulations are done for both symmetric and asymmetric pitch cases. For the symmetric pitch case, the pitches  $2l_x$  and  $2l_y$  are equal. For asymmetric pitch cases in this thesis, the ratio of  $(l_y-a)/(l_x-a)$  is set to 2 and 4, respectively. The Stokes flow field are solved for  $V_f$  ranging from 0.3 to 0.75. The velocity field is depicted in Figure 4.4 for  $V_f$  at 0.6042. As can be seen, the flow is locally parallel for each value of  $z$  as resin passes through the clearance of cylinders aligned in  $x$  and  $y$ -directions. Therefore the entire 3-D flow field can be decoupled into two regions of one-dimensional flow along the two filament (cylinder) directions. This pattern remains clear for  $V_f$  larger than 0.45. Furthermore from the corresponding pressure distribution (see Figure 4.5), one can see that most of the pressure drop occurs near the minimum gap clearance between the two cylinders, where the flow is essentially one-dimensional. Therefore the above simplification will not have significant effects on the calculation of the total pressure drop across the repeat unit cell.

Once the flow field is solved, the values of the permeability can be obtained from Darcy's law (Eq. (1.1)). All the permeability results are presented in dimensionless form, scaled by  $d^2$ , where  $d$  is the diameter of the cylinder. The transverse permeability for both symmetric and asymmetric pitch are compared in Figure 4.6. As can be seen,  $K_z$  for

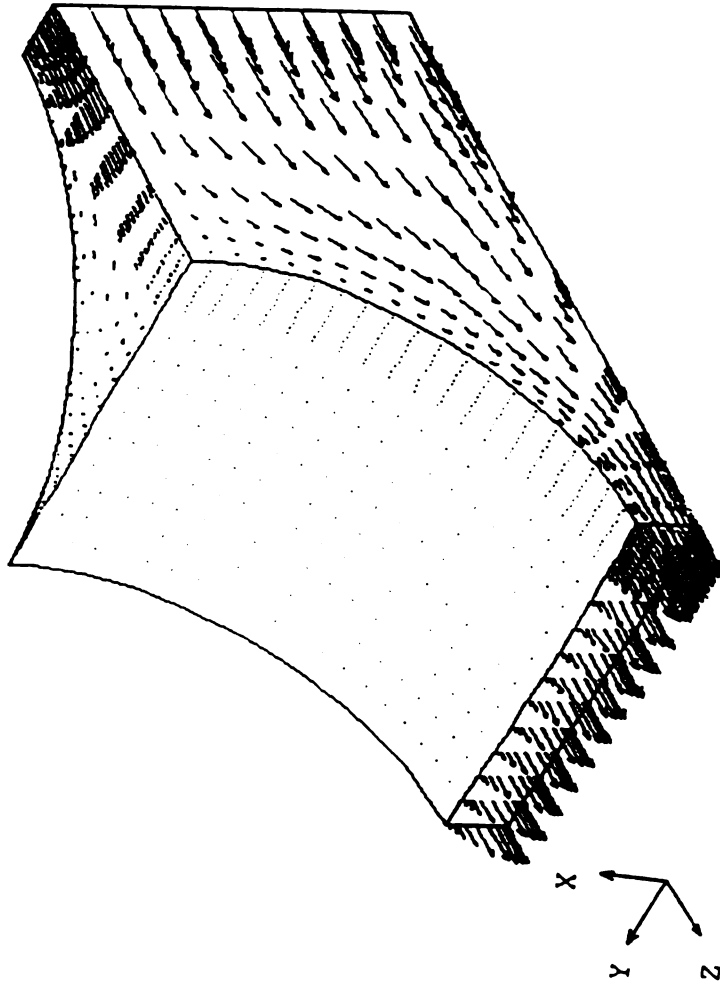


Figure 4.4: 3-D velocity field for transverse permeation



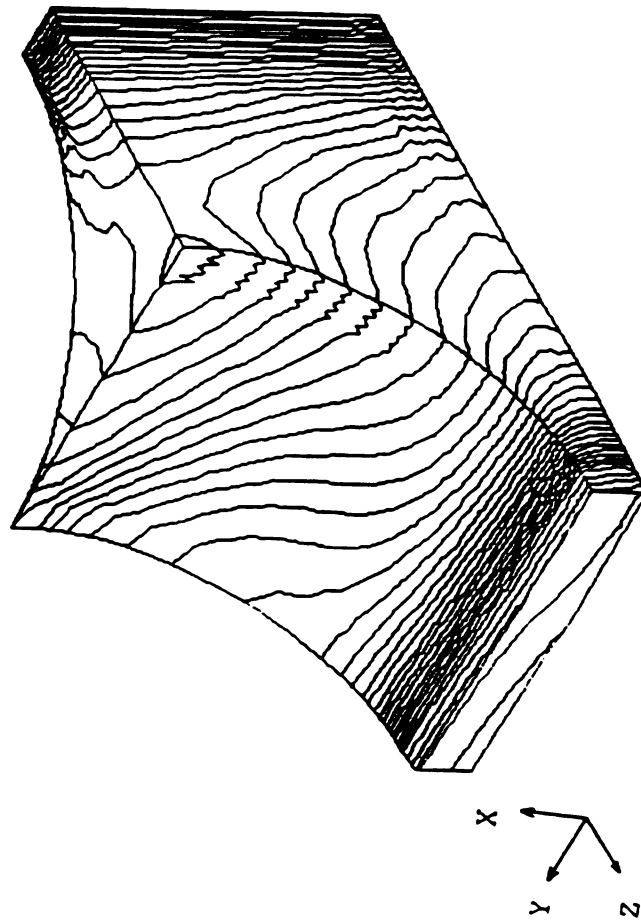


Figure 4.5: Pressure distribution for transverse permeation

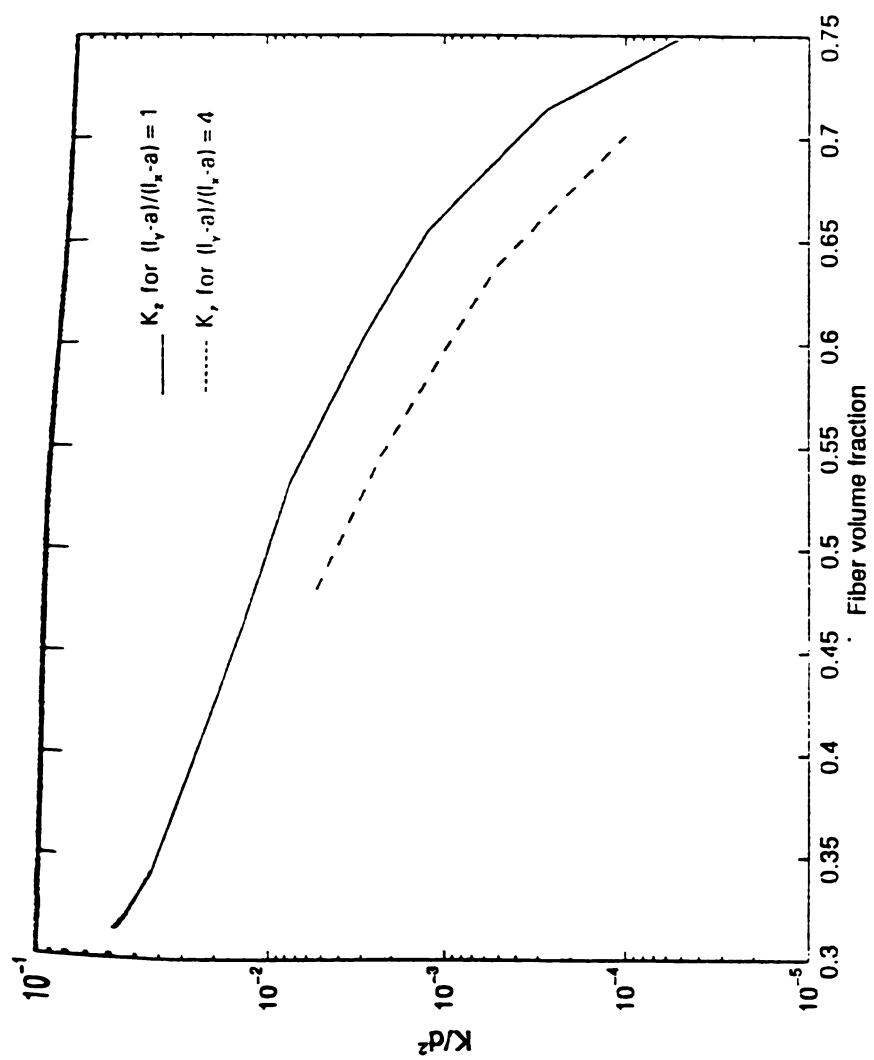


Figure 4.6: Numerical results of transverse permeability

asymmetric pitch is lower than  $K_z$  of symmetric pitch. For 0.50  $V_f$ , the transverse permeability of asymmetric pitch is 30% lower than  $K_z$  of symmetric pitch. The difference is larger at lower fiber volume fraction. At 0.50 fiber volume fraction,  $K_z$  for the asymmetric case is 60% less than  $K_z$  of symmetric pitch.

### 4.3 Transverse Permeability Model

#### 4.31 Structure parameters

As shown in Figure 4.7,  $V_f$  of bi-directional fiber arrays can be calculated from

$$V_f = \frac{\pi (a_x^2 l_x + a_y^2 l_y)}{4 l_x l_y (a_x + a_y)} \quad (4.14)$$

where  $a_x$  and  $a_y$  are radius of the cylinder aligned in x or y-direction. For maximum packing, ( $l_x = a_y$ , and  $l_y = a_x$ )

$$V_{fmax} = \frac{\pi}{4} \quad (4.15)$$

As shown in the next section, the transverse permeability of bi-directional fiber arrays can be determined by the following group of structural parameters:  $a_x$ ,  $V_f/V_{fmax}$ ,  $l_x/l_y$ , and  $a_y/a_x$ .

#### 4.32 Decoupling of the 3-D flow field

As indicated by the numerical results, the 3-D transverse flow field can be decoupled into two regions of one-dimensional flow mathematically. At high  $V_f$ , Eq. (4.10) can be broken into the following two equations for 1-D flow in x-z and y-z planes using the lubrication approximation (see Figure 4.7).

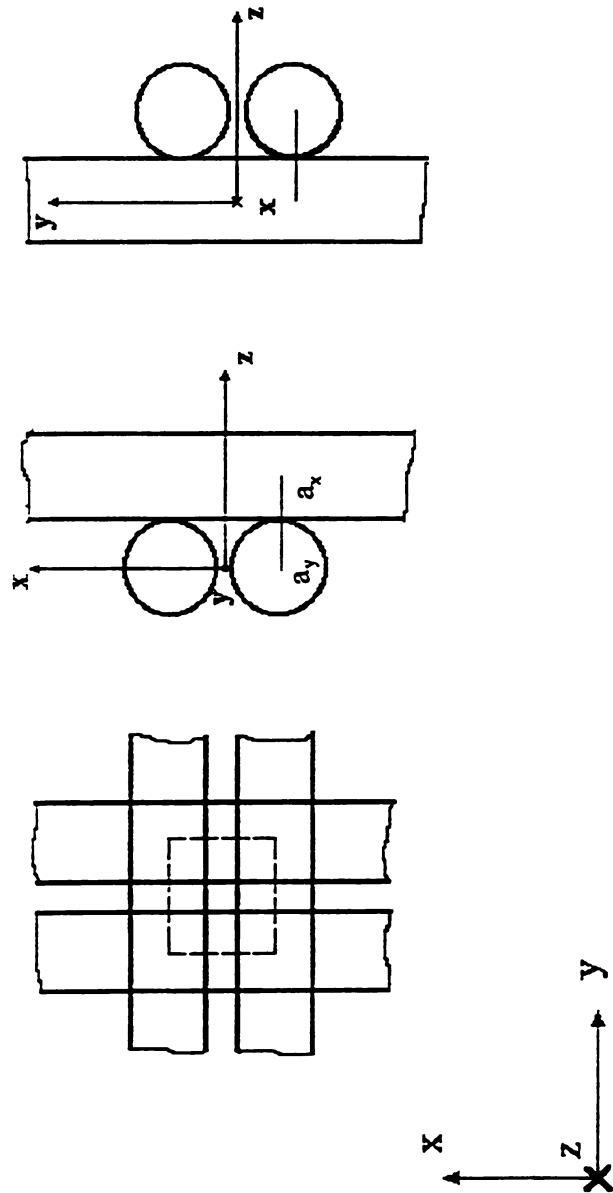


Figure 4.7: Three-dimensional repeat unit for transverse flow (z-direction)

$$\begin{aligned} \mu \frac{\partial^2 u_z}{\partial x^2} &= \frac{dP}{dz} \quad \text{for } -a_y < z < a_y \\ \mu \frac{\partial^2 u_z}{\partial y^2} &= \frac{dP}{dz} \quad \text{for } a_y < z < a_y + 2a_x \end{aligned} \quad (4.16)$$

Here  $u_z$  is the z-component of interstitial velocity. Eq. (4.16) can be easily solved to obtain  $u_z$

$$\begin{aligned} u_z(x) &= \frac{1}{2\mu} \frac{dP}{dz} (x^2 - h_{z1}^2) \quad \text{for } -a_y < z < a_y \\ u_z(y) &= \frac{1}{2\mu} \frac{dP}{dz} (y^2 - h_{z2}^2) \quad \text{for } a_y < z < a_y + 2a_x \end{aligned} \quad (4.17)$$

Here  $h_{z1}$  and  $h_{z2}$  are half of the gaps clearance, which vary with  $z$ .

$$\begin{aligned} h_{z1} &= l_x - (a_y^2 - z^2)^{\frac{1}{2}} \\ h_{z2} &= l_y - [a_x^2 - (z - a_x - a_y)^2]^{\frac{1}{2}} \end{aligned} \quad (4.18)$$

Upon integrating Eqs. (4.17), one can obtain two components of the pressure drop

$$\begin{aligned} \Delta P_1 &\doteq - \frac{9\pi (Q/2l_y) \mu a_y^{1/2}}{8\sqrt{2} (l_x - a_y)^{5/2}} \quad \text{for } -a_y < z < a_y \\ \Delta P_2 &\doteq - \frac{9\pi (Q/2l_x) \mu a_x^{1/2}}{8\sqrt{2} (l_y - a_x)^{5/2}} \quad \text{for } a_y < z < a_y + 2a_x \end{aligned} \quad (4.19)$$

where  $Q$  is the volumetric flow rate

$$Q = \int_{-l_y}^{l_y} \int_{-h_{z1}}^{h_{z1}} u_z(x) dx dy = \int_{-l_x}^{l_x} \int_{-h_{z2}}^{h_{z2}} u_z(y) dy dx \quad (4.20)$$

Hence the total pressure drop along one repeat cell becomes

$$-\Delta P = -(\Delta P_1 + \Delta P_2) = \frac{9\pi \mu U_z}{8\sqrt{2}} \left[ \frac{2l_x a_y^{1/2}}{(l_x - a_y)^{5/2}} + \frac{2l_y a_x^{1/2}}{(l_y - a_x)^{5/2}} \right] \quad (4.21)$$

where  $U_z$  is the superficial velocity,

$$U_z = \frac{Q}{(2l_x \cdot 2l_y)} \quad (4.22)$$

Hence the transverse permeability,  $K_z$  can be calculated from Darcy's law:

$$K_z = -\frac{\mu U_z 2(a_x + a_y)}{\Delta P} = \frac{8\sqrt{2}(a_x + a_y)}{9\pi} \left[ \frac{l_x a_y^{1/2}}{(l_x - a_y)^{5/2}} + \frac{l_y a_x^{1/2}}{(l_y - a_x)^{5/2}} \right]^{-1} \quad (4.23)$$

Using Eqs. (4.14) and (4.15), one obtains

$$\frac{K_z}{a_x^2} = \frac{8\sqrt{2}(1+\beta)}{9\pi} \left[ \frac{\left( \frac{V_f}{V_{fmax}} \cdot \frac{\beta^2 + \beta}{\beta^2 + \alpha} \right)^{3/2}}{\beta \left( 1 - \frac{V_f}{V_{fmax}} \cdot \frac{\beta^2 + \beta}{\beta^2 + \alpha} \right)^{5/2}} + \frac{\left( \frac{V_f}{V_{fmax}} \cdot \frac{\alpha + \alpha \beta}{\beta^2 + \alpha} \right)^{3/2}}{\left( 1 - \frac{V_f}{V_{fmax}} \cdot \frac{\alpha + \alpha \beta}{\beta^2 + \alpha} \right)^{5/2}} \right]^{-1} \quad (4.24)$$

where

$$\alpha = \frac{l_x}{l_y} \text{ and } \beta = \frac{a_y}{a_x} \quad (4.25)$$

Hence one can determine the transverse permeability by knowing  $a_x$ ,  $V_f/V_{fmax}$ ,  $l_x/l_y$ , and

$a_y/a_x$ .

If the radius of the cylinders are the same ( $a_x=a_y=a$  ,  $\beta=1$ )

$$\frac{K_z}{a^2} = \frac{16\sqrt{2}}{9\pi} \left[ \frac{\left(\frac{V_f}{V_{fmax}} \cdot \frac{2}{1+\alpha}\right)^{3/2}}{\left(1 - \frac{V_f}{V_{fmax}} \cdot \frac{2}{1+\alpha}\right)^{5/2}} + \frac{\left(\frac{V_f}{V_{fmax}} \cdot \frac{2\alpha}{1+\alpha}\right)^{3/2}}{\left(1 - \frac{V_f}{V_{fmax}} \cdot \frac{2\alpha}{1+\alpha}\right)^{5/2}} \right]^{-1} \quad (4.26)$$

Further for symmetric pitch ( $l_x = l_y = l$ ,  $\alpha = 1$  ),

$$\frac{K_z}{a^2} = \frac{8\sqrt{2}}{9\pi} \left(1 - \frac{V_f}{V_{fmax}}\right)^{5/2} \left(\frac{V_f}{V_{fmax}}\right)^{-3/2} \quad (4.27)$$

This expression is very similar to that of unidirectional arrays ( square packed ) as shown by rearranging Eq. (4.4)

$$\frac{K_z}{a^2} = \frac{8\sqrt{2}}{9\pi} \left(1 - \sqrt{\frac{V_f}{V_{fmax}}}\right)^{5/2} \left(\sqrt{\frac{V_f}{V_{fmax}}}\right)^{-1} \quad (4.28)$$

### 4.33 Model predictions and comparisons with numerical results

The transverse permeability predictions for the symmetric pitch case are plotted in Figure 4.8 against  $V_f$  with the computed results from FEA analysis. The analytical solutions match well with the numerical results for fiber volume fraction greater than 0.55 (<10%). The difference between the two increases at lower  $V_f$ . This trend is expected since the decoupling of the 3-D flow is only valid at high fiber volume fractions. Hence the analytical solutions of transverse permeability provide a check on the computed results from the numerical simulation. The comparison of model predictions and numerical results

for the asymmetric cases are plotted in Figures 4.9 and 4.10. The same trend is observed.

A modified model is obtained by changing the power index  $3/2$  in Eq. (4.26) to  $3/4$  in order to match the numerical results at lower  $V_f$ .

$$\frac{K_z}{a^2} = \frac{16\sqrt{2}}{9\pi} \left[ \frac{\left(\frac{V_f}{V_{fmax}} \cdot \frac{2}{1+\alpha}\right)^{3/4}}{\left(1 - \frac{V_f}{V_{fmax}} \cdot \frac{2}{1+\alpha}\right)^{5/2}} + \frac{\left(\frac{V_f}{V_{fmax}} \cdot \frac{2\alpha}{1+\alpha}\right)^{3/4}}{\left(1 - \frac{V_f}{V_{fmax}} \cdot \frac{2\alpha}{1+\alpha}\right)^{5/2}} \right]^{-1} \quad (4.29)$$

The predictions obtained from this modified model are shown in Figure 4.11 with the numerical results for the symmetric pitch case. As can be seen, the model prediction agrees well with the FEA results for the entire range of fiber volume fraction. The comparison for an asymmetric case is plotted in Figure 4.12. The same trend is observed.

The transverse permeability of bi-directional fiber arrays (symmetric pitch) is compared with that of unidirectional arrays (square packing) in Figure 4.13. At the same fiber volume fraction bi-directional arrays have higher transverse permeability than unidirectional arrays. This result is reasonable since for bi-directional arrays

$$\frac{a}{l} = \frac{V_f}{V_{fmax}} \quad (4.30)$$

And for the square packed unidirectional arrays, one has

$$\frac{a}{l} = \sqrt{\frac{V_f}{V_{fmax}}} \quad (4.31)$$

Hence for the same  $V_f$ , the gap is larger for bi-directional arrays than for unidirectional arrays. Thus the transverse permeability of bi-directional arrays is higher. Note the maximum attainable fiber volume fraction is  $\pi/4$  for both cases. As  $V_f$  approaches to its



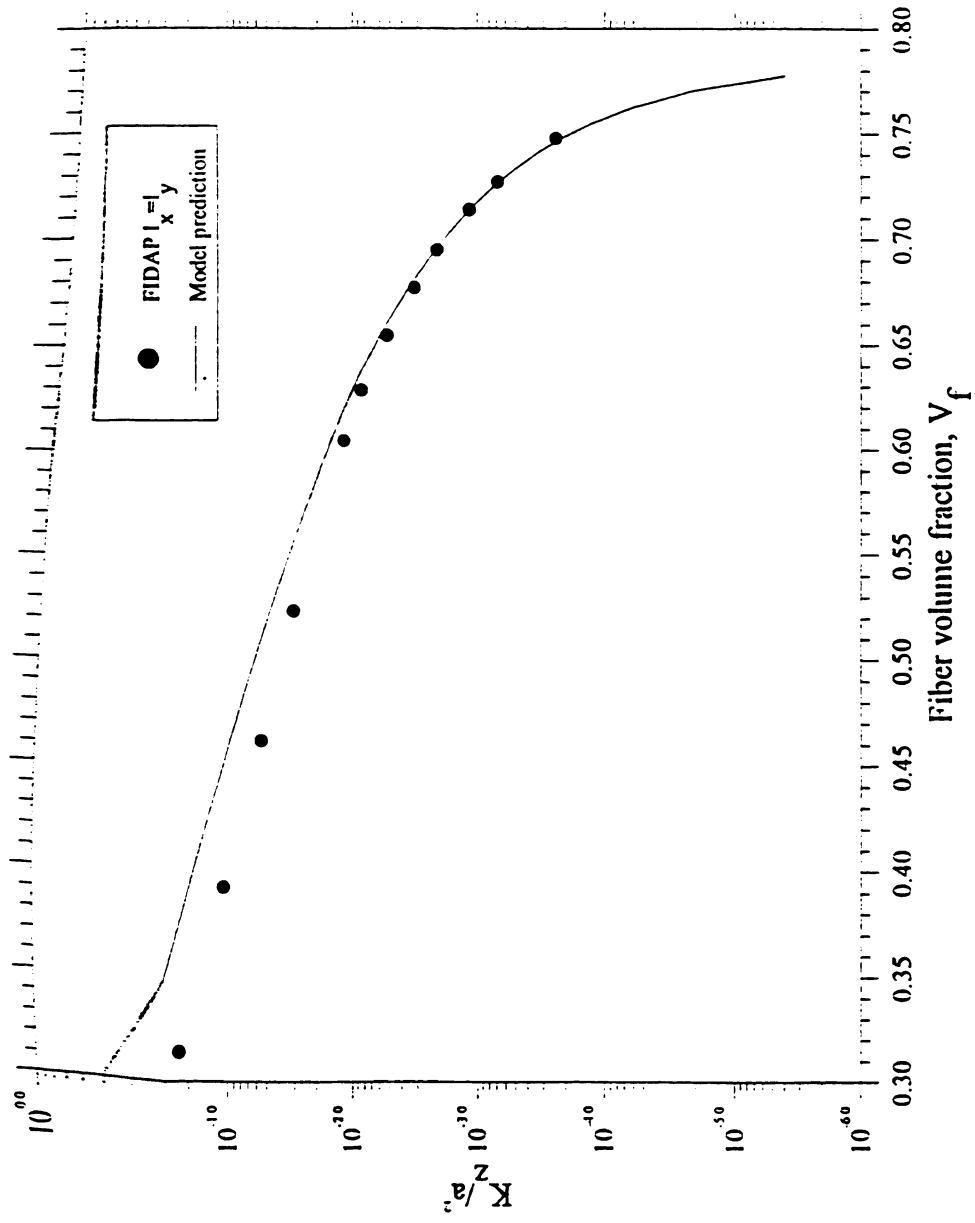


Figure 4.8: Comparison between numerical results and Eq. (4.26),  $l_x=l_y$

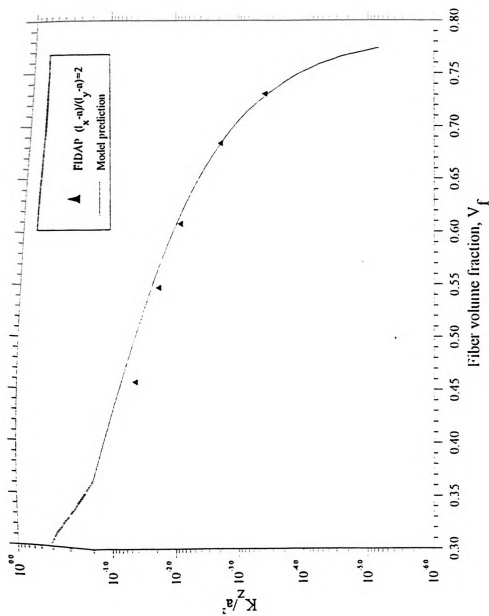


Figure 4.9: Comparison between numerical results and Eq. (4.26),  $I_x \neq I_y$ .

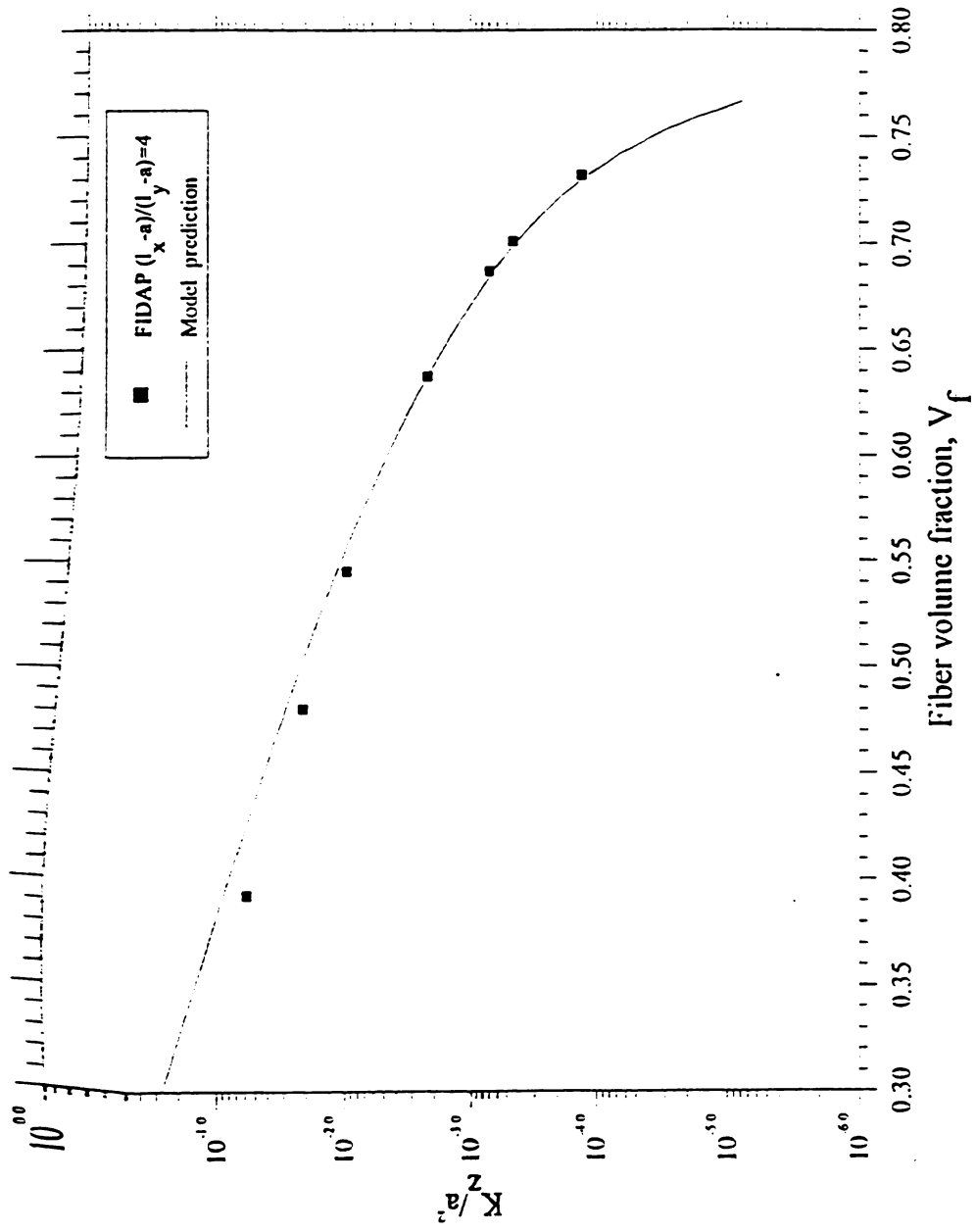


Figure 4.10: Comparison between numerical results and Eq. (4.26),  $l_x \neq l_y$

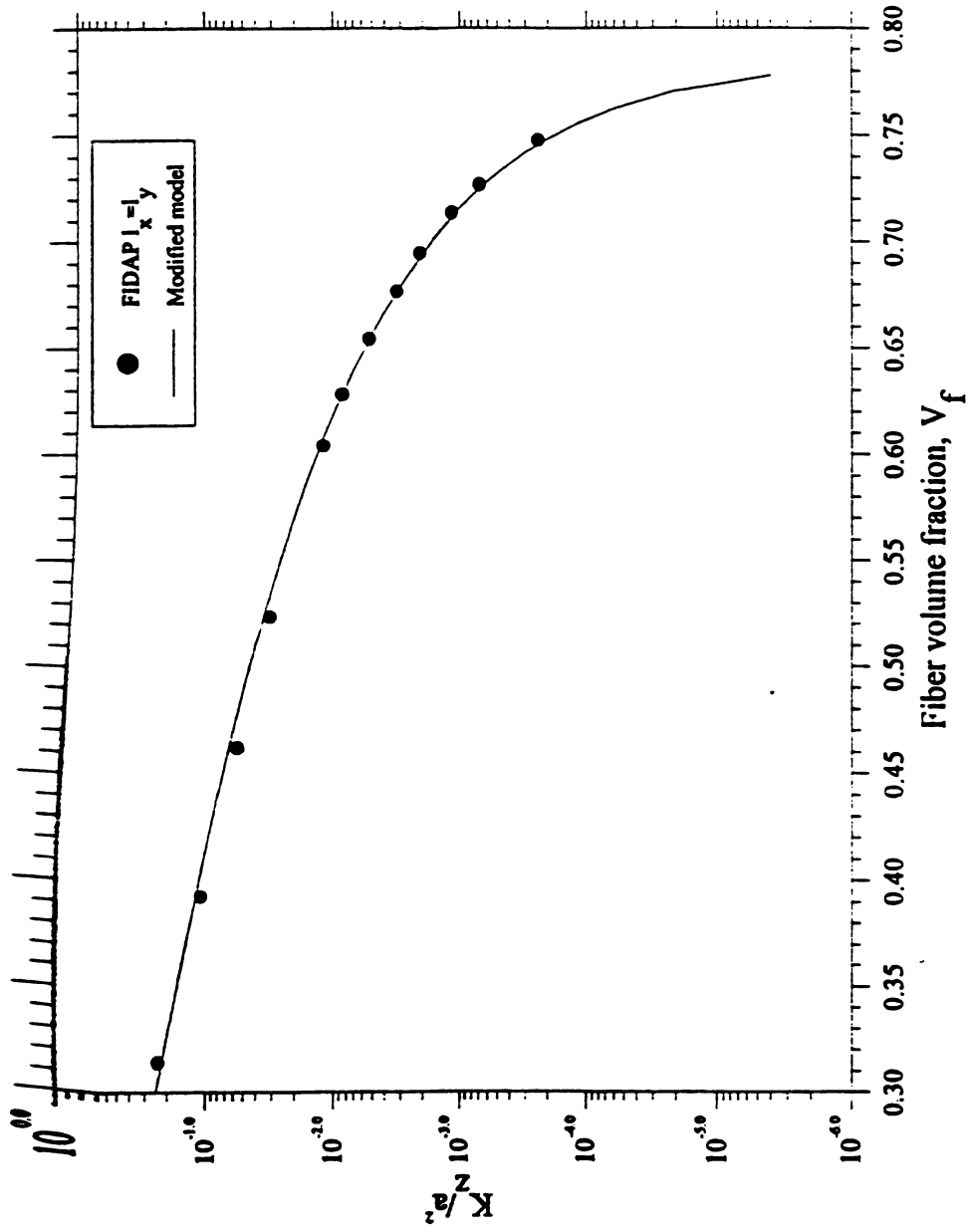


Figure 4.11: Comparison between numerical results and Eq. (4.29),  $l_x=l_y$

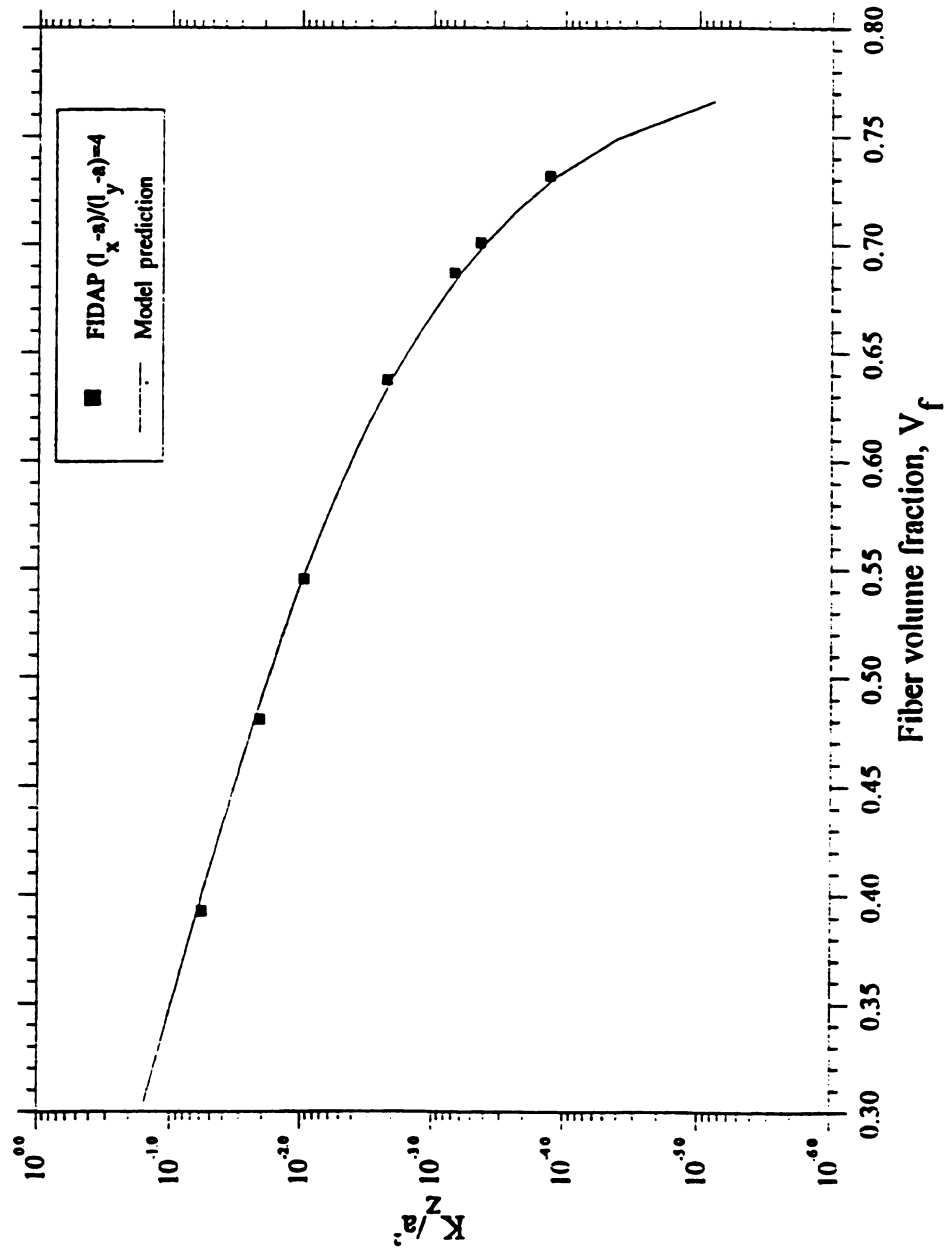


Figure 4.12: Comparison between numerical results and Eq. (4.29),  $l_x \neq l_y$

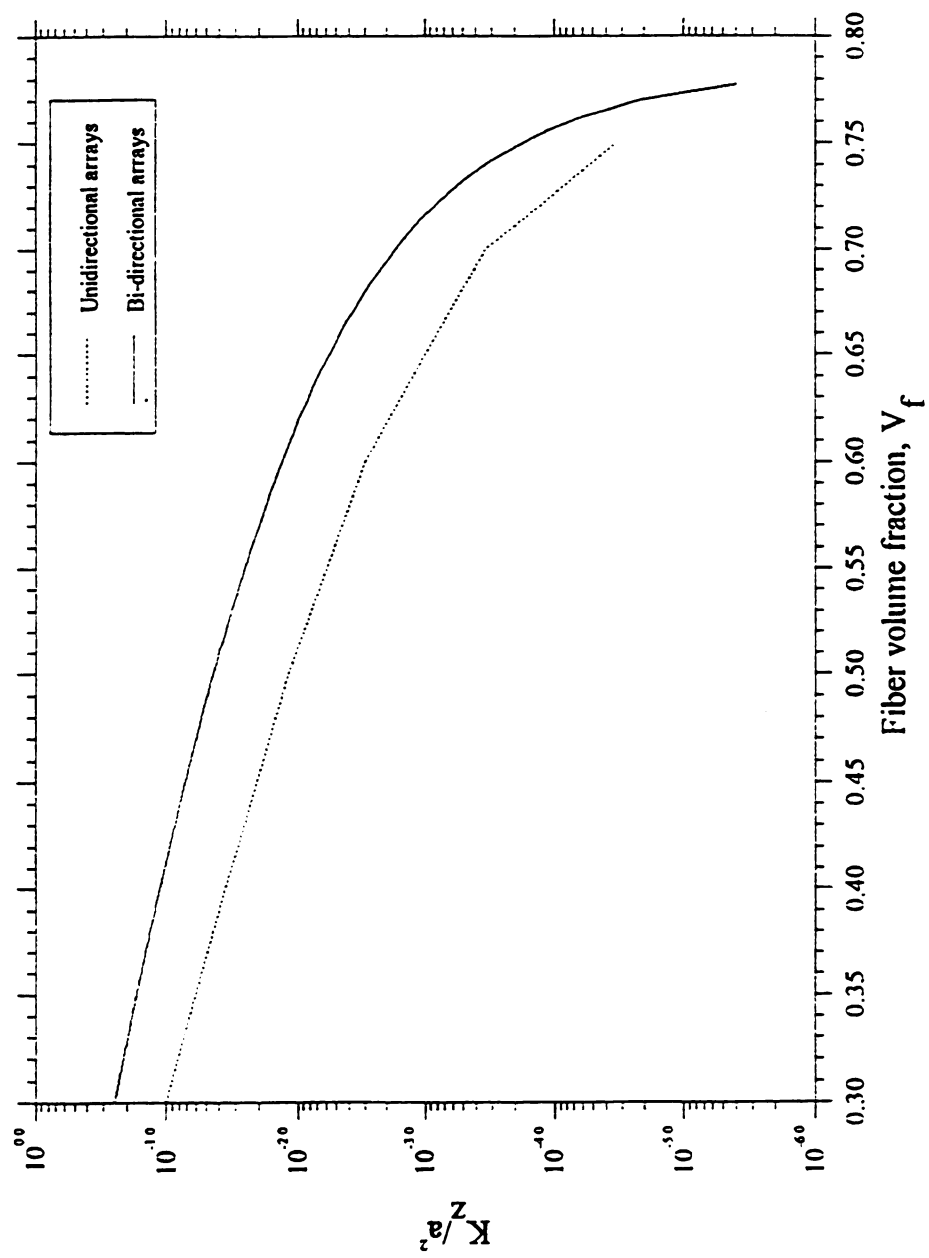


Figure 4.13: Transverse permeability for bi-directional and unidirectional arrays

maximum value, transverse permeability in both cases goes to zero. However the decay rate of the transverse permeability for bi-directional arrays is faster.

Finally the effects of pitch ratio,  $l_x/l_y$  is investigated in Figure 4.14, which shows the variation of transverse permeability with  $l_x/l_y$  for several different fiber volume fractions. The model shows that the transverse permeability is lowered significantly as the pitches along the two cylinder axes are made asymmetric. This trend is also observed in the FEA results (see Figure 4.6).

#### 4.4 Experimental Validation

The theoretical and numerical results of permeability presented in previous sections are obtained for a perfectly aligned stack of bi-directional fiber arrays. However, the real structure of the bi-directional stitched fiber mats is different from this idealized structure. In bi-directional fiber mats, the filaments are grouped in fiber tows, which are porous and generally do not have a circular cross section. Compressed inside the mold, the fiber tows are usually in elliptic shape. Hence the validity of the prediction model based on idealized bi-directional cylinder arrays needs to be tested.

##### 4.4.1 Experimental

Measurements of in-plane as well as transverse permeability of bi-directional stitched fiber mats have been carried out in our own lab [38]. Three type of bi-directional mats were used, two of which were assembled from unidirectional plies by stacking them in the 0/90 arrangements. The third one is a bi-directional stitched fiber mats. The specification of these materials are listed in the table below.

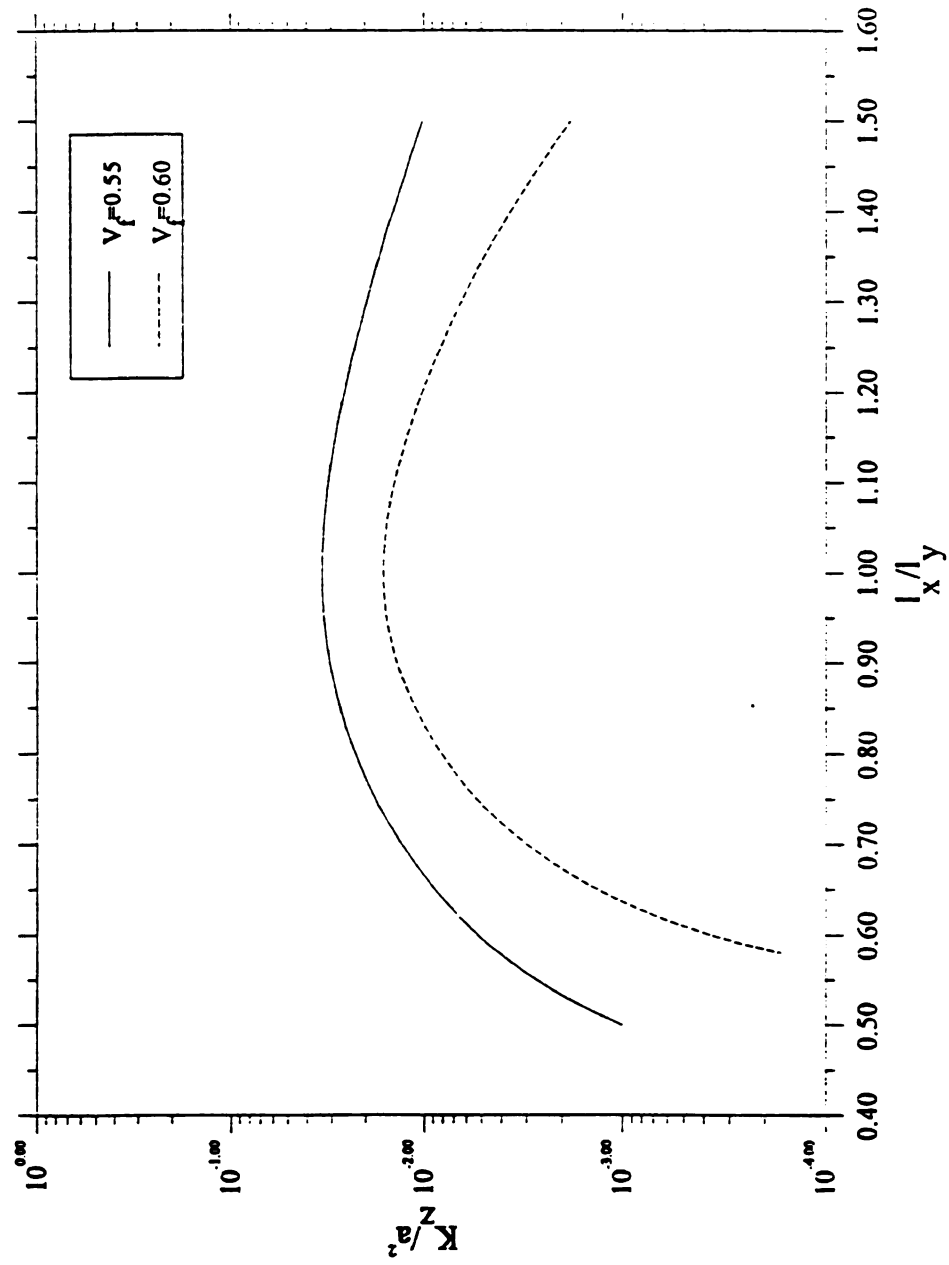


Figure 4.14: Predicted transverse permeability verse ratio of pitch distances





**Table 4.1 Specifications of bi-directional fiber mats**

Mats	Cross-plyed UA8	Cross-plyed UB6	Cofab
Tow weight	450 yards/lb	225 yards/lb	
Tows/inch	13.72	9.5	6.5
Filaments/tow	1600	3200	2000
Filament diameter	19 microns	19 microns	15.5 microns

The impregnation fluids was a mixture of glycerol and water, with a viscosity range from 66 mPa-s to 230 Pa-s at room temperature. Dow Corning's Silicone sealant and vacuum grease were used to provide effective sealing. Compressed nitrogen was used to force the liquid through the permeation cells. The fiber preform is cut from a large roll of fiber mats, and the stacked preform is then transferred to the Wabash instrumental press to be compressed. The details of the flow loop set-up, the preforming technique, as well as the permeation cells assemblies for in-plane and transverse permeability measurements can be found in [38].

#### **4.42 Comparisons with experimental data**

The results of the transverse permeability measurements for bi-directional fiber mats consisting of cross plyed UA8 and UB6 mats are shown in Figure 4.15 with the model predictions (Eq.(4.19)). As can be seen, the model prediction matches fairly well

with the experimental data for fiber volume fraction ranging from 0.45 to 0.65. The comparison of the analytical solution with the experimental data obtained for the Cofab mats is plotted in Figure 4.16. Same trend is observed. Since for both cases the pitch is symmetric, Eq. (4.27) is used to generate analytical results. The parameter  $a$  in Eq. (4.27) is set to be the radius of the single filament, which are 9.5 microns for cross-plyed mats and 7.75 microns for the Cofab stitched mats.

The choice of using the radius of a single filament can be explained by the microstructure of the bi-directional fiber mats. Before being placed into the mold, the fiber mats were consolidated in order to attain high fiber volume fraction. In the compressed fiber mats, the fiber tows are flattened and the large pore channels between the tows are eliminated. This has been confirmed by the micrographs obtained from Scanning Electron Microscopy [38]. Since fiber tows become indistinguishable as the preforms are compressed, the flow through the preform network take place only in gaps between the filaments. Therefore the suitable length scale in the permeability model should be the radius of the single filament rather than the radius of the whole fiber tow.

The permeability values of the Cofab is lower than that of the cross-plyed UA8 and UB6 since Cofab mats have lower filament radius which leads to smaller gaps between them. Furthermore the predicted permeability values are slightly lower than the experimental measurements at  $V_f$  below 0.55. This is because at lower fiber volume fraction, the fiber tows are not completely flattened. The gaps between the fiber tows are greater than the average pore size between the individual filaments. Hence more flow occurs through the preform than predicted by the model, resulting in higher permeability.

The experimental data are compared with the some of the existing permeability

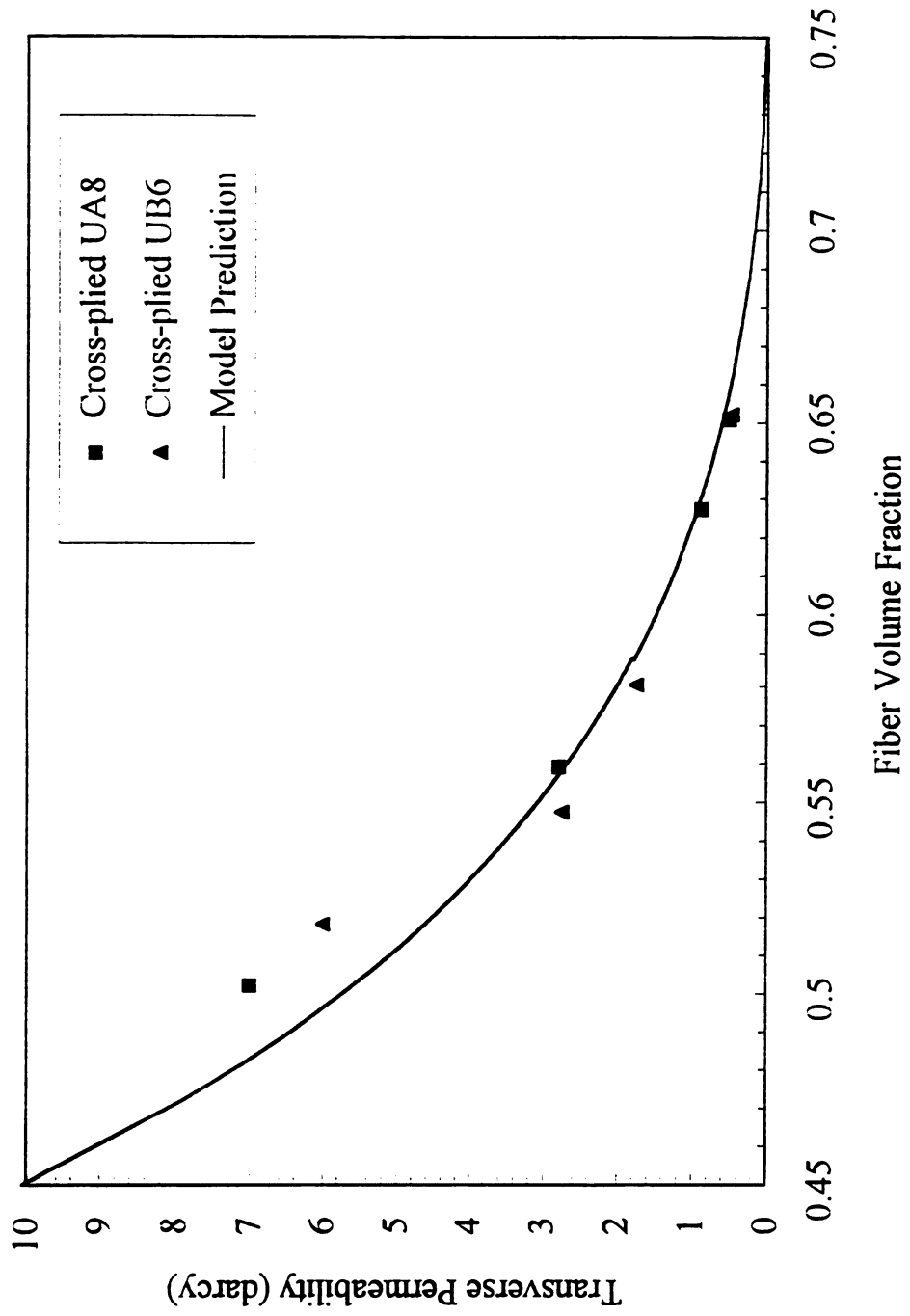


Figure 4.15: Comparison of model prediction and experimental data (cross-plyed)

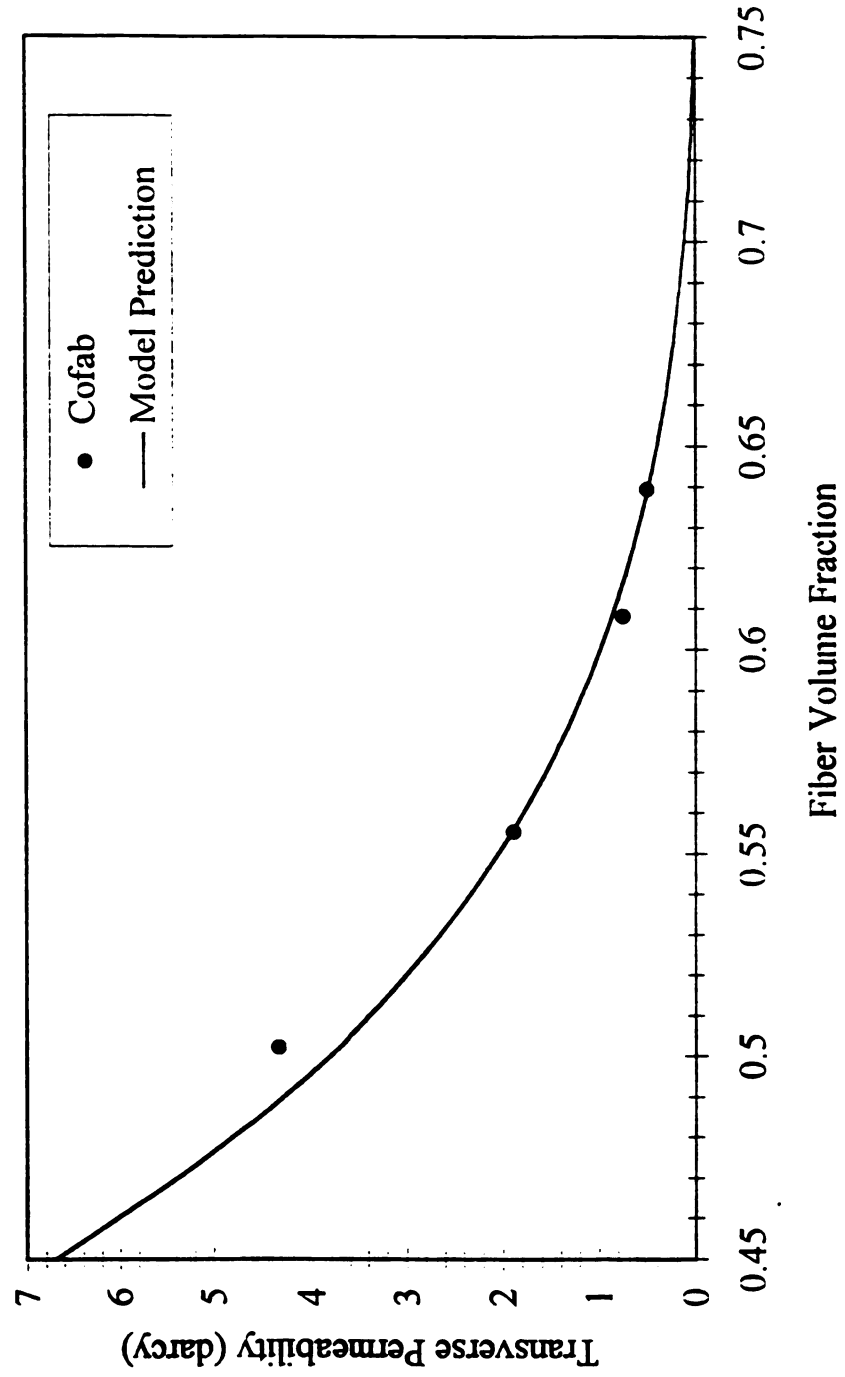


Figure 4.16: Comparison of model prediction and experimental data (Cofab)

models as shown in Figure 4.17. The empirical constants in these models are determined by best fitting the experimental data. As can be seen, none of these models can provide a close match with the experimental data. The success of the proposed model is not surprising since this model is specific to preforms with bi-directional architecture, and thus taken into account the preform geometry without lumping the them into model parameters which may vary for different type of fiber mats. In addition to preform geometry, the model also includes the effect of the preform microstructure, which is through the filament radius, a relevant unit in the compressed preforms.

Finally, the model is used to predict the transverse permeability of bi-directional mats with asymmetric pitch. The experimental data for bi-directional mats with asymmetric pitch are reported by Morse et al [36]. The model prediction and the experimental data are shown in Table 4.2. The fiber volume fraction is 0.37 for both mats. The ratio of the pitch distance,  $\alpha$  is calculated from the ration of the tow ends in 0/90 directions.

**Table 4.2 Transverse permeability for asymmetric pitched  
bi-directional fiber mats**

	$\alpha (l_x/l_y)$	$K_z$ experimental	$K_z$ model
Mat 1	3.48	16 darcy	11 darcy
Mat 2	1.61	32 darcy	32 darcy

One can see from Table 4.2 that the trends predicted by the model is supported by the

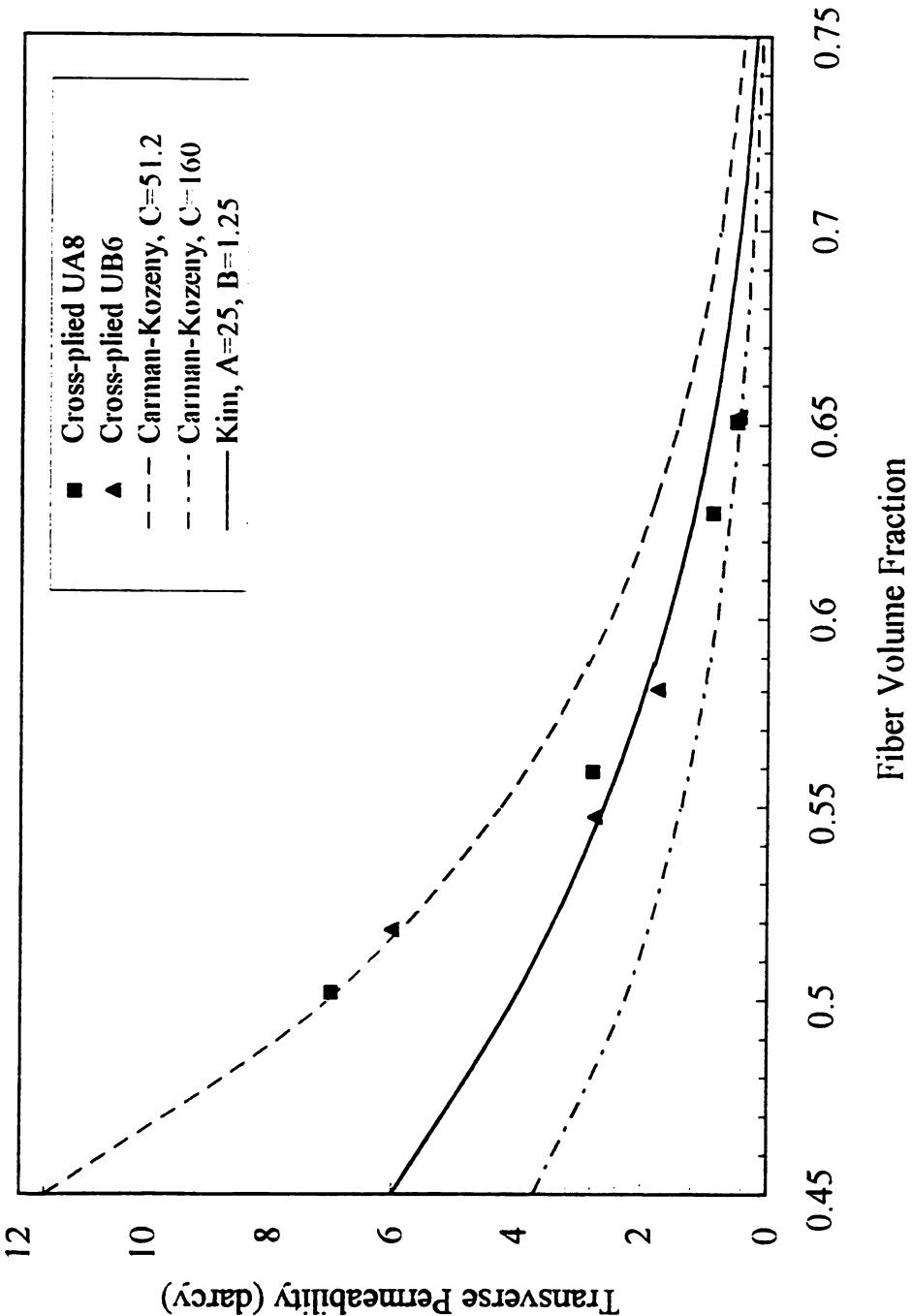


Figure 4.17: Companion between existing models and the experimental data

experimental data. However due to the flattening of the fiber tow in compressed preform, the definition of pitch distance is not as clear as that of the idealized regular arrays. More work has to be done so that proper structure parameters can be included in the model.

In conclusion, an analytical model based on the lubrication approximation is developed to predict the transverse permeability of bi-directional fiber mats. The model prediction is first confirmed by the numerical results at high  $V_f$ . Furthermore the transverse permeability predictions match well with the experimental measurements on bi-directional fiber mats when the filament radius is used as the length scale. The usage of the filament radius rather than the fiber tow radius is supported by the study of the microstructure of the compressed fiber preforms. Hence the analytical model developed for the transverse permeability is valid for the real fiber preforms.



## ***Chapter 5 IN-PLANE PERMEABILITY***

### **5.1 In-plane Permeability Prediction**

As for the transverse permeability, the longitudinal permeability of unidirectional fiber arrays has also been studied by many researchers. The theoretical values of this quantity for square and hexagonal packed unidirectional arrays are obtained by Drummond and Tahir [39]. An analytical solution for the longitudinal permeability at low fiber volume fraction was obtained by Happel [32].

$$\frac{K_x}{a^2} = \frac{1}{8 V_f} \left( 4 V_f - V_f^2 - 3 + 2 \ln \frac{1}{V_f} \right) \quad (5.1)$$

Berdichevsky and Cai [22,23] have later obtained an improved analytical expressions by using the improved self-consistent method (see Eq. (5.2)). This expression is also valid at high  $V_f$ .

$$K_x = 0.211 (V_a - 0.605) \left( 0.907 \frac{V_f}{V_a} \right)^{-1.81} \left( 1 - 0.907 \frac{V_f}{V_a} \right) + 0.292 (0.907 - V_a) (V_f)^{-1.57} (1 - V_f)^{1.55} \quad (5.2)$$

For bi-directional fiber mats, Lee and co-workers [34, 40] proposed the following empirical relation by fitting the experimental data.

$$\begin{aligned}
K_x &= 47 e^{5.92(1-V_f)} + [2018(1 - V_f) - 592] u \\
K_y &= \frac{4}{5} K_x
\end{aligned}
\tag{5.3}$$

This empirical relation is only valid for the type of fiber mats used in their experiments.

In the following sections, an analytical expression is proposed for in-plane permeability of bi-directional fiber mats. The model is developed based on the simplifications of the 3-D flow through the idealized structure (see Figure 4.1). The model prediction is compared with the experimental data obtained in our own lab [38].

## 5.2 Finite Element Analysis

### 5.21 Numerical scheme

The FEA analysis of the in-plane permeation is also carried out on repeat cells with appropriate boundary conditions as for the transverse permeation. The computational cells for in-plane permeation is depicted in Figure 5.1. In this case, periodic velocity boundary conditions are applied at the inlet and outlet surfaces. Eqs. (4.9) and (4.10) are solved with the boundary conditions listed below.

$$\begin{aligned}
\vec{u} &= 0, & \text{on } \Gamma_{cyl} \\
u_n &= 0, & \text{on } \Gamma_{sym} \\
\vec{u}(\Gamma_{in}) &= \vec{u}(\Gamma_{out}) \\
P(\Gamma_{in}) - P(\Gamma_{out}) &= -\Delta P
\end{aligned}
\tag{5.4}$$

As shown in Figure 5.2, a mesh of 8000 brick elements and 9451 nodes is used to perform numerical simulations using FIDAP. The running time of a typical case is

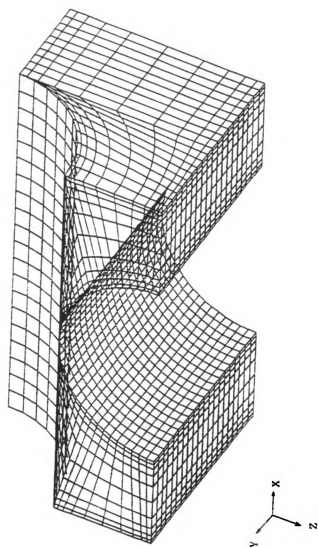


Figure 5.2. The 3-D mesh for in-plane permeation

around 15 hours on the SUN 690 MP.

## 5.22 Numerical results

The Stokes flow field are solved for  $V_f$  ranging from 0.3 to 0.75. The velocity distribution of a typical case of in-plane permeation is shown in Figure 5.3. As can be seen, the flow occurs mainly along the fiber axes aligned in x-direction, along which the pressure drop is specified. The corresponding pressure contour is plotted in Figure 5.4. Finally, the contour of the velocity at inlet and outlet surfaces are shown in Figure 5.5. The periodic boundary condition is observed.

The in-plane permeability of asymmetric pitch arrays,  $K_x$  and  $K_y$  are shown in Figure 5.6, along with the in-plane permeability of the symmetric pitch,  $K_p$ . Figure 5.6 shows significant difference between the in-plane permeability of symmetric and asymmetric pitch cases. At 0.70  $V_f$ ,  $K_x$  is 70% higher than  $K_p$  and  $K_y$  is 14% less than  $K_p$ . The difference is even bigger at lower fiber volume fraction. For 0.50 fiber volume fraction,  $K_x$  is three times as large as  $K_p$  and  $K_y$  is 30% less than  $K_p$ .

The numerical results of the in-plane and the transverse permeability for symmetric pitch arrays are shown together in Figure 5.7. The two curves intersect at 0.60 fiber volume fraction. The transverse permeability is higher than the in-plane permeability at fiber volume fractions less than 0.60. The ratio  $K_z/K_p$  is of order one. For fiber volume fraction higher than 0.60, the in-plane permeability is much larger than the transverse permeability. The anisotropy ( $K_z/K_p$ ) is much stronger. For asymmetric pitch, the in-plane permeability  $K_x$  and  $K_y$  are compared with the transverse permeability,  $K_z$ , in Figure 5.8 and Figure 5.9, respectively. Figure 5.8 shows that  $K_x$  is always higher than  $K_z$  for fiber

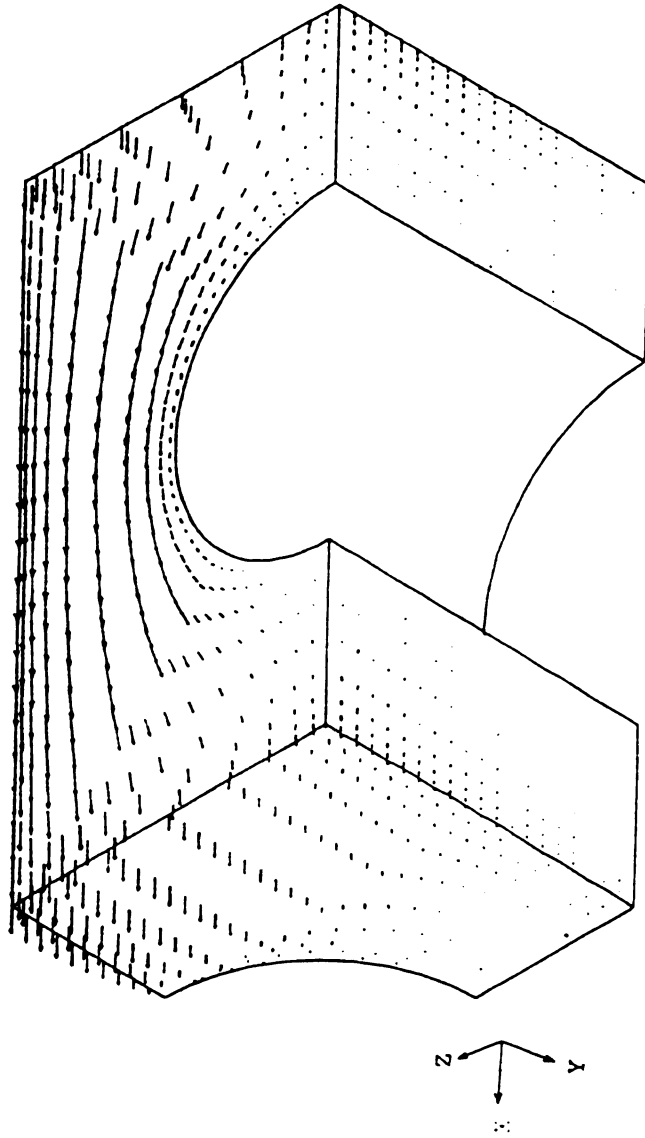
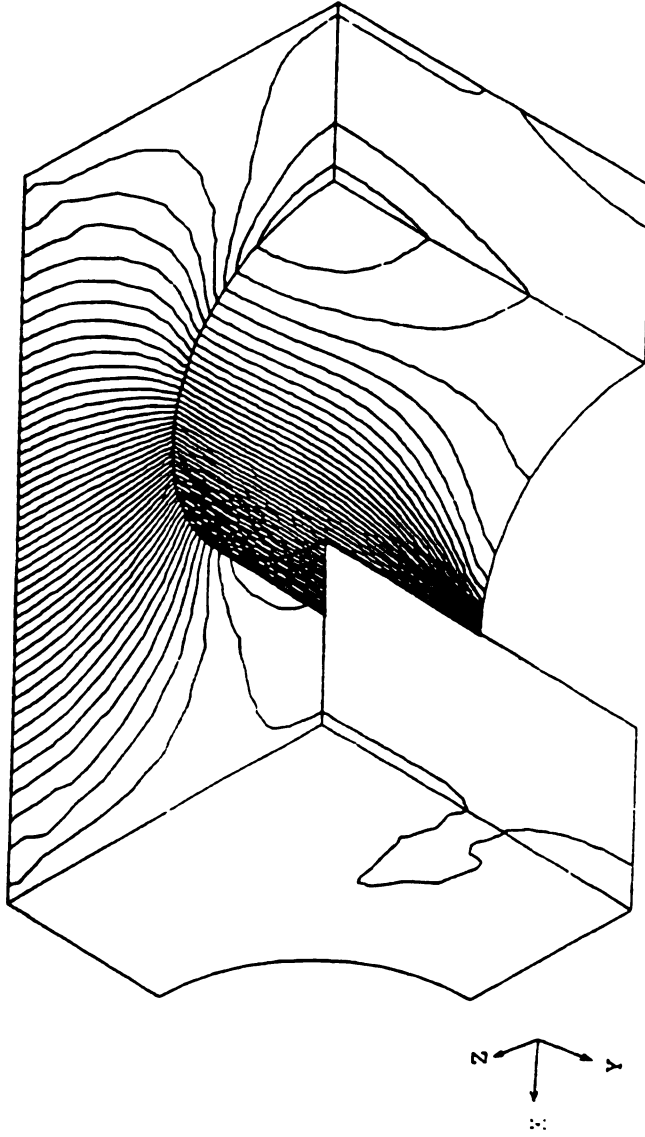


Figure 5.3: 3-D velocity field for in-plane permeation



**Figure 5.4: Pressure distribution for in-plane permeation**

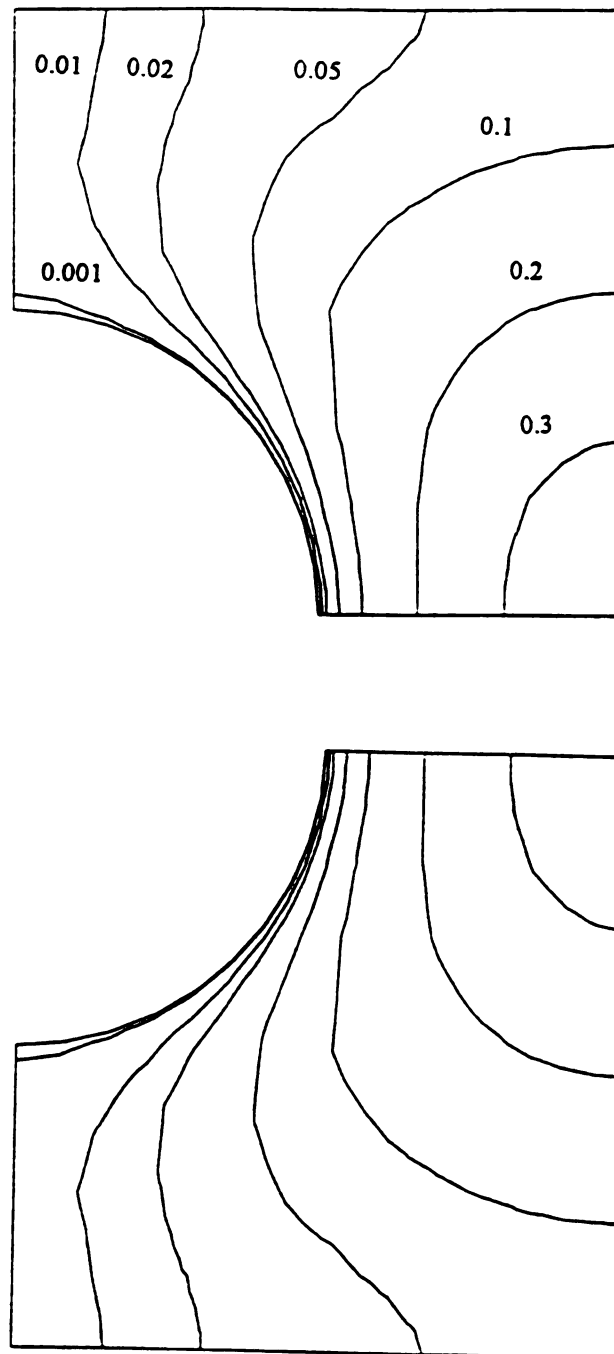


Figure 5.5: Contour of the periodic velocity boundary condition

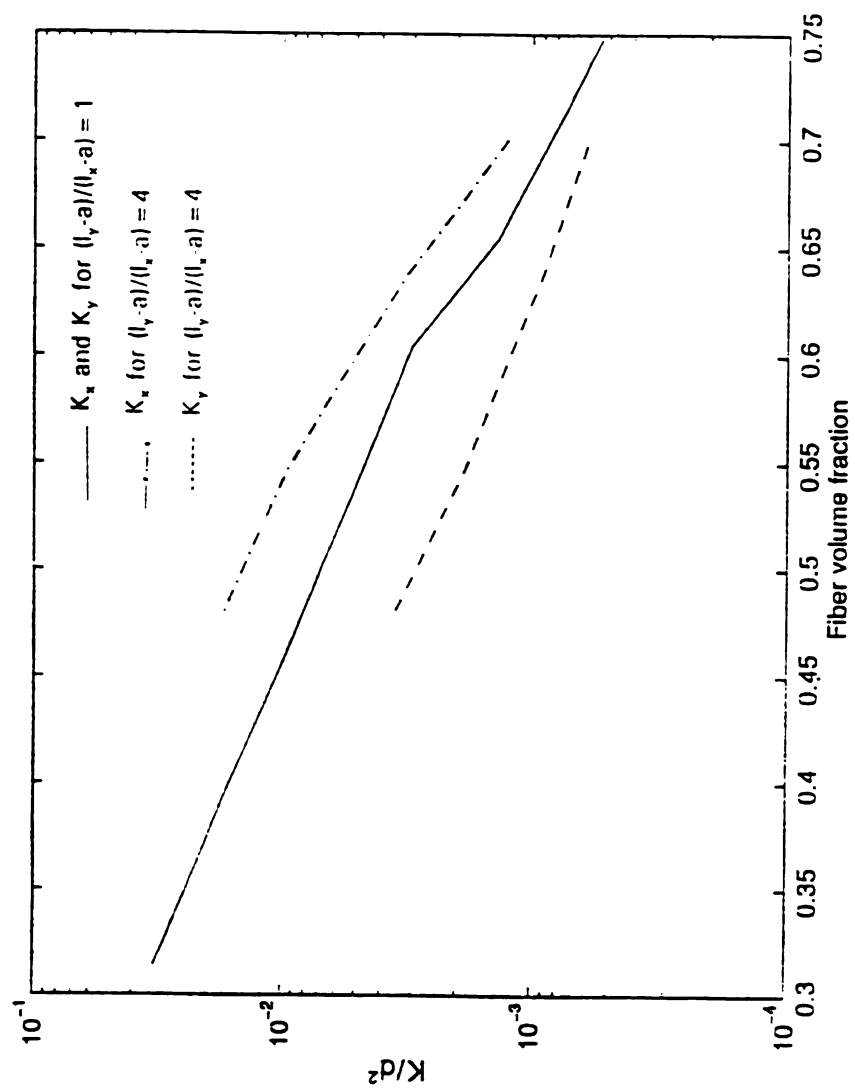


Figure 5.6: Numerical results of in-plane permeability



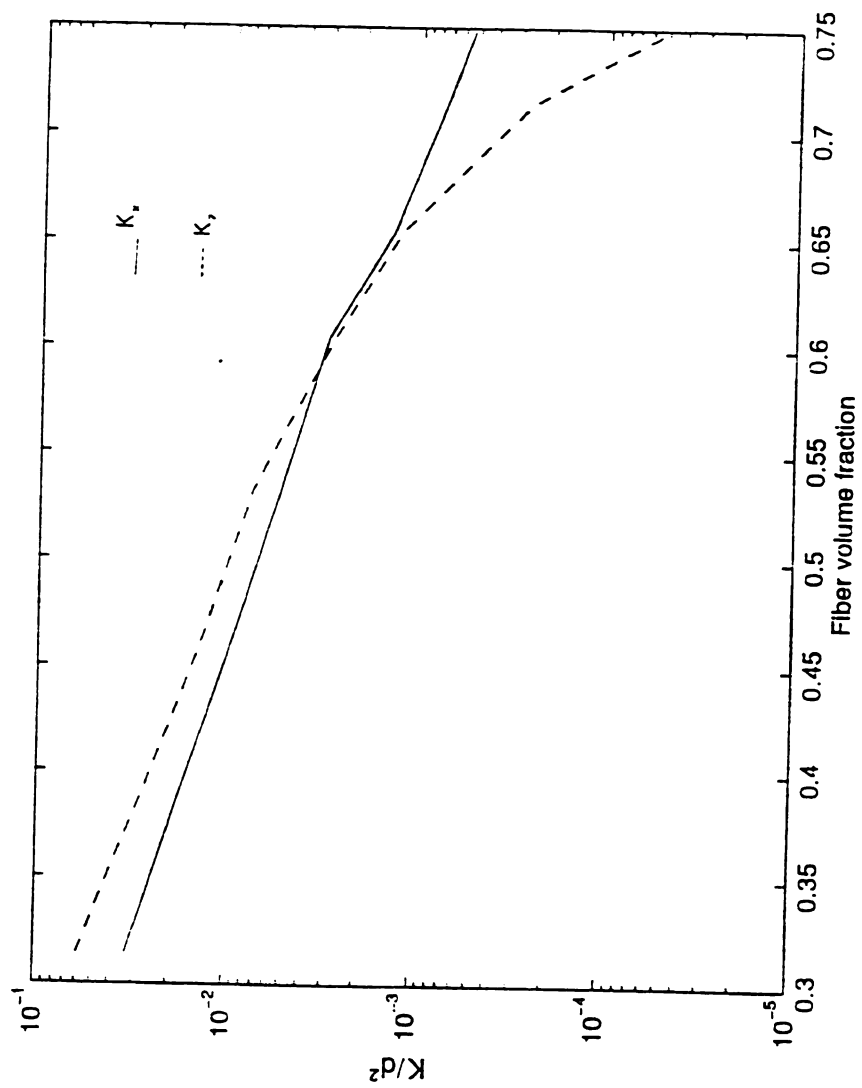


Figure 5.7: The anisotropy of symmetric pitch case

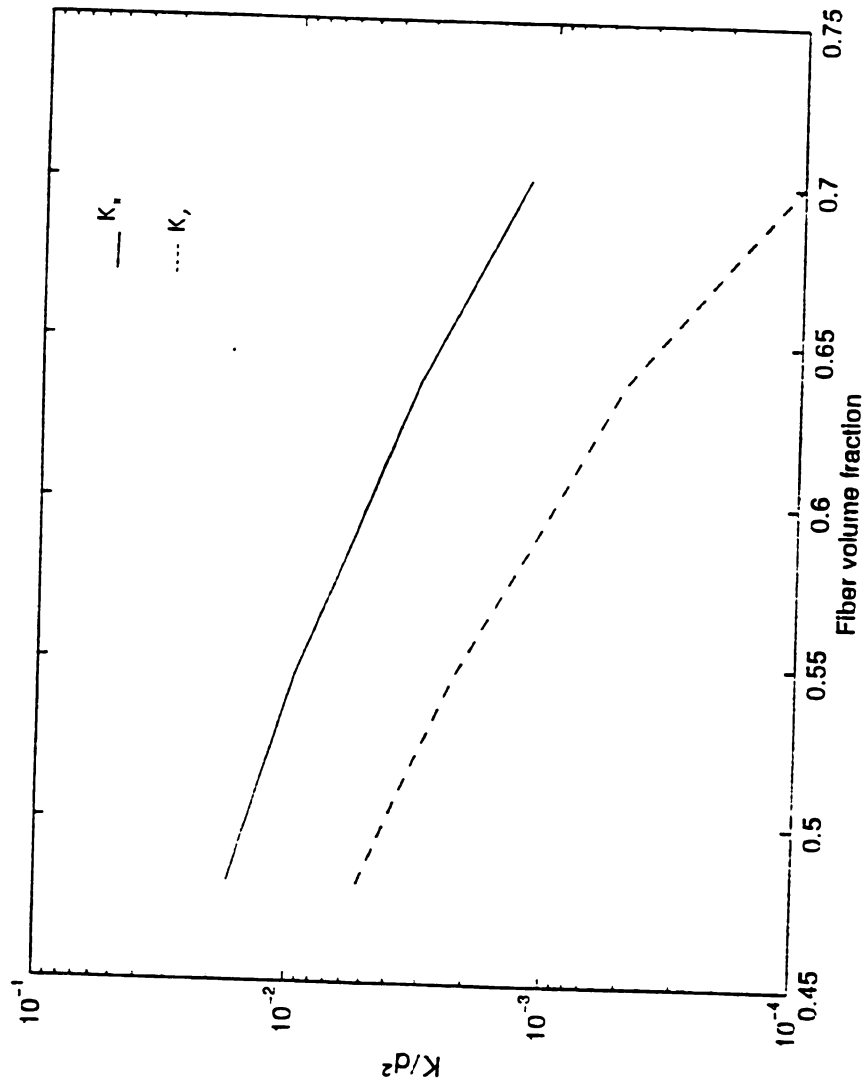


Figure 5.8: The anisotropy of an asymmetric pitch case

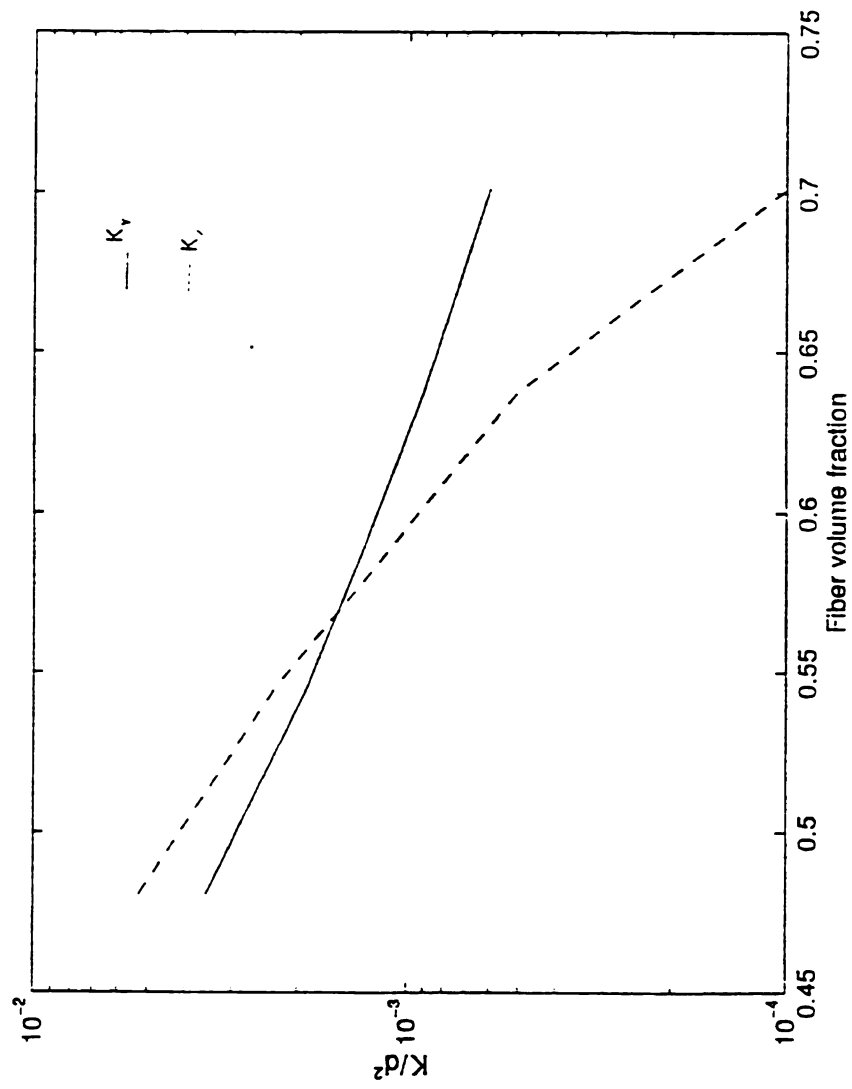


Figure 5.9: The anisotropy of an asymmetric pitch case

volume fractions ranging from 0.50 to 0.70. However,  $K_z$  is higher than  $K_y$  for  $V_f$  lower than 0.57. The variation of the anisotropy ( $K_z/K_{p,\min}$ , where  $K_{p,\min}=K_y$ ) follows the same trend as symmetric pitch cases.

### 5.3 In-plane Permeability Model

#### 5.3.1 Flow through a channel

As one can see from Figure 5.3, the flow occurs mainly along the fiber axes for in-plane permeation. Hence one can consider the flow is along a channel, the cross section of which is shown in Figure 5.10, where the cylinders aligned transverse to the flow direction are considered as a solid wall. The friction loss in this case can be expressed as

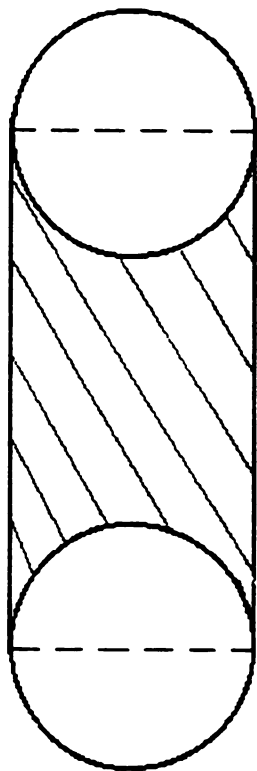
$$f = c \left( \frac{\rho U_{iz} D_h}{\mu} \right)^{-1} = \frac{-\Delta P}{L_x} \frac{2D_h}{\rho U_{iz}^2} \quad (5.5)$$

where  $D_h$  denotes the hydraulic diameter,  $f$ , the friction factor,  $c$ , the shape factor,  $L_x$ , the distance over which the pressure drop applied, and  $U_{ix}$ , average interstitial velocity component in flow direction.  $U_{ix}$  can be obtained from Eq. (5.5) as

$$U_{ix} = \frac{1}{c} \frac{-\Delta P}{L_x} \mu (2D_h^2) \quad (5.6)$$

Using Darcy's law (see Eq. (1.1) ), one can solve for the in-plane permeability

$$K_x = \frac{L_x}{-\Delta P} \mu U_x = \frac{1}{c} \frac{\beta}{1+\beta} \left( 1 - \frac{\alpha + \alpha \beta}{\beta^2 + \alpha} V_f \right) (2D_h^2) \quad (5.7)$$



$$2 l_x$$

Figure 5.10: Channel cross section shape of in-plane permeation

Note that

$$U_x = \frac{\beta}{1+\beta} \left(1 - \frac{\alpha + \alpha \beta}{\beta^2 + \alpha} V_f\right) U_{ix} \quad (5.8)$$

From the definition, the hydraulic diameter is

$$D_h = \frac{2a_x \left(1 - \frac{\alpha + \alpha \beta}{\beta^2 + \alpha} V_f\right)}{\left(0.5 + \frac{\alpha + \alpha \beta}{\beta^2 + \alpha} V_f\right)} \quad (5.9)$$

Hence the in-plane permeability can be expressed in terms of  $V_f$  as

$$\frac{K_x}{a_x^2} = \frac{8}{c(1+\beta)} \frac{\left(1 - \frac{\alpha + \alpha \beta}{\beta^2 + \alpha} V_f\right)^3}{\left(0.5 + \frac{\alpha + \alpha \beta}{\beta^2 + \alpha} V_f\right)^2} \quad (5.10)$$

Here the in-plane permeability,  $K_x$  is determined by  $a_x$ ,  $c$ ,  $l_x/l_y$ ,  $a_y/a_x$ , and  $V_f$ . If the radius of the cylinders are the same ( $a_x = a_y = a$ ,  $\beta = 1$ ),

$$\frac{K_x}{a_x^2} = \frac{4}{c} \frac{\left(1 - \frac{2\alpha}{1+\alpha} V_f\right)^3}{\left(0.5 + \frac{2\alpha}{1+\alpha} V_f\right)^2} \quad (5.11)$$

Furthermore for symmetric pitch ( $l_x = l_y = 1$ ,  $\alpha = 1$ )

$$\frac{K_x}{a^2} = \frac{K_y}{a^2} = \frac{4}{c} \frac{(1-V_f)^3}{(0.5+V_f)^2} \quad (5.12)$$

This is a type of modified Carman-Kozeny equation with  $c/16$  as the corresponding Kozeny constant.

### 5.32 Model predictions and comparisons with the FEA results

To obtain the analytical solutions for in-plane permeability, the shape factor,  $c$  needs to be determined (see Eq. (5.7)). In theory the shape factor can be calculated once the velocity field is solved. In order to provide quick estimates of the permeability,  $c$  is determined by fitting the numerical results from FIDAP for the symmetric pitch case. For  $c=20$ , the analytical solutions agree well with the numerical results for fiber volume fraction varying from 0.3 to 0.75 as shown in Figure 5.11. The same value of  $c$  is used to yield in-plane permeability prediction for an asymmetric case. Both the analytical and numerical solutions are plotted in Figure 5.12 against fiber volume fraction. As can be seen, the agreement between the two is good.

### 5.4 Experimental Validation

The analytical solutions of the in-plane permeability for bi-directional fiber mats are checked against the experimental data provided by Kalyanaraman [38]. When the radius of the filament is used in the model as for the transverse permeation case, the predicted in-plane permeability is substantially lower than the experimental measurements. This can be explained by the microstructure of the compressed fiber preforms. As shown by Scanning Electron Microscopy, there exists considerable dislocations and inhomogeneities in the filament packing for the compressed fiber preform [38]. The non-uniformities in the pore size create continuous channels of diameter larger than the average filament diameter. Hence the real pore size should be represented by a length scale larger than the single filament radius. The model predictions are plotted with the experimental data in Figures 5.13 and 5.14 with an effective fiber radius about eight times

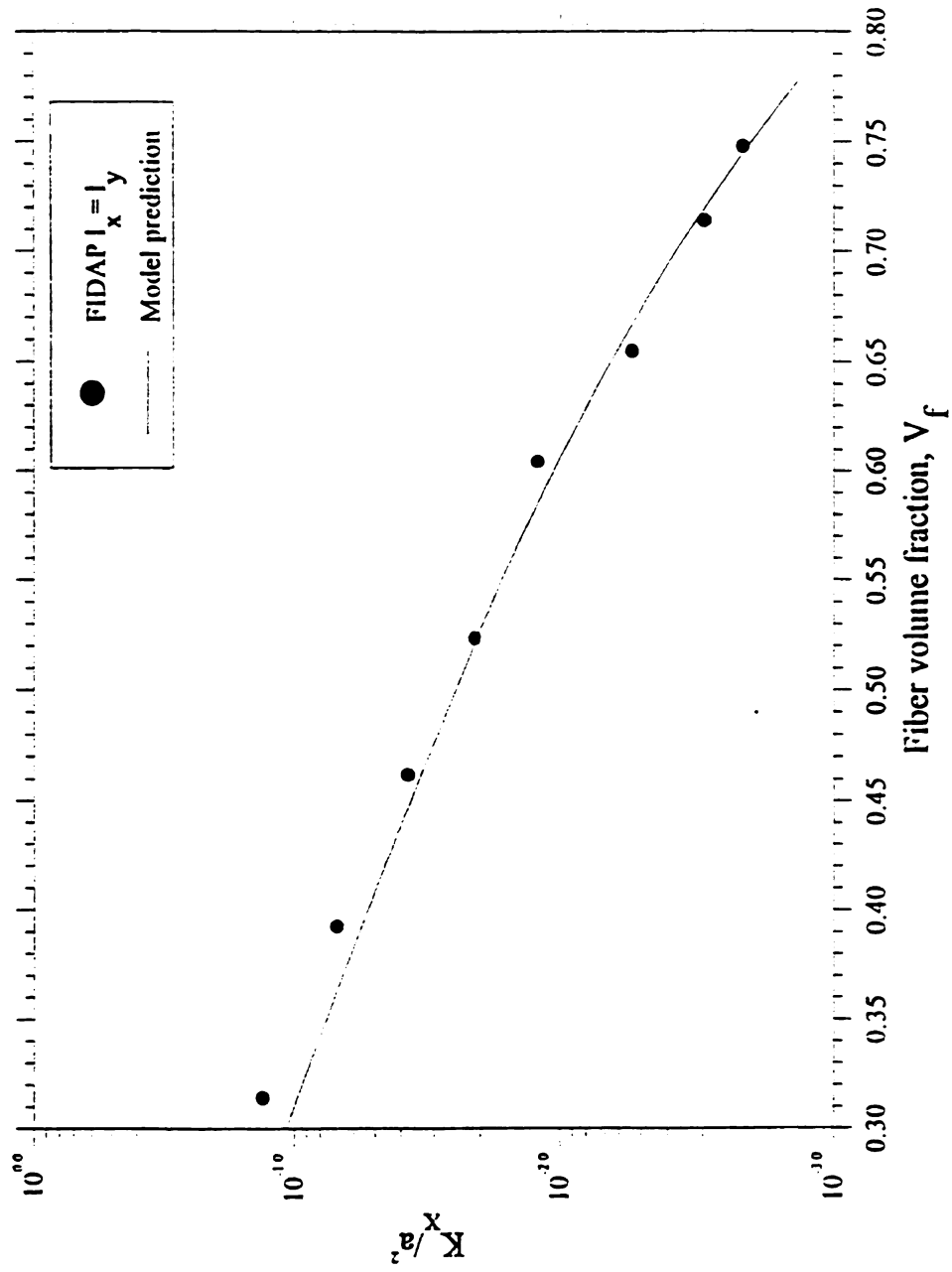


Figure 5.11: Comparison of numerical results and model prediction,  $I_x = I_y$



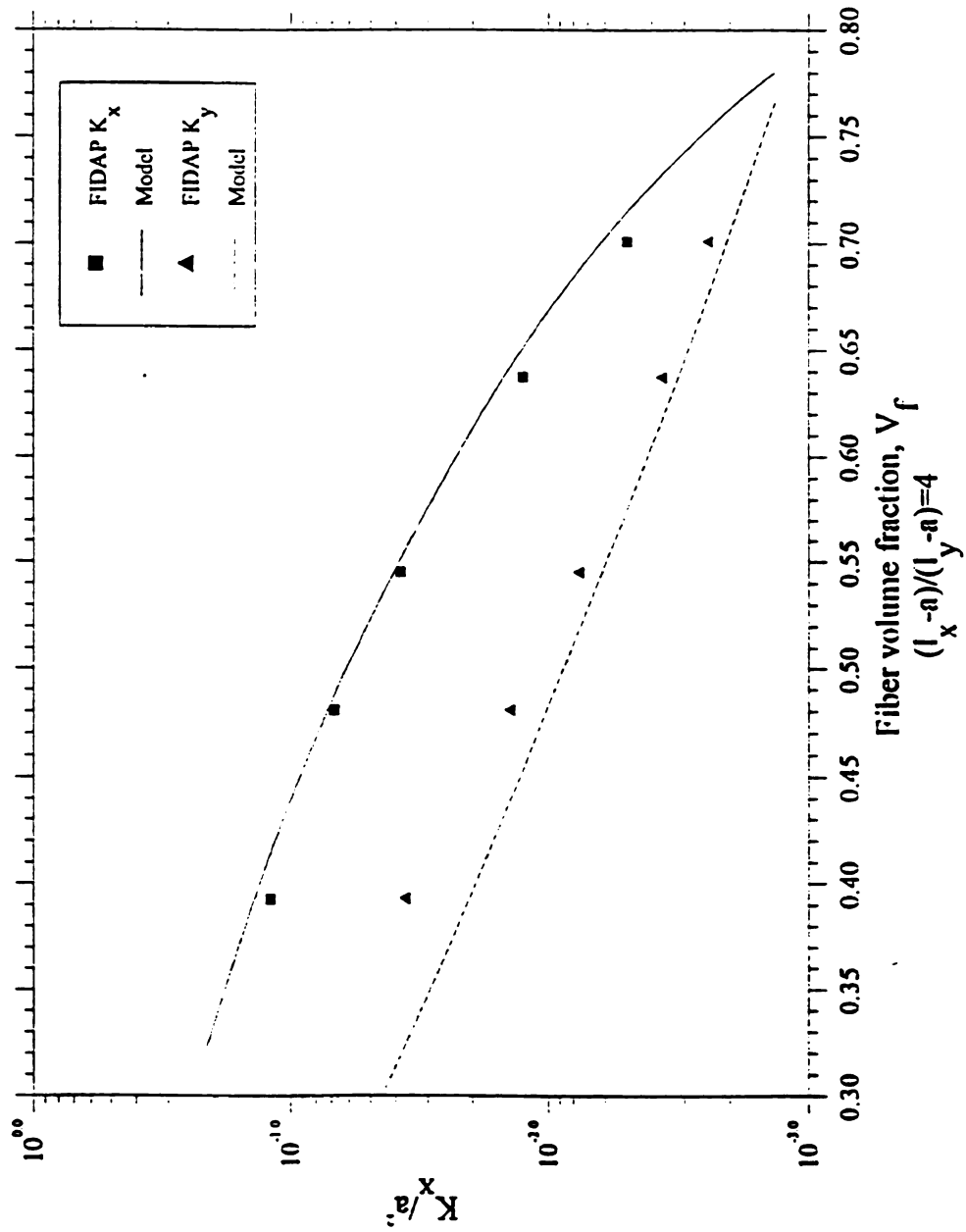


Figure 5.12: Comparison of numerical results and model prediction,  $l_x \neq l_y$

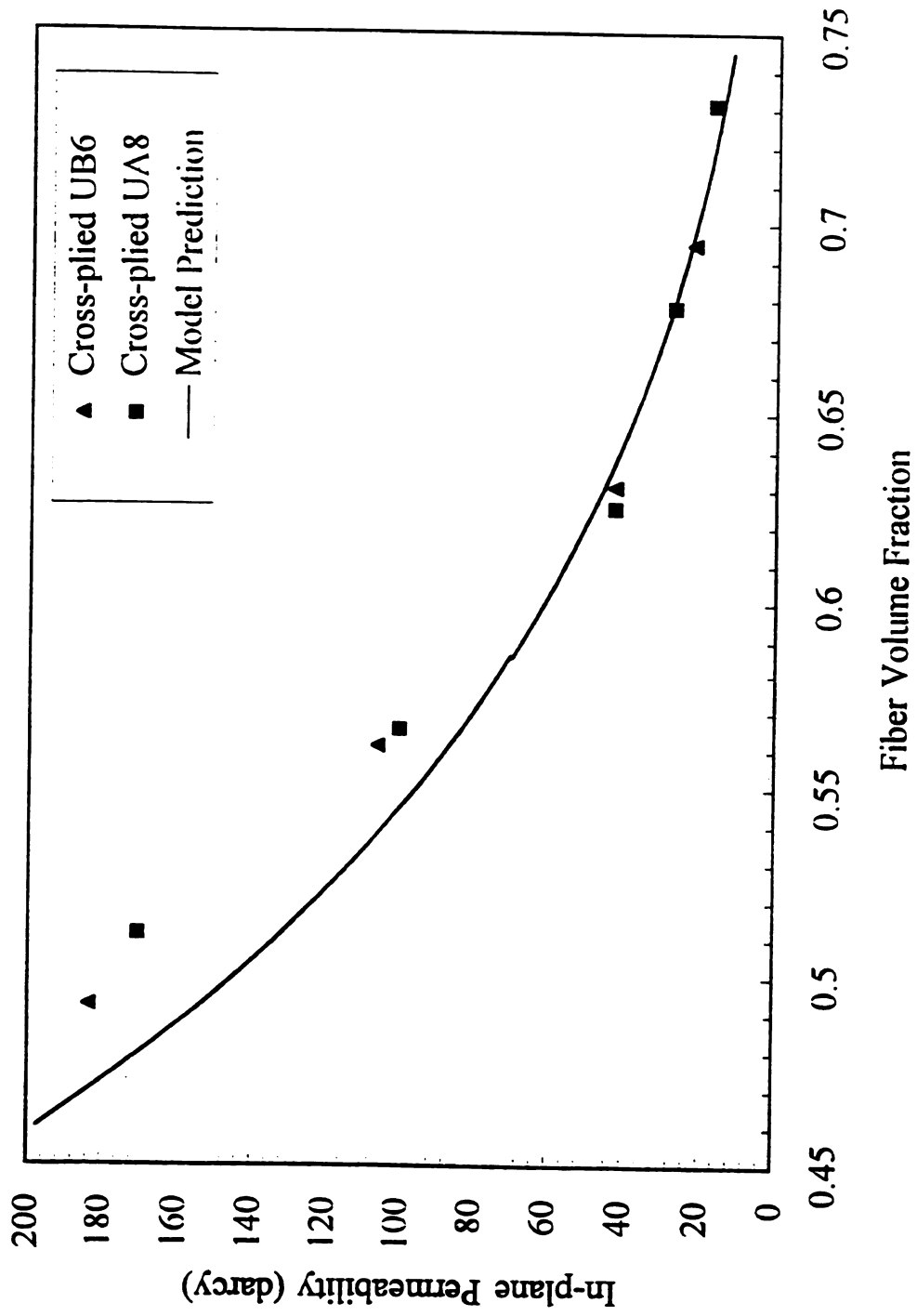


Figure 5.13: Comparison of model prediction and experimental data (cross-plyed)

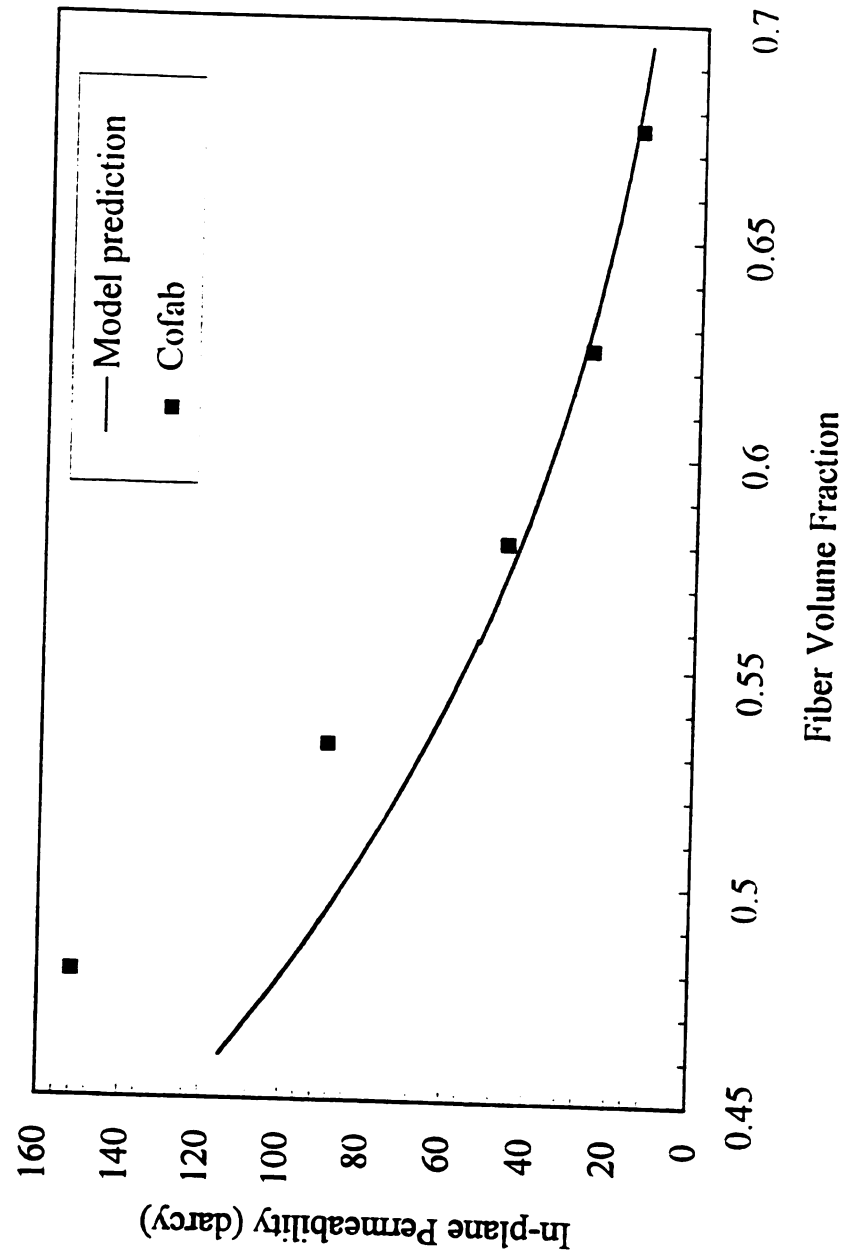


Figure 5.14: Comparison of model prediction and experimental data (Cofab)

larger than the filament radius. As can be seen, the predicted in-plane permeability values agree well with the experimental measurements when  $V_f$  is higher than 0.575. For lower  $V_f$ , the analytical solution is still lower than the experimental data.

When the classical Carman-Kozeny equation (Eq. (5.2)) is used, a better match with the experimental data can be achieved when a effective fiber radius about six times larger than the filament radius is used (see Figures 5.15 and 5.16). The shape factor in this case are calculated based on the shape of the flow channel (see Figure 5.10). This result is supported by the preform microstructure. For real fiber mats, the structure of bi-directional fiber mats is composed of layers of unidirectional mats aligned along and/or transverse to the flow direction. For  $V_f$  larger than 0.45, more than 90% of flow occurs in layers where filaments aligned along the flow direction. Hence, the relation developed for unidirectional fiber arrays is more suitable in this case. However the determination of the effective fiber radius still depends on the experimental data. Therefore more work needs to be done to link the effective fiber radius to the preform architecture.

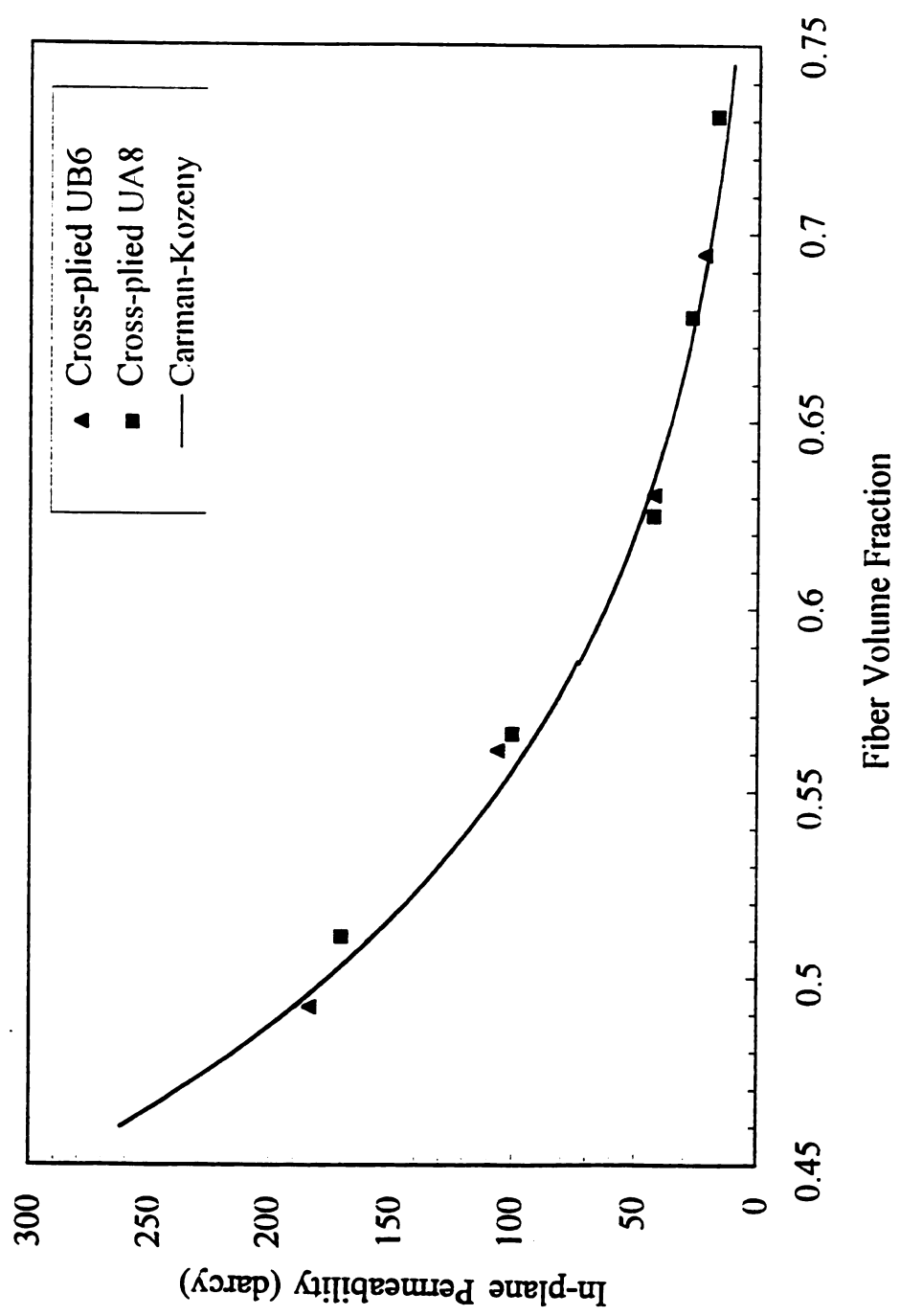


Figure 5.15: Companion of experimental data and Carman-Kozeny equation (cross-ply)

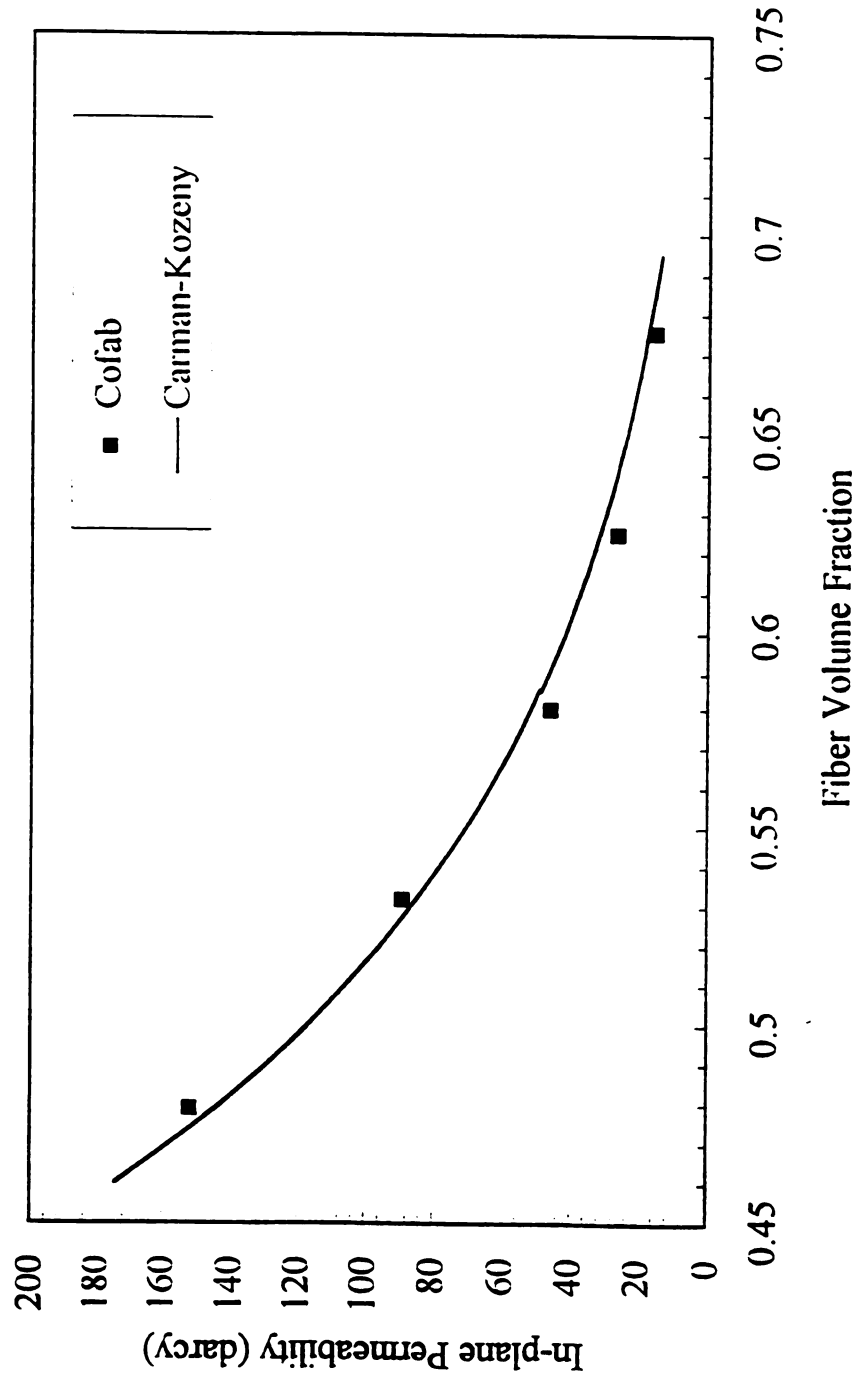


Figure 5.16: Comparison of experimental data and Carman-Kozeny equation (Cofab)

## ***Chapter 6 CONCLUSIONS AND RECOMMENDATIONS***

### **6.1 Conclusions**

The conclusions of this thesis are:

- (1) An easily solved process model has been developed for controlling the resin viscosity and mobility gradients during mold filling of the liquid molding processes (S-RIM and RTM). The model predicts resin viscosity variations due to dissolved binder content, mold heating, and chemical reaction. The model predictions on binder dissolution matches well with experimental data under several different mold wall heating conditions. This means that the model describes the interaction between non-isothermal effects and binder dissolution effects well. Finally, design limits on the ratio of filling time to a characteristic dissolution time have been developed for a case with this model.
- (2) Raising the mold wall temperature is found to be an effective control means to reduce the extent of viscosity increase along the filling direction as long as the resin is still far from its gel state. However, raising the resin inlet temperature may cause an increasing viscosity in the direction of flow when the resin inlet temperature is higher than the mold wall temperature. Simulations also show that a variable mold wall temperature profile

could be more effective in reducing the extent of resin viscosity increase than a uniform wall temperature profile when binder dissolution is coupled with the mold filling process.

(3) The effect of preform architecture on permeation through bi-directional fiber mats has been investigated with finite element analysis (FIDAP). The variation of permeability with fiber volume fraction ranging from 0.3 to 0.75 has been computed along different directions of periodic, repeat cells of bi-directional cylinder arrays. Arrangement with symmetric pitch as well as asymmetric pitch have been compared for permeability. The FEA analysis shows that the transverse permeability is lowered significantly as the pitches along the two cylinder axes are made asymmetric. This is supported by the experimental data reported by Morse et al. The anisotropy of permeability for these symmetric arrays ( $K_z/K_x$ ) is of order 1 until a fiber volume fraction of 0.65 is reached; after this, the anisotropy is strong. As the array is made asymmetric (different pitches along the two axes directions), similar trends are seen for the ratio  $K_z/K_{x,min}$ ; it is of order one until a fiber volume fraction of 0.65. It must be emphasized that the predictions are for perfectly aligned stacks. Fiber mats should be aligned exactly on top of each other in order to test these predictions.

(4) For transverse permeability prediction, an analytical model based on the lubrication approximation is developed to predict the transverse permeability of bi-directional fiber mats. The model prediction is first confirmed by the numerical results at high  $V_f$ . A simple modification of the analytical expression yields prediction that matches the numerical results over the entire range of fiber volume fraction. Furthermore the transverse permeability predictions match well with the experimental measurements on bi-directional fiber mats when the filament radius is used as the length scale. The usage of



the filament radius rather than the fiber tow radius is supported by the study of the microstructure of the compressed fiber preforms. Hence the analytical model developed for the transverse permeability is valid for the real fiber preforms.

(5) A modified Carman-Kozeny type of equation is also derived for the prediction of in-plane permeability of the bi-directional arrays. It has been found that a constant shape factor can be used to fit the numerical results obtained from FEA analysis for symmetric pitch case over the entire range of fiber volume fraction. Using the same constant, the model prediction for a asymmetric pitch case also agrees well with the numerical results. However, the analytical solutions only agree well with the experimental data for  $V_f$  larger than 0.575. Furthermore the classical Carman-Kozeny equation provide better match between the analytical solutions and the experimental data due to its closer representation of the real fiber structure. For both cases an effective fiber radius corresponding to a small cluster of filaments is used. The study on the preform microstructure reveals that dislocations and non-uniformities in the filament packing create continuous channels which are wider than the average gaps between the filaments. More work needs to be done to link the effective fiber radius to the preform architecture.

## **6.2 Scope of Future Work**

- (1) To develop models for the prediction of permeability at low fiber volume fraction ( $<0.45$ ).
- (2) To study the effects of fabric stretching during the preforming process.
- (3) To develop models for the permeability of woven fabrics.
- (4) To perform mold filling analysis using the information gained from the permeability

study as well as the resin viscosity behavior and its reaction kinetics.

(5) To conduct molding runs to confirm the results from the numerical simulations and to develop guidelines on proper locations of gate(s) and vent(s), and appropriate resin injection rates.

## ***BIBLIOGRAPHY***

## BIBLIOGRAPHY

1. Engelman, M. S., *FIDAP Theoretical Manual*, Fluid Dynamics International, Evanston, IL, (1993).
2. Owen, M.J., Middleton, V., C.D. Rudd, and I.D. Revill, "Fiber Wet-out in High Speed Resin Transfer Moulding", *Interfacial Phenomena in Composite Materials, Conference 1989*, pp 208-19, University of Sheffield, Sept. 5-7, 1989.
3. Hsu, C.P., Kinkelaar, M., Hu, P. and Lee, L. J., "Effects of Thermoplastic Additives on the Cure of Unsaturated Polyester Resins", *Polymer Engineering and Science*, 31, 1450 (1991).
4. Backes, D., "Effects of Resin Soluble Binder on Mold Filling with Non-Woven Preforms", M.S. thesis, Dept. Chemical Engineering, Michigan State University, East Lansing, (1993).
5. Han, K., Trevino, L., Lee, L.J., and Liou, M., "Fiber Mat Deformation in Liquid Composite Molding. I: Experimental Analysis", *Polymer Composites*, 14, 144 (1993).
6. Mishra, S., and Jayaraman, K., "Transverse Permeation through Compressible Stacked Glass Fiber Mats over a Range of Fiber Volume Fractions", *SAE Transactions*, 102 (5), No. 930174, Detroit (1993).
7. Coulter, J.P., and Guceri, S.I., "Resin Transfer Molding: Process Review, Modeling and Research Opportunities", *Proc. Manufacturing International '88*, ed. T.G. Gutowski, ASME, NY, p. 79, (1988).
8. Bruschke, M.V., and Advani, S.G., "A Finite Element/Control Volume Approach to Mold Filling in Anisotropic Porous Media", *Polymer Composites*, 11 (6), 398, (1990).
9. Bruno, A., Molina, G. Betracchi, G., and Moroni, A., "Flow Behavior in RTM: Numerical Simulation", *Proceedings of 7th ACM/ESD Conference*, Detroit, p.149, (1991).
10. Wang, H.P., Liang, E.W., and Perry, E.M., "FEMAP-RTM: A Resin Transfer Molding Process Simulator", *Proceedings of 7th ACM/ESD Conference*, Detroit, p. 217, (1991).

11. Lin, R.J., Lee, J., and Liou, M. J., "Mold Filling and Curing Analysis in Liquid Composite Molding", *Polymer Composites*, 14 (4), 71, (1993).
12. Loos, A. G., and Weideman, "RTM Process Modeling for advanced Fiber Architectures", *Proceedings of 7th ACM/ESD Conference*, Detroit, p. 209, (1991).
13. Owen, M. J., Rudd, C.D., and Kendall, K.N., "Modeling the RTM Process", *Proceedings of ACM/ESD Conference*, Detroit, p. 187, (1991).
14. Smith, J.M., *Chemical Engineering Kinetics*, McGraw-Hill, (1981).
15. Bird, R. B. et al , *Transport Phenomena*, John Wiley & Sons, (1960).
16. Bejan, A.B., *Convection Heat Transfer*, McGraw-Hill, (1984).
17. Acrivos, A., "Method of Characteristics Technique", I.E.C. *Process Design and Development*, p. 703, (1956).
18. Larson, B., and Drzal, L. T., "Resin Spreading & Fiber Wetting in a Liquid Composite Molding Environment", submitted for publication (1993).
19. Sangani, A. S., and Acrivos, A., "Slow Flow past Periodic Arrays of Cylinders with Application to Heat Transfer", *International Journal of Multiphase Flow*, 8, 193 (1982).
20. Sangani, A. S., and Yao, C., "Transport Processes in Random Arrays of Cylinders. II Viscous Flow", *Physics Fluids*, 31, 2435 (1988).
21. Berdichevsky, A. L., and Cai, Z., "Preform Permeability Predictions by Self-Consistent Method and Finite Element Simulation", *Polymer Composites*, 14, 132 (1993).
22. Cai, Z., and Berdichevsky, A. L., "An Improved Self-Consistent Method for Estimating the Permeability of a Fiber Assembly", *Polymer Composites*, 14, 314 (1993).
23. Cai, Z., and Berdichevsky, A. L., "Numerical Simulation on the Permeability Variations of a Fiber Assembly", *Polymer Composites*, 14, 529 (1993).
24. Phelan, F. R., Jr., "Modeling of Microscale Flow in Fibrous Porous Media", *Proceedings of 7th ACCE Conference*, Detroit, Michigan, 175 (1991).
25. Ranganathan, S., Phelan, F. R., Jr., and Advani, S. G., "A Generalized Model for the Transverse Permeability of Unidirectional Fibrous Media", Submitted to *Polymer Composites*, (1994).
26. Keller, J. B., "Viscous Flow through a Grating or Lattice of Cylinders", *Journal of Fluid Mechanics*, 18, 94 (1964).

27. Skartsis, L., Khomami, B., and Kardos, J. L., "Resin Flow through Fiber Beds during Composite Manufacturing Processes. Part I: Review of Newtonian Flow through Fiber Beds", *Polymer Engineering and Science*, 32, 231 (1992).
28. Bruschke, M. V., and Advani, S. G., "Flow of Generalized Newtonian Fluids Across a Periodic Array of Cylinders", *Journal of Rheology*, 37, 479 (1993).
29. Chmielewski, C., Petty, C. A., and Jayaraman, K., "Crossflow of Elastic Liquids Through Arrays of Cylinders", *Journal of Non-Newtonian Fluid Mechanics*, 35, 309 (1990).
30. Skartsis, L., Khomami, B., and Kardos, J. L., "Resin Flow Through Fiber Beds During Composite Manufacturing Processes. Part II: Numerical and Experimental Studies of Newtonian Flow Through Ideal and actual Fiber Beds", *Polymer Engineering and Science*, 32, 231 (1992).
31. Gebart, B. R., "Permeability of Unidirectional Reinforcements for RTM", *Journal of Composite Materials*, 26, 1100 (1992).
32. Happel, J., "Viscous Flow Relative to Arrays of Cylinders", *AIChE Journal*, 5, (1959).
33. Trevino, L., Rupel, K., Young, W. B., Liou, M. J., and Lee, L. J., "Analysis of Resin Injection Molding in Molds With Preplaced Fiber Mats. I: Permeability and Compressibility Measurements", *Polymer Composites*, 12, 20 (1991).
34. Young W. B., Rupel, K., Han, K., Lee, L. J., and Liou, M. J., "Simulation and experimental Verification of Mold Filling in Resin Transfer Molding and Structural RIM", *Proc 45th ann conf, Composite Institute*, session 9-D, 1, (1991).
35. Wu, C. H., Wang, T. J., and Lee, L. J., "Trans-plane Permeability Measurement and its Application in Liquid Composite Molding", *Polymer Composite*, 15 (4), 288, (1994).
36. Morse, C. T., Ochoa, O. O., Barron, J. H., and Barron, D. L., "Optimization of SRIM Automotive Bumper Beams Through Permeability and Wet-out Characterization", *Proceedings of 8th ACCE Conference*, Chicago, Illinois, 1 (1992).
37. Kim , Y. R., and McCarthy, S. P., "Compressibility and Relaxation of Fiber Reinforcements during Composite Processing", *Polymer Composite*, 12 (1), 13, (1991).
38. Kalyanaraman, P., "Permeability Characterization of Stitched Bi-directional Fiber Preforms", M.S. thesis, Dept. Chemical Engineering, Michigan State University, East Lansing, (1995).
39. Drummond, J. E., and Tahir, M. I., "Laminar Viscous Flow through Regular Arrays

of Parallel Solid Cylinders", *International Journal of Multiphase Flow*, 10, 515 (1984).

40. Wang, T. J., Wu, C. H., and Lee, L. J., "In-plane Permeability Measurement and Analysis in Liquid Composite Molding", *Polymer Composite*, 15 (4), 278, (1994).

MICHIGAN STATE UNIV. LIBRARIES



31293014057479